LOW TEMPERATURE MAGNETISATION PROPERTIES OF THE SPIN ICE MATERIAL $DY_2TI_2O_7$

Demian G. Slobinsky

A Thesis Submitted for the Degree of PhD
at the
University of St Andrews

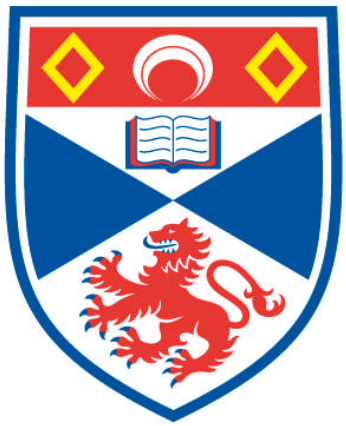

2012

Low temperature magnetisation properties of the spin ice material $Dy_2Ti_2O_7$

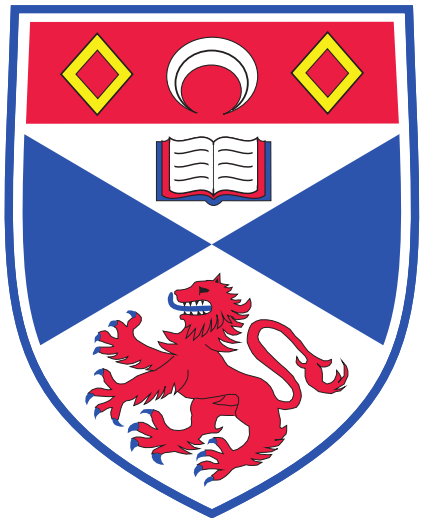

A thesis presented by

Demian G. Slobinsky

to the
University of St Andrews
in application for the degree of
Doctor of Philosophy

March 2012

Declarations

I, Demian G. Slobinsky, hereby certify that this thesis, which is approximately 41,000 words in length, has been written by me, that it is the record of work carried out by me, and that it has not been submitted in any previous application for a higher degree.

date _____ *signature of candidate* _____

I was admitted as a research student in October 2007 and as a candidate for the degree of Doctor of Philosophy in October 2007; the higher study for which this is a record was carried out in the University of St Andrews between October 2007 and April 2011.

date _____ *signature of candidate* _____

I hereby certify that the candidate has fulfilled the conditions of the Resolution and Regulations appropriate for the degree of Doctor of Philosophy in the University of St Andrews and that the candidate is qualified to submit this thesis in application for that degree.

date _____ *signature of supervisor* _____

In submitting this thesis to the University of St Andrews we understand that we are giving permission for it to be made available for use in accordance with the regulations of the University Library for the time being in force, subject to any copyright vested in the work not being affected thereby. We also understand that the title and abstract will be published, and that a copy of the work may be made and supplied to any bona fide library or research worker, that my thesis will be electronically accessible for personal or research use, and that the library has the right to migrate my thesis into new electronic forms as required to insure continued access to the thesis. We have obtained any third-party copyright permissions that may be required in order to allow such access and migration.

The following is an agreed request by candidate and supervisor regarding the electronic publication of this thesis: Embargo on both printed copy and electronic copy for the same fixed period of 1 year on the following ground: publication would preclude future publication.

date _____ *signature of candidate* _____

date _____ *signature of supervisor* _____

Abstract

A way to obtain materials that show novel phenomena is to explore the interplay between geometry and interactions. When it is not geometrically possible to satisfy all the interactions by a given configuration, then to find the ground state becomes very complicated. This interplay between geometry and interactions defines geometrical frustration.

One of the most popular examples of geometrical frustration in magnetism is spin ice. In this system, nearest neighbour ferromagnetic interactions between Ising spins in a pyrochlore structure emulate water ice by showing the same degree of frustration. This is manifested by the same ground state residual entropy. Although the clearest example of spin ice among magnets is shown by $Dy_2Ti_2O_7$, the behaviour of this material is richer than that of pure spin ice. The large magnetic moments of the rare earth Dy form a spin ice that also interacts via dipolar interactions. These long range interactions give rise to monopolar excitations which dramatically affect the dynamics of the system with respect to the pure spin ice case.

In this thesis magnetisation experiments and numerical methods are used to explore the properties of the magnetic insulator $Dy_2Ti_2O_7$. We study its excitations at low temperature and describe the out-of-equilibrium characteristics of the magnetisation processes, below a temperature where the system freezes out. For temperatures above the freezing temperature, we describe and measure a 3D Kasteleyn transition and the concomitant Dirac strings associated to it, for the field in the [100] crystallographic direction. For temperatures below the freezing temperature, we find new out-of-equilibrium phenomena. Magnetic jumps are measured and their sweep rate dependence analysed. A deflagration theory is proposed and supported by simultaneous magnetisation and sample temperature measurements obtained by a new design of a Faraday magnetometer.

Acknowledgments

I would like to acknowledge those who made my time in St Andrews a great time, and that taught the most important lessons I have learnt during this period, which I will keep with me forever. Also, I would like to thanks all those in other places, that helped and supported me during these years.

Thanks to my co-directors Andy Mackenzie and Santiago Grigera, for having given me the chance to be part of the oxide group, and for have transferred me their vast knowledge of science and of the scientific system. In the same paragraph, I would like to thank my third un-official co-director Rodolfo Borzi (Chufo) whith whom I have learnt, disagreed, discussed and then agreed on most of the topics exposed in this dissertation.

I would like to acknowledge all members of the oxide group and those from other groups for invaluable hours of discussions and fun. Thanks to Emil and Jan, thanks to Andreas, Marcel, Ed, J.F., Karl, Rob, Alex G., Vikash, Chris H., Andrew B., Andrew G, Cliff, Lara, John A., Felix, Anna, Phil, Non, Ronan and the rest.

A very special acknowledgement to my family: My dad, and my sisters. And the most special of all, along to the dedication of the thesis, to Lorena, that changed my life and made me a better person.

"Tengo Hambre...
Comí un montón, me duele la panza."
A.L.P.

Contents

Chapter 1

Introduction

The study of magnetic materials has proven to be fundamental for the advancement of material science and the development of engineering. Since the appearance of electromagnets we have been increasingly able to master the generation of magnetic fields. Nowadays we can generate a wide range of fields from very small and controlled for industrial applications, to extremely homogeneous and high magnetic fields and gradients for laboratory use. This gives a very fine degree of control over magnets, thus generating a tremendous technological impact on our world.

Among magnets, magnetic insulators were classified into ferromagnets and antiferromagnets by the way their magnetic moments interact. For temperatures above a critical temperature set by the energy scale of the interaction both of these families behave like paramagnets. When the temperature is lowered below this scale, ferromagnetic or antiferromagnetic correlations dominate the behaviour. There are, however, systems that although having a ferromagnetic or antiferromagnetic interaction, collectively behave like paramagnets even well below their characteristic energy scale. This behaviour is achieved by making the interaction between the magnetic moments of the system incompatible with the lattice symmetry, which leads to what is generally known in physics as *frustration*. This remarkably simple prescription generates systems with complex collective behaviour and provides a recipe for the discovery of novel phenomena.

There are at least two different ways to obtain frustration. The first comes from changes in the signs of the interactions between different particles. This is the typical frustration observed in spin glasses obtained by diluting a magnetic ion into a host crystal. This case is illustrated in the left drawing of figure 1.1, in which a host square lattice of spins with only antiferromagnetic bonds becomes frustrated from the symmetric and competing interactions obtained by the introduction of randomly spaced ferromagnetic

bonds. The second way to obtain frustration is accomplished by geometrical frustration, which arises from the impossibility of a system to maximally fulfil all local constraints (*i.e.*, minimise the local energy). A typical example of geometrical frustration is that of a triangle with collinear Ising spins on its vertices interacting via an antiferromagnetic interaction. It is easy to see that after the first two spins choose to be anti-parallel (in any two vertices of the triangle), the third spin can choose to be either anti-parallel with the first or with the second but not with both at the same time (right drawing in figure 1.1). In this case, geometrical frustration generates three degenerate energy states for the lowest energy with no symmetry other than that of the interaction associated to this degeneration. This trivial case can be made extensive by joining triangles to form a lattice over which the same prescription is applied. In doing so, the degeneracy can become exponentially big to the point of reaching a macroscopic entropy. In this way, a very complex manifold of equal energy ground states can be obtained.

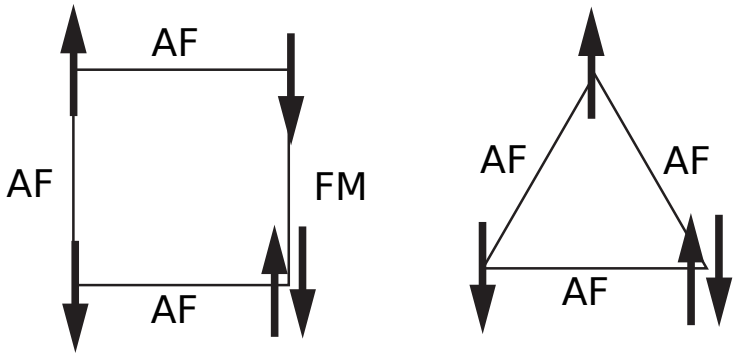

Figure 1.1: **Left**: A host square lattice with a two-dimensional grid of spins with only antiferromagnetic (AF) bonds becomes frustrated from the nearly symmetric and competing interactions obtained by the introduction of randomly spaced ferromagnetic (FM) bonds. **Right**: A triangle with collinear Ising spins on its vertices interacting via an antiferromagnetic interaction is an example of frustration. After the first two spins choose to be anti-parallel, the third spin will be parallel to only one of them.

As we mentioned, one of the hallmarks of frustrated systems is that even though they have an energy scale given, for instance, by the ferromagnetic or antiferromagnetic coupling constant, they remain paramagnetic below that energy scale. This suggests a convenient way to assign a degree of frustration, by defining the so called frustration index given by the ratio of the typical energy scale (in temperature) of the problem and the experimental measured

energy where the system deviates from the paramagnetic behaviour [1].

In geometrical frustrated magnets, the flexibility of the ground state given by the degeneracy opens a whole new world for excitations. All sorts of topological excitations, even at the classical level, drive frustrated systems through uncommon dynamics and transitions. Some of the most popular examples of frustrated magnets of the last fifteen years belong to the family called *spin ice*. The magnetic lattice of these magnets is formed by corner sharing tetrahedra with Ising spins on their vertices, pointing along the direction joining the centres of any two contiguous tetrahedra. This arrangement yields a degeneracy of six states for each tetrahedron when the spins are made to interact ferromagnetically. The first wave of interest in spin ice materials came from the experimental demonstration of residual entropy at the lowest temperatures [9], in agreement with Pauling's prediction for water ice [6]. Recently, a renewed interest appeared when certain excitations with monopolar character were identified in the dipolar ice model suitable for real materials [35]. This model adds the more realistic long range dipolar interactions between magnetic moments that are measured in experiments, to the pure spin ice model of nearest neighbour interactions.

In this thesis we explore by means of experimental and numerical methods the properties of the magnetic insulator $Dy_2Ti_2O_7$ which presents the best experimental example of spin ice known to date. We study excitations in $Dy_2Ti_2O_7$ at low temperature and explore the out-of-equilibrium characteristics of the magnetisation processes below a temperature where the system freezes out. We find new phenomena attributable to physics extrinsic to the simple spin ice model, namely the vibrational degrees of freedom of the lattice.

The thesis is divided into three parts. In the first part, we give a self-contained approach to the physics of spin ice systems and its extension to the real material $Dy_2Ti_2O_7$. Special emphasis is given to the differences between the ideal spin ice and the real material. This is done introducing the concept of dipolar ice which constitutes the model Hamiltonian to understand the experimental results obtained in the rest of the thesis.

In the second part, the experimental as well as the numerical methods used are extensively discussed. On the experimental side, the motivations for the development of a new magnetisation probe are expressed, stressing the criteria and specifications to which it was made. On the numerical side, the Monte Carlo method is explained and the standard Ewald summation technique used for the analysis is summarised.

The third part of the thesis deals with the results obtained during three and a half years of research between the years 2007 and 2011. We show

magnetisation as a function of magnetic field studies, with the field collinear to the crystallographic [100] direction, which presents features attributable to a theoretically predicted Kasteleyn transition of string excitations. Also, the concomitant string excitations predicted by this theory are shown to exist by comparison of neutron diffraction experiments with numerical simulations. The remaining results deal with different magnetisation experiments with the field along the [111] crystallographic direction for low and high field respectively. For the low field region, new out-of-equilibrium behaviour is found and extensively analysed using concepts such as monopoles, phonon bottleneck and magnetic deflagration. At high fields, the transition between an intermediate state, known as Kagome state, and saturation is revisited. Our new results are discussed and analysed using the concepts developed along the thesis.

Part I

State of the art

Chapter 2

Spin ice

2.1 Theoretical model of spin ice

As discussed in the introduction, one of the manifestations of geometrical frustration is degeneracy. The inability of the system to resolve all the constraints imposed by geometry and interactions produces an accidental degeneracy of the ground state. Mathematically, the ground state degeneracy can be seen as the space of solutions of the constraints imposed by the interactions, over the degrees of freedom of the system. This definition can be used to give a criterion of frustration that ranks more frustrated systems (entities such as Ising or Heisenberg spins, and their interactions: nearest neighbour, dipolar, etc. defined on a geometry) according to their increasing ground state degeneracy. In particular Moessner and Chalker have studied the general problem of Heisenberg spins lying on the vertices of different geometric lattices [2]. Here we will only concentrate on the geometry related to the spin ice problem.

The first step to model spin ice consists of understanding the basic geometric structures that give the right combination of constraints and degrees of freedom to make it a frustrated system. These are: *the regular tetrahedron* and *the pyrochlore lattice.*

The regular tetrahedron is the 3-dimensional generalisation of the regular (equilateral) triangle in the following sense: while the regular triangle is obtained by connecting three equidistant non-coincident points in a plane, the regular tetrahedron is the geometrical shape obtained by connecting four equidistant non-coincident points in 3-dimensional space. This shape has 4 vertices, 6 edges and 4 faces. We will see these numbers appearing continuously in the description of the different physical properties.

In the following we assume all tetrahedra to be regular. A convenient

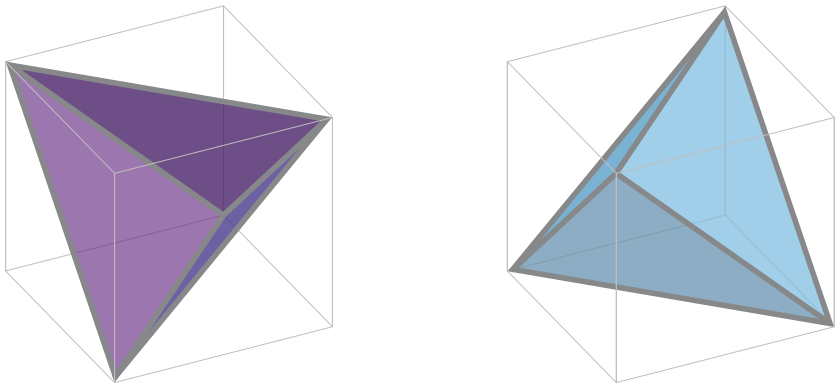

Figure 2.1: A tetrahedron can be inscribed in a cube in two different ways, connecting lines on the surfaces from bottom left to top right (purple), or from bottom right to top left (blue).

way to visualise a tetrahedron in Euclidean space is to inscribe it into a cube by making each of its four vertices coincide with four of the eight vertices of the cube as shown in figure 2.1. The coordinates of the vertices are given by a positive or a negative scale factor, depending on the chosen vertices of the cube, times the vectors (111), $(1\bar{1}\bar{1})$, $(\bar{1}1\bar{1})$ and $(\bar{1}\bar{1}1)$. In this way, the two species described in figure 2.1 can be obtained by using a positive (purple) or a negative (blue) scale factor. One species forms the tetrahedron inscribed in the cube made by connecting a line from bottom left to top right in each one of the six faces, and the other for the one connecting the lines from bottom right to top left.

The pyrochlore lattice is formed by alternating tetrahedra of the two different species joined by their vertices in such a way that the centre of two contiguous tetrahedra are joined by a straight line containing the vertex in common, as shown on the left of figure 2.2. Another important geometric structure related to the pyrochlore is its dual lattice that is formed by joining the centres of all contiguous tetrahedra. The resulting lattice is the diamond lattice depicted by black lines inside the pyrochlore on the left panel of figure 2.2.

The richness of the pyrochlore geometry stems from the fact that very complex substructures can be projected from it. For instance, the [111] projection can be seen as an alternating stack of triangular and Kagome planes and the [100] appears as a checkerboard. These are drawn on the right of figure 2.2.

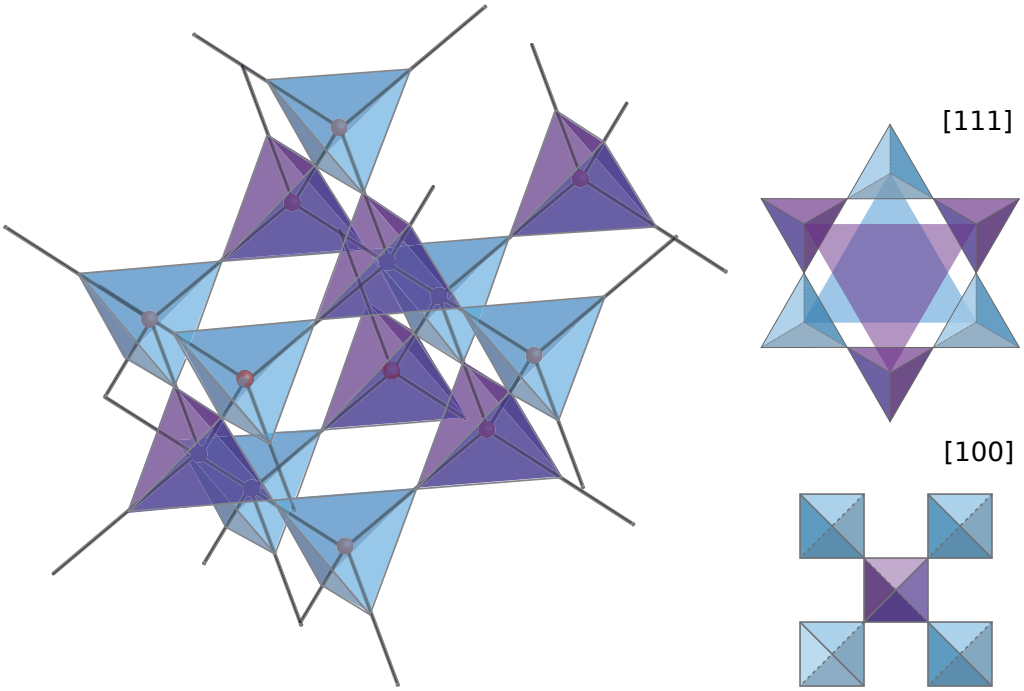

Figure 2.2: **Left**: Section of a pyrochlore lattice. The lines joining the centres of the tetrahedra form a diamond lattice which is the dual of the pyrochlore. **Right**: The [111] and [100] projections of the pyrochlore lattice.

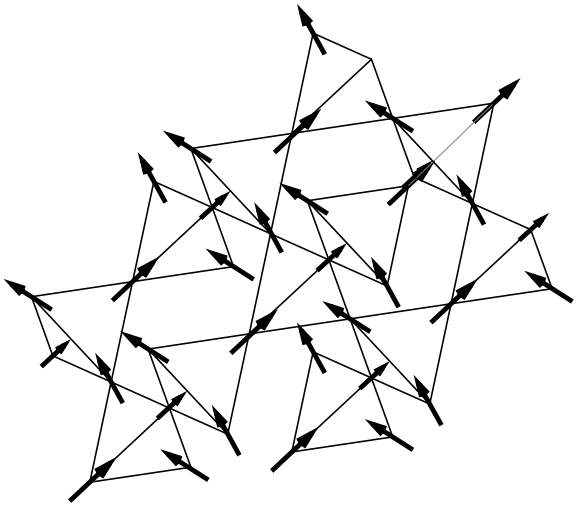

Figure 2.3: Spins in spin ice are distributed on the vertices of a pyrochlore lattice with their magnetic moment laying on the axis joining the centres of contiguous tetrahedra.

Spin ice borrows its name from water ice or simply ice. The water ice lattice is a slightly distorted version of the pyrochlore lattice. The energetics of ice are such that any given water molecule is connected to four different water molecules. Two of these connections are Hydrogen bonds and the other two are covalent bonds located around each Oxygen at fixed angles on the edges of a quasi diamond lattice (104° instead of 109°). The electrostatic interactions are frustrated in ice, and thus lead to degeneracy; there is a degeneracy for placing any bond in any edge of the diamond lattice. The freedom to place Hydrogens in the (quasi-) pyrochlore subject to the restriction of two near to and two far from the central Oxygen is the rule that generates perfect ice starting from water molecules, and is known as the *ice rule*[1] [3].

In spin ice, the spins are distributed on the vertices of a pyrochlore lattice with their magnetic moment laying on the axis joining the centres of contiguous tetrahedra as shown in figure 2.3 (these lines form the diamond lattice depicted in full black lines in figure 2.2). These spins can point towards the centre of a given tetrahedron or opposite to it. The formal analogy between spin ice and ice, from which it inherits its name, boils down to the binary property of the Ising spins that maps to the Hydrogen atoms being either *near* to a given Oxygen forming a molecule ('spin in'), or *far* from it forming an Hydrogen bond to the next water molecule ('spin out').

As was seen in the introduction, frustation generally arises with antiferromagnetic interactions. Also frustration can be obtained from ferromagnetic interactions. For instance, in spin ice the spins, $\mathbf{S}$, form an angle of $\alpha = \arccos(-1/3) = 109^\circ$ with each other. This angle changes the sign of any interaction preceding the scalar product of spins. Then, for instance, if Ising spins on the pyrochlore lattice interact through a nearest neighbour interaction of the form $J\mathbf{S}\cdot\mathbf{S}$, with $J > 0$, they can be mapped to pseudospins S with values: $+$ and $-$ keeping the same energy $-J/3SS$, but interacting through an effective interaction $K = -J/3 < 0$ that is antiferromagnetic for the pseudospins [4].

It is easy to see that a ferromagnetic nearest neighbour interaction is frustrated for the pseudospins. Indeed, the lowest energy is given by $-2J/3$ in a configuration with two pseudospins $+$ and two $-$, or in terms of spins, two *'in'* and two *'out'*. This was first realised by Anderson [5]. There are six of these configurations.

The six ice rule-preserving configurations that spins can take on a tetrahedron can be conveniently labelled through a mapping to the six faces of a cube. This convention will be extensively used throughout this thesis. In a

[1] Or ice rules, in plural, referring to the six possible configurations for each water molecule.

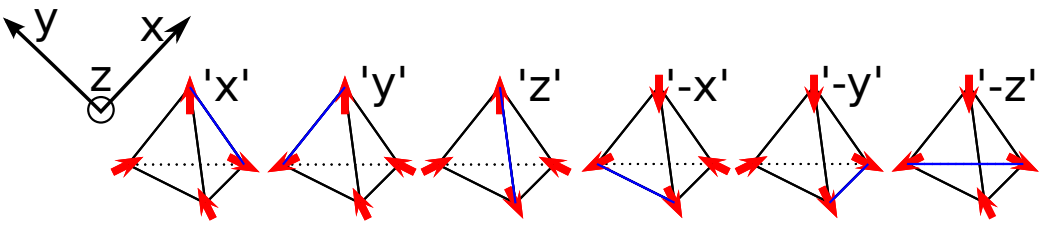

Figure 2.4: The six possible arrangements that preserve the ice rules. On blue we marked the edge that is perpendicular to the total magnetisation of the tetrahedron for each configuration.

spin ice configuration the orientation of the spins implies that the vectorial sum of them in each tetrahedron adds up to a vector perpendicular to one of the six edges of it, or which is the same, to a vector perpendicular to a face of a cube containing the tetrahedron[2]. Placing the cube on the Cartesian axes the six configurations can be labelled according to the vectorial sum of their spins: '$\pm x$', '$\pm y$' and '$\pm z$'. In figure 2.4 we show explicitly these configurations.

The total number of configurations within the ice rule manifold on the pyrochlore lattice can be estimated from the following considerations due to Pauling [6]: on one hand, for N independent spins there are $N/2$ tetrahedra, and 2^N spin configurations. On the other hand, out of 16 possible configurations for each tetrahedron only 6 reproduce the ice rule. Hence, the total number of configurations (assuming independent tetrahedra, *i.e.*, neglecting closed loop constraints[3]) is given by $2^N(6/16)^{N/2} = (3/2)^{N/2}$. This is a macroscopically big number that survives the thermodynamic limit (it logarithm scales with system size). The macroscopic number of configurations itself is associated with a configurational entropy that manifests in the measured entropy of both water ice and spin ice [8, 9].

In water ice Giauque and Ashley determined the residual entropy by integrating the specific heat as a function of temperature [8]. This classical experiment to determine the entropy of water ice was reproduced by Ramirez *et al.* to obtain the entropy of a polycrystalline sample of $Dy_2Ti_2O_7$ [9]. The result is shown in figure 2.5.

In the plot, an absolute entropy scale is introduced by the third law of thermodynamics which states, in one of its formulations, that for a *system at equilibrium the isotherm* $T = 0$ *is also isentropic.* In other words at $T = 0$

[2]This can also be resolved by adding up the vector coordinates of a spin ice configuration (for example, $(111)+(1\bar{1}\bar{1})-(\bar{1}1\bar{1})-(\bar{1}\bar{1}1) = (400)$).

[3]An exact solution for the two-dimensional case can be found in reference [7].

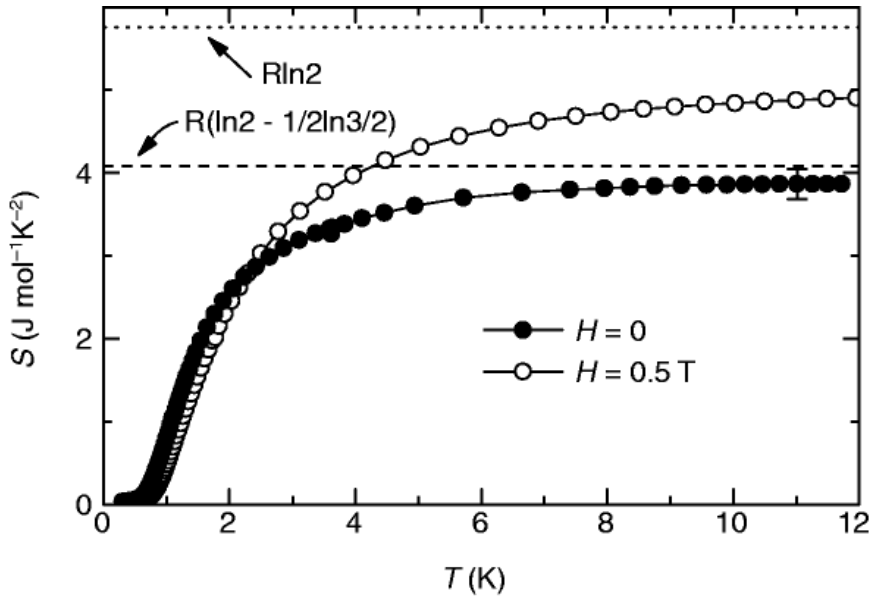

Figure 2.5: Entropy as a function of temperature calculated from the integration of the specific heat for a polycrystalline sample of $Dy_2Ti_2O_7$ in zero field (closed circles), and at $H = 0.5$T (open circles). In dotted lines, the theoretical entropy for an Ising paramagnet, $R\log 2$, and in dashed line the difference betweem this entropy and Pauling's configurational entropy $R(\log(2) - \log(3/2)/2)$. (From Ramirez *et al.* [9])

the entropy is constant, and its constant value is conventionally taken as zero. In figure 2.5 the closed circles represent the zero field entropy and the dotted lines, the high temperature theoretical entropy for an Ising paramagnet, $R\log 2$. The entropy difference between $R\log 2$ and saturation is very close to $R/2\log(3/2)$ (dashed lines) at $12K$, the equivalent value of the residual entropy of spin ice in its ground state. This means that either we have a lot of entropy to play around even at extremely low temperatures, which would be interesting in its own right for applications in magnetic cooling, or that the normalisation following the third principle of thermodynamics has to be re-examined. One should stress that the experiment was performed on a real material that is not a perfect representation of spin ice, in the sense that there are further interactions, apart from the nearest neighbour, that have to be taken into account. These interactions, mainly dipolar, can perturb the spin ice behaviour of real materials, and have to be taken into account when theories are tested. In principle, further interactions would tend to order the system at a higher temperature given by the typical energy scale

of their interaction constant. In the present case, they disfavour ergodicity and take the system out-of-equilibrium. The peculiarities of $Dy_2Ti_2O_7$ and the interaction between its magnetic moments will be described, in the next section.

In the same figure in open circles the evolution of entropy under an applied field of $H = 0.5$T is shown. As can be seen, although not all, some of the residual entropy is released by the application of a magnetic field. The fact that the magnetic field changes the amount of available micro-states illustrates the richness of spin ice, in which different configurations can be tuned with magnetic field to give different ground states and completely different behaviours as will be shown in section 2.3.

2.2 The real material: $Dy_2Ti_2O_7$

In the previous section we showed that the ideal spin system on the sites of a pyrochlore lattice can be formally mapped to water ice provided that the spins are Ising spins, and that they interacted via nearest neighbour ferromagnetic interactions.

There are a few examples of magnetic materials that present spin ice behaviour. All of them are isostructural to the cubic pyrochlore oxide of the form $R_2M_2O_7$ with R a trivalent +3 rare earth (Ho, Dy, etc.) and M a +4 transition or p-block metal ion (Ti, Sn, etc.) [10]. Among them, by far the most studied cases to date are $Ho_2Ti_2O_7$ and $Dy_2Ti_2O_7$.

In the Holmium compound, there is a strong hyperfine coupling that causes nuclear spins to undergo an ordering transition at $\sim$ 300mK. This nuclear transition makes a huge contribution to the specific heat [11] and has to be carefully subtracted, as shown in figure 2.6.

In practice this is done by substracting the contribution of Holmium in a pyrochlore structure such as Ho_2GaSbO_7 [12]. Nevertheless, the Holmium compound has an acceptable neutron cross section, and given that the nuclear spins remain confined to Bragg peaks in neutron diffraction experiments, they do not obscure the image of the electronic spins, making the material suitable for this kind of study [13]. On the other hand, the Dysprosium compound has much weaker hyperfine coupling, and hence, is a clearer example of spin ice in bulk investigations. However, $Dy_2Ti_2O_7$ has the disadvantage of having a large absortion cross section for neutron scattering. This inconvenience can be overcome by the use of very expensive isotopical samples of ^{162}Dy that present a small enough scattering cross section to make them adequate for this kind of experiments [14, 15, 16]. A further advantage of this isotope is that it has zero nuclear spin making it a pristine spin ice test material for

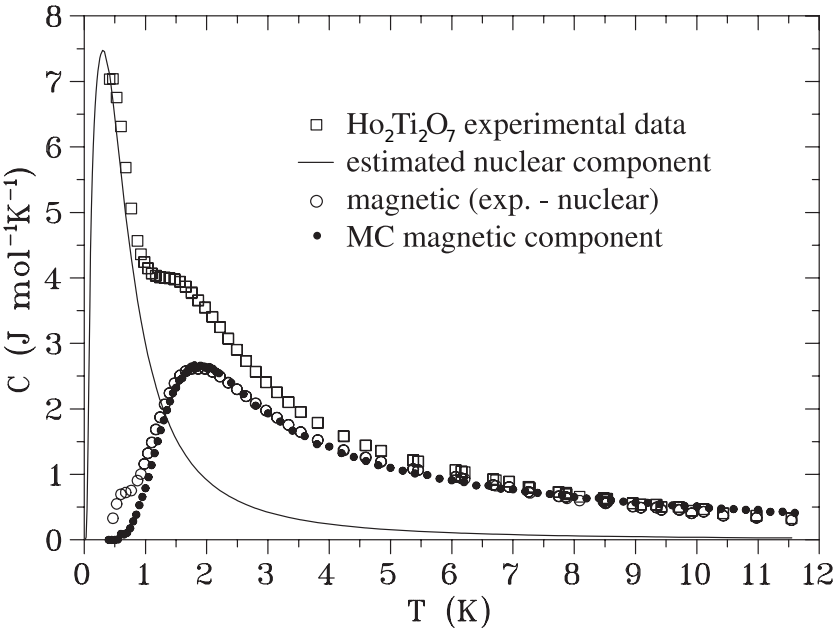

Figure 2.6: Specific heat of $Ho_2Ti_2O_7$. The open squares are the experimental data. The expected nuclear contribution is indicated by the curve, while the resulting magnetic specific heat estimation is shown by the open circles. Near 0.7 K the estimation is prone to a large error. Monte Carlo simulation results are indicated by the filled circles. (From Melko *et al.* [11])

thermal experiments, as explained by Klemke *et al.* [17].

To the naked eye $Dy_2Ti_2O_7$ has a transparent amber colour corresponding to its band insulating character. The Titanium and Oxygen atoms form a matrix that sustains the Dy^{3+} atoms whose electrons are the ones responsible for the magnetism (Ti^{4+} has a full shell). At room temperature the material is a paramagnet with a Curie-Weiss law consistent with a magnetic moment of $\mu \sim 10\mu_B$, very close to the theoretical value of $10.65\mu_B$ [18]. The ground state for the spin system is a doublet with an excitation energy to the first excited state of $\sim$ 365K. In figure 2.7, the theoretical admixture of states for the crystal electric field of $Dy_2Ti_2O_7$ is shown. This admixture is in good agreement with the one measured by ^{47}Ti-NQR (nuclear quadrupolar resonance) for different thermal populations between $70 - 300$K [19], and gives an almost pure $|\pm 15/2\rangle$ doublet leading to strong Ising anisotropy at low temperatures. Below 10K excitations above the ground state doublet are exponentially suppressed, giving place to the development of spin ice correlations. Susceptibility and heat capacity measurement confirm Curie-

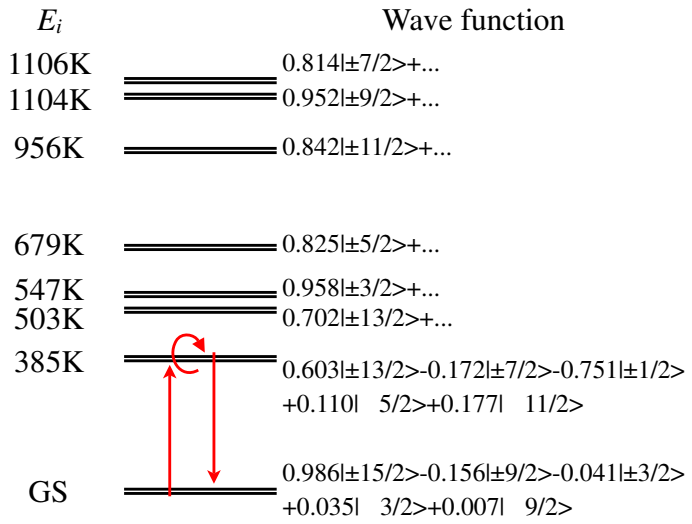

Figure 2.7: Crystal field level scheme of $Dy_2Ti_2O_7$. The arrows represent the major process for the spin-flip relaxation between the ground-state doublet. The ground-state is almost pure $|\pm 15/2\rangle$ leading to strong Ising anisotropy at low temperatures. (From Kitagawa *et al.* [19] Copyright©(2008) by the American Physical Society)

Weiss behaviour with a ferromagnetic nearest neighbour $J \sim 1.1$K [18, 9].

2.2.1 Dipolar ice

The low value of 1.11K for J together with the large value of the magnetic moments in $Dy_2Ti_2O_7$, $\mu \sim 10\mu_B$ raises the question about the role played by dipolar interactions. The mutual influence that spins feel due to the dipolar interaction can be readily estimated from the values of the magnetic moments and the distance between them. The distance between Dy atoms in $Dy_2Ti_2O_7$ is $r_{nn} \sim 3.57$Å which gives for the nearest neighbour interaction a dipolar contribution of

$$D_1 = \frac{5}{3}\left(\frac{\mu_0}{4\pi}\right)\frac{\mu^2}{r_{nn}^3} = +2.35\text{K} \tag{2.1}$$

where μ_0 is the permeability of vacuum, and 5/3 is a geometrical factor. This contribution is ferromagnetic, and implies that, in order to account for the 1.11K ferromagnetic coupling measured in susceptibility experiments, the nearest neighbour coupling coming from the exchange interaction has to be

Figure 2.8: **Left**: experimental neutron-scattering pattern of $Ho_2Ti_2O_7$ at 50mK. Dark blue shows the lowest intensity level, red-brown the highest. **Centre**: calculated neutron-scattering for the nearest-neighbour spin ice model at $T = 0.15J$. **Right**: calculated neutron-scattering for the dipolar spin ice model at $T = 0.6$K. This can be compared with the experimental scattering due to spin freezing below ~ 650mK as discussed in the text. The clear match between the left and right figures indicates the reality of the dipolar interactions. (From Bramwell *et al.* [13] Copyright©(2008) by the American Physical Society 2001)

antiferromagnetic and of the order of -1.24K[4].

It is important to note that dipolar interactions cannot be neglected in this material and that their long range character plays a substantial role in the behaviour of the system. This point is illustrated by the neutron diffraction experiment by Bramwell *et al.* [13] shown in figure 2.8. In this figure, the low temperature diffraction from a sample of $Ho_2Ti_2O_7$ (left) cooled at zero field is compared to Monte Carlo simulations of pure spin ice (centre) and of 'dipolar ice' (right), *i.e.*, a spin ice where the expansion of dipolar interaction is not truncated to the first neighbour. The left and right figures match well, and differ from the central one. This indicates the importance of dipolar interactions. However, there is still a point to be clarified in relation to the temperature at which the experiment on the left panel was performed compared with the temperature used to simulate the results shown on right panel. The experimental data were taken at 50mK while the simulation was computed at a temperature of 600mK. The explanation for this discrepancy is found to be relevant to the entropy measurement discussed in the previous section. Due to the complex interplay of geometric frustration, long range interactions and the fact that collective spin moves do not seem to occur

[4]Similarly for $Ho_2Ti_2O_7$, $J_{Ho} = 1.8$K, $\mu_{Ho} \sim 10\mu_B$, which implies that the nearest neighbour exchange interaction has to be ferromagnetic and of the order of -0.55K.

below 650mK, the dynamics of $Ho_2Ti_2O_7$ and $Dy_2Ti_2O_7$ become very slow when compared with experimental times and eventually, the spin system on these materials freezes out. The freezing was reported in each of the experimental studies made on $Dy_2Ti_2O_7$ and $Ho_2Ti_2O_7$ below 700mK by different experimental groups in laboratories around the world[5].

The sudden freezing of spins explains the residual entropy of the last section: the system dynamics becomes very slow, with long relaxation times compared to measurement times. Hence, the heat capacity as measured on experimental time-scales ceases to represent a thermodynamic quantity of the spin system, because the system is probed in an out-of-equilibrium state (the third law of thermodynamics applies to systems that comply with the first and second laws). In statistical terms, the presence of large energy barriers to hop between states causes the system to lose ergodicity.

In the case of the neutron diffraction experiments, it is not difficult to imagine that if the system freezes in a particular spin ice state, it suffices then with a few layers of uncorrelated configurations to obtain a diffraction pattern similar to the one that would be obtained for an equilibrium configuration in spin ice. In a sense, because of the randomness of the spin ice configuration, different layers can represent different systems altogether, and the diffraction has the effect of averaging over all of them. This property of the diffraction pattern of spin ice is called *self-averaging* [34].

2.2.2 Magnetic Hamiltonian for $Dy_2Ti_2O_7$

In $Dy_2Ti_2O_7$ at low temperatures, spin excitations out of the doublet ground state are exponentially suppressed. The magnetic Hamiltonian can be separated into two parts [21], one with an antiferromagnetic nearest neighbour interaction with $J_1 = -1.24$K, and the other with dipolar long range interaction with $D = 1.41$K (which gives $D_1 = 2.35$K, as shown in the previous section) given by the two following terms,

$$\mathcal{H} = J_1 \sum_{<ij>} S_i S_j + D \sum_{(ij)} \left[\frac{\hat{e}_i \cdot \hat{e}_j}{\mid \mathbf{r_{ij}} \mid^3} - \frac{3(\hat{e}_i \cdot \mid \mathbf{r_{ij}} \mid)(\hat{e}_j \cdot \mid \mathbf{r_{ij}} \mid)}{\mid \mathbf{r_{ij}} \mid^5} \right] S_i S_j, \qquad (2.2)$$

where $\hat{e}_i$ are the easy axes, *i.e.* the axes to which the spins are constrained by the crystal field, and $\mathbf{r_{ij}}$ are the vector distances between pseudospins S_i and S_j. For the sake of simplicity, in this minimal Hamiltonian, higher order interactions have been neglected, but they should be included to obtain better quantitative agreement with experiment if needed, as discussed

[5]University of Tokyo, Kyoto University, Helmholtz-Zentrum Berlin, ISIS Facility Oxfordshire, Pennsylvania State University, Princeton University, among others.

by Yavorsk'kii *et al.* in reference [22]. Furthermore, in equation 2.2, an infinite phonon bath is implicitly assumed. That is, we are assuming that there are phonon states of all the right energies to allow spins to change their energy in a spin flip, and to equilibrate the spin system at a given temperature. Restricted phonon coupling should be included, specially at very low temperatures ($T < 1$K) to account for some of the experiments in part III.

2.3 Frustration and excitations in spin ice

The free energy of $Dy_2Ti_2O_7$, in the region of parameter space where the Hamiltonian of equation 2.2 is valid, can be written as

$$F = U - ST - \mathbf{M} \cdot \mathbf{H} \tag{2.3}$$

where U is the energy coming from that Hamiltonian, S is the entropy, T the temperature, $\mathbf{M}$ the magnetisation and $\mathbf{H}$ the magnetic field.

The competition between the different terms in the free energy dictates the equilibrium state of the system, and the number and type of excitations. For instance, for $T << J$ the ice rules are thermally enforced[6]. In this case, they can only be broken with magnetic field and the main competition is between U and $\mathbf{M} \cdot \mathbf{H}$. Alternatively, if $\mathbf{H}$ is such that it picks a particular configuration, like $\mathbf{H}//[100]$ where all tetrahedra can adopt the 'x' configuration from section 2.1, then at low temperatures the ice rules are mostly conserved throughout the system and the behaviour of the system is given by the competition between $\mathbf{M} \cdot \mathbf{H}$ and ST on the free energy as will be explained in section 2.3.2.

In the following, several examples of the behaviour of the system are illustrated for different values of the external parameters T and $\mathbf{H}$.

2.3.1 Zero field ground state: spin ice manifold

If we consider interactions only to the nearest neighbour, at zero temperature and zero field, the classical ground state of $Dy_2Ti_2O_7$ is the spin ice configuration previously described. The macroscopically large number of spin ice configurations have the same energy and form the spin ice manifold. As the temperature is increased from zero, the energy constraint that fixes the ice rules can be thermally overcome, and excitations out of the ground state appear.

[6] J is sometimes refer to as J_{eff} to account for the effective nearest neighbour interaction that is obtained by the sum of the antiferromagnetic J_1 and the ferromagnetic D_1.

An elementary excitation in spin ice is a single spin flip. The consequence of such is the breaking of the ice rule in two contiguous tetrahedra, at an energy cost of $4J$, ($2J$ for each of them). Note that this excitation does not treat the two tetrahedra equally. After the spin flip, one of them will have 3 spins pointing in and 1 out, and the other tetrahedron will have 3 out and 1 in. In this sense, one can distinguish two kind of defects, which are usually associated a positive and a negative sign respectively. From this excited state, a different spin ice configuration can be obtained, by carrying the first defect around a loop until encountering the second one at the starting tetrahedron. The defect moves by flipping one of the 3 spins pointing in or out of the tetrahedron. This heals the ice rule in that tetrahedron and breaks it in the one sharing the flipped spin. After doing this for a loop of tetrahedra, the ice rules are recovered everywhere but the spin ice state has changed because a closed loop of flipped spins has been left behind the path of the defect.

If the whole dipolar interaction is taken into account there is a unique theoretically proposed ground state. The ordered state that minimises the total energy is given by an alternating stack of planes of up tetrahedra, one in the 'x' ('y') and the other in the '$-x$' ('$-y$') configuration in the direction perpendicular to the z axis. This spin ice order was found by Melko *et al.* [23] by numerically calculating the energy of spin ice configurations where the spins interacted through the Hamiltonian 2.2. The spin ice configurations were obtained by means of a special loop algorithm that, combined with single spin flips, speeded up the calculations in the frozen temperature regime. The transition to this ordered state is predicted to happen at $\sim$ 180mK, and was never measured down to the lowest temperatures achieved in real experiments. We believe that the main reason for this is the freezing of the spins below 700mK, as will be discussed in part III of this thesis.

2.3.2 Field along [100]: strings

Different kinds of excitations can be tuned with an external magnetic field. When a magnetic field is applied along the [100] crystallographic axis, the 'x' configuration is favoured over the others. For a high enough magnetic field all tetrahedra saturate adopting this configuration.

At a finite intermediate temperature, as the field is decreased, the system will lower its magnetisation via entropically favoured excitations. As discussed in the last section, any possible excitation from a pure spin ice state starts with a single spin flip at an energy cost of $4J + MH$, $2J$ for each of the two broken tetrahedra. Take for instance the case of a strong magnetic field enforcing the saturated all 'x' configuration. After the first

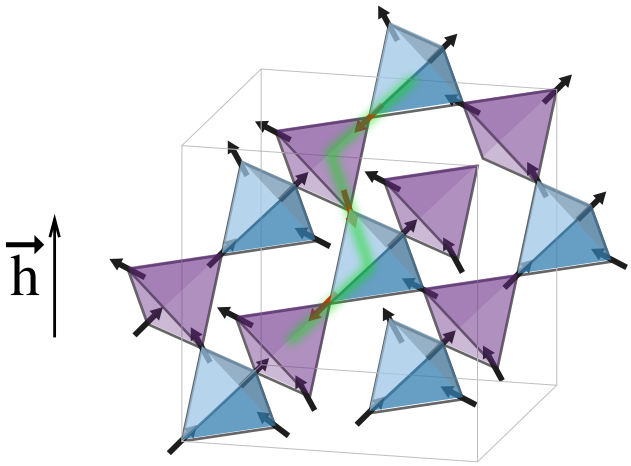

Figure 2.9: String of flipped spins on a background of 'x' tetrahedra. The only two defective tetrahedra in this figure are the ones at the ends of the string. The intermediate spins have flipped with respect to the field direction.

single spin flip[7], the system can choose to flip an independent spin far from it at an equal energy cost, or entropically flip a second spin against the field direction in one of the two tetrahedra to which the first spin belonged. This spin flip is such that the ice rules are restored in that tetrahedron but broken in the neighbouring one as shown in figure 2.9. The first of the processes described has a total energy cost of $8J + 2\mathbf{M} \cdot \mathbf{H}$ and the second one only costs $4J + 2\mathbf{M} \cdot \mathbf{H}$. Evidently, flipping neighbouring spins in this fashion is energetically favourable over flipping unrelated spins. A third spin can be flipped and joined to the last tetrahedron for a total cost of $4J + 3\mathbf{M} \cdot \mathbf{H}$ and, in this way, more spins can be added to elongate the defect at only the cost of magnetic energy to form a *string*.

String formation is an entropically driven process, caused by the competition of $\mathbf{m} \cdot \mathbf{H}$ with $k_B T \log 2$, where $\mathbf{m}$ is the [100] magnetisation per spin and $\log 2$ is the entropy associated with the two possible choices of the next spin on the string opposite to the field direction, that restores the ice rule in the last tetrahedron. The existence of strings is guaranteed by the ice rules whenever they prevail, as discussed by Jaubert *et al.* [24]. These excitations lower the magnetisation from the saturated all 'x'-spin ice configuration to zero, but they only approximately describe dipolar ice.

When the ice rules are not massively broken, *i.e.*, when $T << J$, the

[7]This is only a mental picture, *i.e.*, the first spin flip has to be taken as virtual in the sense that *first* does not necessarily mean before another flip.

dipolar ice description agrees almost everywhere in the crystal with pure spin ice state, with exception of a low density of tetrahedra where the ice rules are broken [25]. With a value of $J = 1.11$K for $Dy_2Ti_2O_7$ the temperature where the string description should work is bound from above at that energy scale. In turn, the experimental freezing temperature bounds it from below given that the entropy quickly dies out below 700mK, as seen in figure 2.5[8]. From these considerations, we see that the ideal temperature for strings to dominate the behaviour of an experiment is given by the lowest possible temperature where the system remains unfrozen on experimental time scales. This poses stringent constraints, perhaps too stringent, for the string picture to describe the spin ice thermodynamics of $Dy_2Ti_2O_7$ under a [100] magnetic field, as will be addressed in more detail in section 6.1. In principle cooling the sample in field from a temperature above the freezing temperature to one below should freeze the system in a particular string configuration. This allows imaging the configuration through some neutron technique.

The transition from saturation ('x') to the string regime when the [100] magnetic field is decreased, was theoretically conjectured to be a case of a very special topological transition, a 3D case of a Kasteleyn transition usually found in 2D systems [26, 27, 28]. This topological transition is very peculiar in the sense that it is not a transition between phases like the ones we are used to. In order to highlight the differences we can compare the Kasteleyn transition with first and second order phase transitions.

In a first order transition two minima of the free energy exist and cross for a given control parameter change in the free energy. As shown in figure 2.10 these minima are disconnected and there are no statistical fluctuations connecting the two states[9]. In that case, the observable macroscopic quantities show a discontinuity in their behaviour at the transition point as exemplified by the magnetisation and the entropy.

Differently, in a second order phase transition, one minimum in the free energy evolves continuously into a pair of minima as a function of some external parameter. In this case, the phases are connected at the transition point, and the transition is driven by fluctuations. The observable macroscopic quantities show a continuous behaviour but a discontinuous derivative at the phase transition (see magnetisation and entropy).

Unlike the previous cases in a Kasteleyn transition there are no phases, as can be inferred from the plot of the free energy in figure 2.10 where there is only one minimum that evolves continuously until the order parameter

[8]Which is equivalent to what is measured in single crystal studies.

[9]Provided of course, that the energy barrier between states is big enough to neglect exponentially damped tunneling across it.

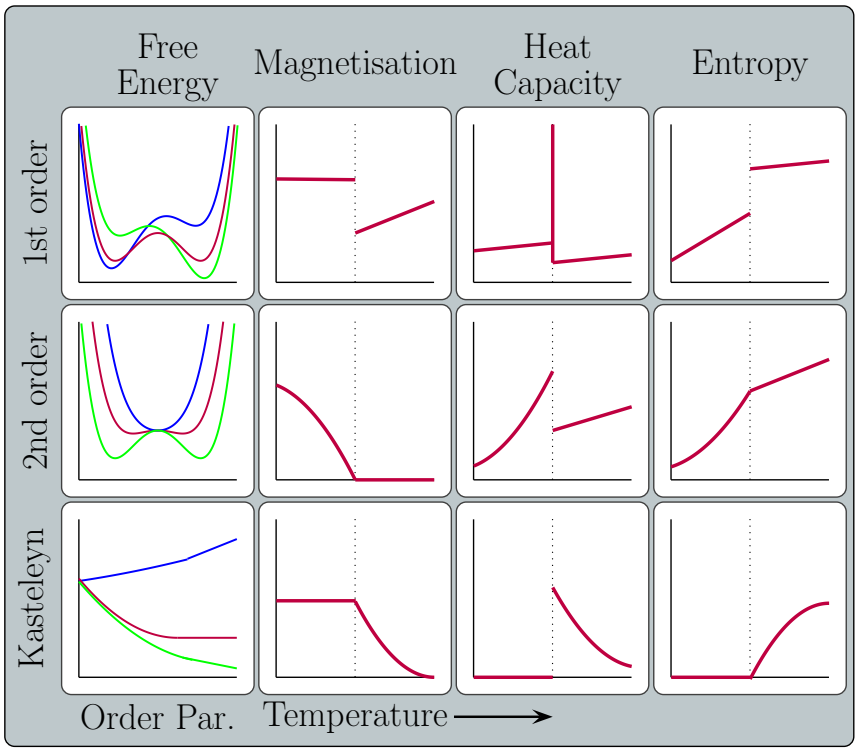

Figure 2.10: Signatures of a 1st order, 2nd order and Kasteleyn transitions as a function of temperature. The magnetisation, heat capacity and entropy of these transitions as discussed in the text. The free energy is plotted as a function of a suitable order parameter, for instance magnetic field, and for decreasing values of temperatures in blue, purple and green.

saturates. In a sense, the transition can be understood as one between a vacuum and an excited state where the excitations are topological. The observables present a very strange kink at the transition; from the vacuum side it looks like a first order transition, because the vacuum is abruptly lost in favour of excitations (zero slope), but from the excitation side it looks like a continuous transition where the excitations are lost gradually towards vacuum (infinite slope). Note from the figure 2.10, that the observables do not behave exactly as a function of temperature as in the cases of either the 1st or the 2nd order phase transitions. The entropy and heat capacity strictly vanish at the transition point, and the magnetisation saturates with positive convexity. This convexity on the magnetisation can be understood from the following consideration. At the transition point from the vacuum side, the free energy of the vacuum and that of creating any number of

excitations becomes equal. The fact that there is no barrier to create any number of excitations is translated into an infinite susceptibility. This is similar to what happens in a type II superconductor at H_{c1} where an infinite susceptibility is measured when the condition of vortex penetration is given. Before reaching H_{c1}, there is a vacuum of vortices on the sample but once it is surpassed the sample fills with them.

In the particular case of strings in [100]-spin ice, the vacuum is represented by the state without strings given by the polarised configuration (all tetrahedra in 'x'). As soon as the strings are entropically favoured over the vacuum, they pierce the material from side to side, driving the change in magnetisation and hence of the rest of the observables.

One last thing to point out is that when a spin is flipped from an 'x' configuration, there are two possibilities for the first spin on the string entering a new tetrahedron, and two for the second spin going out of it, restoring the ice rules. Therefore there are four possibilities for the final state of the tetrahedron after the string has passed through it: 'y', 'z', '$-y$' and '$-z$'. This implies that sweeping the field down from saturation progressively destroys all 'x' tetrahedra but no '$-x$' configurations are generated, at least for low densities of strings when the probability of two strings crossing a given tetrahedron is extremely low[10]. Hence, decreasing the field from saturation gives magnetic contrast ('$\pm y$', '$\pm z$' in a sea of 'x') to image the strings using neutron diffraction techniques as will be seen in chapter 6.1.

2.3.3 Field along [111]: Kagome ice and dimer-monomer transition

Another interesting case is the one where the magnetic field is applied along the [111] direction. In this case, as the field is increased from zero, the '+' configurations, 'x', 'y' and 'z', are favoured over the '$-$' configurations.

The positive configurations have the property that in them, the [111] spins belonging to the triangular plane, dubbed 'apical spins', are collinear with the magnetic field, and the other three spins belonging to the Kagome plane, referred to as 'basal spins', have a projection of $\pm 1/3$ on the field direction. At intermediate fields the '+' configurations are adopted for all tetrahedra, and besides the fact that they do not present the maximal magnetisation compatible with the crystal field at low temperatures, this state persists for a wide range of field values, generating a plateau in magnetisation as can be seen in figure 2.11. These configurations belong to a macroscopically degenerate manifold due to the remaining freedom of the basal spins. The

[10] Two strings across an 'x' tetrahedron turns it into a '$-x$'.

'+' configurations gathered under the name of Kagome ice, refer to the ice state constrained to the Kagome degeneracy.

The physics behind spin ice with a magnetic field in the crystallographic [111] direction is summarised in figure 2.11 where the magnetisation as a function of magnetic field is shown for different temperatures as measured by Sakakibara *et al.* [29]. In equilibrium, at zero field there is the same amount of any of the six possible configurations for the tetrahedra, and hence, the magnetisation is zero. At intermediate fields, when all apical spins have already flipped and point along the field direction, the magnetisation plateaus [30] at the value $3.33\mu_B$/Dy that corresponds to

$$\frac{M}{\mathrm{Dy}} = \frac{(\overbrace{1}^{apical} + \overbrace{1/3 + 1/3 - 1/3)}^{basals}}{4\mathrm{Dy}} \times 10\mu_B = 3.33\frac{\mu_B}{\mathrm{Dy}} \tag{2.4}$$

where the spin projections along the field have been added up for a tetrahedron and divided by the number of spins (Dy atoms). Note the signs in the sum: a positive sign for the apical spin makes it point out of an up tetrahedron, and two positive basal spins point into an up tetrahedron opposite to the negative spin, therefore enforcing the ice rule: two in, two out. The three possible configurations per tetrahedron on the Kagome ice come from assigning the minus sign to a different basal spin. The Kagome plateau ends when the magnetic field is large enough to flip out of the spin ice manifold the last basal spin opposing the magnetic field in each tetrahedron.

Hiroi *et al.* [31] inferred the reduced degeneracy of the Kagome ice from specific heat measurements with the magnetic field tuned to the Kagome plateau. These data were integrated up to give the entropy shown in the top left corner of figure 2.11. The value obtained is in agreement with the theoretical value calculated by Udagawa *et al.* [32]. A different approach was taken by Tabata *et al.* [33] who studied the Kagome ice state by means of neutron diffraction and compared the data with Monte Carlo simulations for spin ice and dipolar ice models. This work concluded that for intermediate fields (0.5-0.8T), spins in $Dy_2Ti_2O_7$ freeze in a state that belongs to the Kagome manifold, and that the dipolar interaction slightly perturbed (lifted) the degeneracy.

When the magnetic field reaches an energy scale for which the magnetic energy gained by flipping the last spin pointing opposite to the field direction is comparable to that of breaking the ice rules, *i.e.*, when $2\mathbf{M}_{bas} \cdot \mathbf{H} \sim 2J$, the magnetisation increases towards saturation. In the bottom right corner of figure 2.11 the magnetisation below 400mK is shown. A finite hysteresis in magnetisation was measured at 50mK, 190mK and 370mK, from which a first

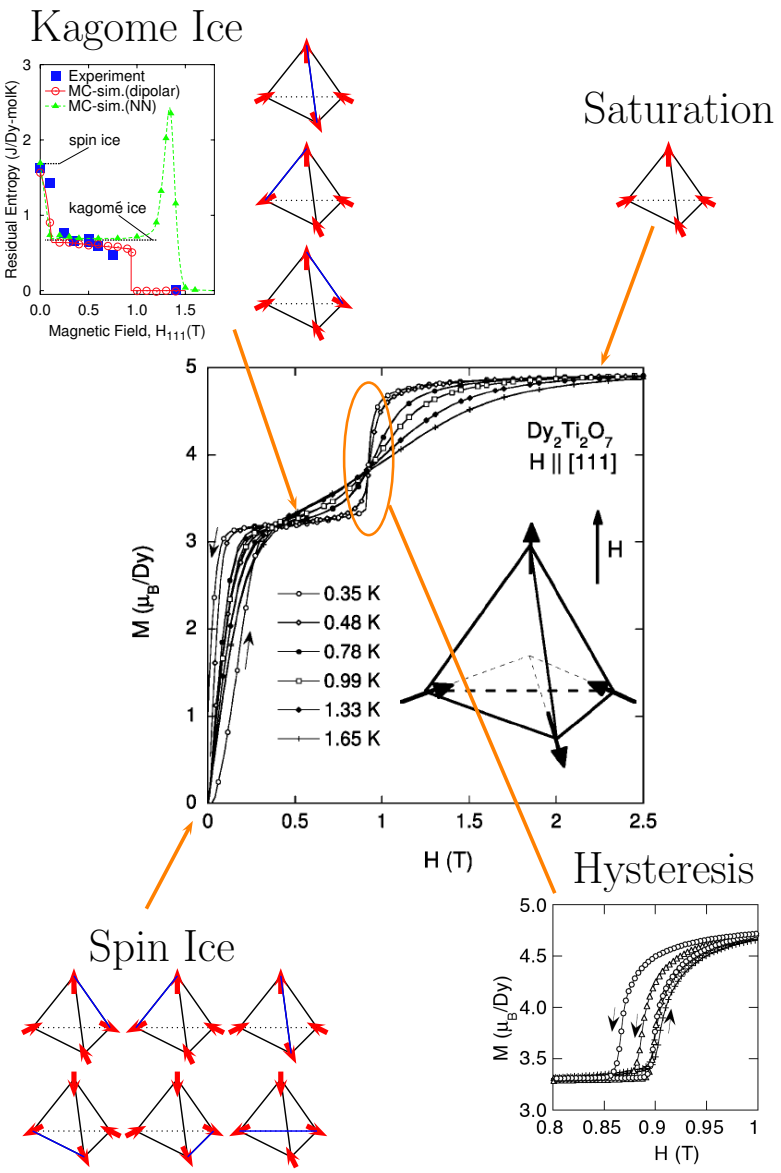

Figure 2.11: Magnetisation as a function of field in the [111] direction. At low fields, all six degenerate possibilities for spins in a tetrahedron are present. At intermediate fields the system polarise the apical spins, leaving only the '+' configurations explained in the text. This is the Kagome ice plateau whose entropy still differs from zero (top left figure). (From Tabata *et al.* [33] Copyright©(2006) by the American Physical Society). Upon further increasing the field, all tetrahedra saturate their magnetisation. Below 400mK this process presents hysteresis . (From Sakakibara *et al.* [29] Copyright©(2003) by the American Physical Society)

order phase transition, like the liquid-gas transition of water, was inferred [29]. This transition has a critical end point in the (T, H) plane at a finite field very much like metamagnets.

A substantial amount of work has been devoted to understanding this transition. This work ended up with the first validation of the monopolar mapping, by a comparison of the experimental results with those of Monte Carlo simulations [34, 35, 36].

Before the monopolar picture was proposed, Moessner and Sondhi [34] argued that, in the Kagome ice state, the Kagome planes were decoupled, and that the polarised triangular planes of apical spins could be neglected for the study of the transition from Kagome ice to saturation. Each Kagome plane was then mapped to a hardcore dimer covering of the honeycomb lattice (Kagome's dual lattice), and the transition to saturation was predicted to be the transformation of dimers into monomers. In their analysis, a nearest neighbour model was assumed and the resulting crossover to saturation lacked the sharpness of the one in figure 2.11. This approach predicted a 2D Kasteleyn transition on the Kagome planes for fields slightly misaligned away from the [111] crystallographic direction in the nearest neighbour model. The correlation functions associated with this transition were later experimentally verified using neutron scattering on $Dy_2Ti_2O_7$ by Fennell *et al.* [37], showing that the essential physics of this material was captured in the simple nearest neighbour model.

Further theoretical work on the same topic by Isakov *et al.* can be found in reference [36], where the entirety of the magnetisation process with the field in the [111] direction was addressed. In this case a giant magnetocaloric effect was predicted for the Kagome-to-saturation transition of the nearest neighbour model as a consequence of the crossing of energy states from both sides of the transition. The explanation for this is that the Kagome ice degeneracy with all its entropy crosses over with the possibility of excitations out of the manifold, enlarging the available phase space. Aoki *et al.* performed a magnetocaloric effect experiment on $Dy_2Ti_2O_7$ [38] and showed that the entropy jump, although sizeable, was notably smaller than the one predicted, and attributed the reduction to dipolar correlations. Furthermore, in Monte Carlo simulations the transition to saturation becomes a first order only when dipolar interactions are taken into account, as will be discussed in part III.

To summarise, we show in figure 2.12 the phase diagram H-T (H//[111]) obtained by Higashinaka *et al.*[41] through specific heat measurements. The spin ice configuration prevails at low fields and low temperatures **(A)**. As the temperature is increased beyond the scale of the nearest neighbour and

dipolar interactions, the system behaves like a paramagnet **(B)**. If the field is increased from the spin ice in **(A)**, the first spins to flip are the apical spins that oppose the field direction. This leads to the Kagome ice state in **(C)**. If the temperature is increased from **(C)** towards the **(D)** region, the apical spins continue to be aligned along the field direction but the temperature randomises the basal spins (1-3 configuration).

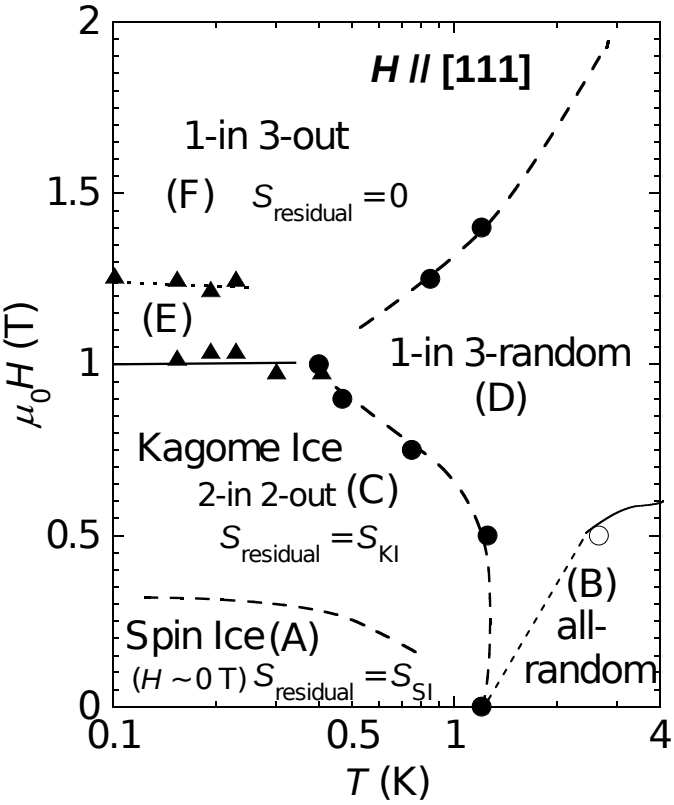

Figure 2.12: H-T phase diagram of $Dy_2Ti_2O_7$ with the field along the [111] direction. The circles and the triangles are experimental peaks measured by means of specific heat. **(A)** spin ice (2 in, 2 out), **(B)** paramagnetic behaviour, **(C)** Kagome ice (2 in, 2 out with the apical spin aligned with the field.), **(D)** apical spin aligned with the field but the temperature high enough to randomise the basal spins (1-3 configuration), **(E)** second peak seen in specific heat and susceptibility (probably caused by misalignment, see figure 2.13) and finally **(F)** saturation with the ice rule broken. (From Higashinaka *et al.*[41]).

Finally, if the field is high enough as in **(F)**, it causes saturation of the

magnetisation with all the spins pointing along the field direction (within the crystal field constraints). In this case, the ice rules break down, and the entropy of the Kagome state is released.

Although not strictly in the [111] direction, several experimental groups have performed very interesting experiments, with the possibility of varying the relative orientation of the magnetic field with respect to the sample crystal axis *in situ* by the use of vector magnets. These experiments yielded the angular dependence of different transitions. In particular, Higashinaka and Maeno [40] studied a ferromagnetic transition that demonstrated the existence and importance of the long range part of the dipolar interaction.

In their experiment, spins on the Kagome planes were fixed by applying a strong magnetic field along the $[\bar{1}\bar{1}2]$ direction, and ac-susceptibility as a function of [111] magnetic field was measured. The experiment was performed at low enough temperatures to indirectly fix the apical spins through the ice rule. When the perpendicular field was increased along [111] it was found that the apical spins flipped all at once at about 0.3T, a value that could only be explained by invoking long range interactions because the apical spins are third nearest neighbours. This is another confirmation of the importance of the dipolar interaction.

Sato *et al.* [39] performed a field angle study of the magnetisation in order to determine the origin of the gas-liquid transition seen in magnetisation. In their work, the field was moved in the plane containing [110], [111] and [112]. The findings of this experiment can be summarised in the top two panels of figure 2.13. When the field is moved away from [111] towards [112], the static susceptibility develops a second peak for the transition from Kagome ice to saturation, which evolves with angle until it vanishes for angles beyond 10° (right panel). Unlike for the latter tilting, when the field is moved towards [110], there is no trace of a second peak (left panel).

The bottom panel of figure 2.13 shows the critical fields as extracted from static susceptibility and magnetisation measurements. It can be seen that a critical field branch continuously connects the first peak at zero angle from [111] to the one at [112], corresponding to the transition measured in the previously discussed reference [40]. One can see that the nearest neighbour model (thick line on the figure) reproduces qualitatively the angular dependence of the transition field for $J = 1.01$K, except for the splitting of the transition into two. This splitting has been also reported in specific heat measurements by Higashinaka *et al.* [41] (**(E)** region in figure 2.12), and its microscopic origin remains an open issue that will be addressed in chapter 9.

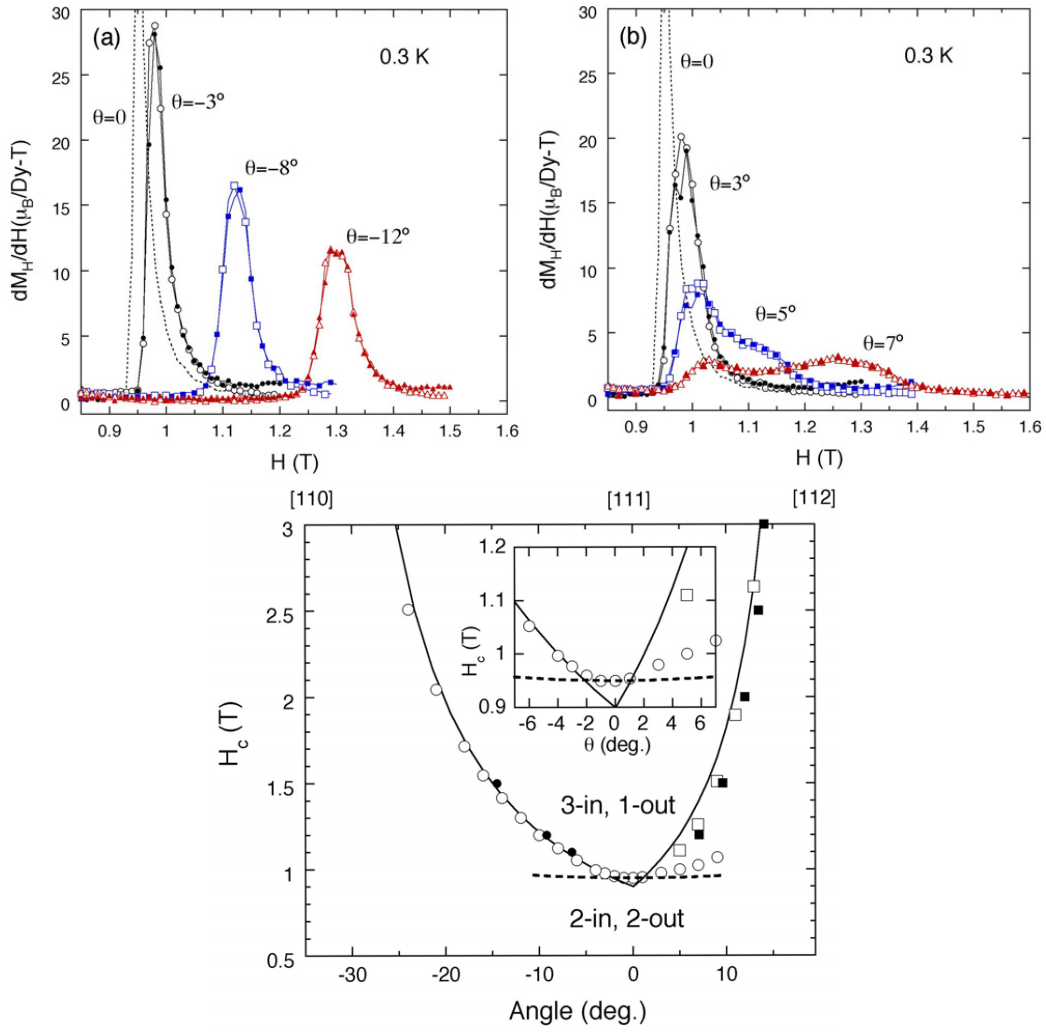

Figure 2.13: **Top**: static susceptibility as a function of field around the Kagome ice to saturation transition for different tiltings from the [111] direction at 300mK. The left panel shows the tiltings towards the [110] direction, and the right panel towards [112]. The static susceptibility in the latter develops a second peak for the transition from Kagome ice to saturation, which evolves with angle until it vanishes for angles beyond 10°. **Bottom**: critical fields extracted from static susceptibility (open points) and magnetisation (full points) at 300mK. The continuous curve traces the critical fields for different tilting angles extracted from a Monte Carlo simulation of the nearest neighbour model with $J = 1.01$K. It can be seen that a critical field branch continuously connects the first peak at [111] to the one at [112]. (From Sato *et al.* [39])

2.3.4 Monopoles

In early numerical studies it was noted that the experiments on $Dy_2Ti_2O_7$ could be satisfactorily reproduced by the implementation of single spin flip dynamics in numerical Monte Carlo simulations. As discussed before, a single spin flip out of the spin ice ground state is the most basic excitation that the system can have and has the consequence of breaking the ice rule in two contiguous tetrahedra. As it was shown in section 2.3.2, these defects coming from a single spin flip can fractionalise into two defects, moving apart from each other by creating a string of magnetisation which predominantly opposes the field direction, for an external applied magnetic field.

Recently, a very important step forward in the theory of $Dy_2Ti_2O_7$ was made when it was understood by Castelnovo *et al.* [35] that in dipolar ice, the string tension for a string configuration with two defects at its ends was zero due to the ice rules. More importantly, they realised that the whole energy cost of the separation of defects could be calculated, to a very good approximation, from the interaction of the defects themselves.

The reasoning behind these statements can be understood by comparing dipolar ice to an array of magnets. Similarly to a magnet that is elongated by the insertion of magnets at its ends (north and south poles head-to-tail), defects in dipolar ice interact via a long range Coulomb **(E)** interaction. However, the high degeneracy of the ice rules permits the line of spins joining the defects to be defined over tetrahedra where the ice rules are fulfilled, representing no extra cost to fractionalisation other than the Coulomb interaction for separating the defects at the end.

To understand the novelty of this phenomenon in condensed matter physics, let us compare it to excitations in an Ising ferromagnet on a square lattice (figure 2.14). Starting from a polarised ferromagnet a first spin is flipped creating a defect. The defect can be elongated by flipping a second spin next to it. This second spin will heal the ferromagnetic interaction with the first while introducing an energetically costly domain wall around it. When the total energy of the defect is computed, an extra domain wall energy has to be added to the monopolar interaction between the ends of the defect due to the spins surrounding the flipped spins. In the case of dipolar ice, the intrinsic degeneracy of the spin ice manifold allows defects to fractionalise without creating a domain wall (a domain wall is generated by violation of the rule only), hiding it on the spin ice manifold. Because these defects interact through a Coulomb law, they were dubbed 'monopoles'.

In the monopolar picture, spins on the pyrochlore lattice are mapped to dumbbells with positive and negative charges. These charges replace the heads and tails of the virtual vectors with the direction of the spins, and

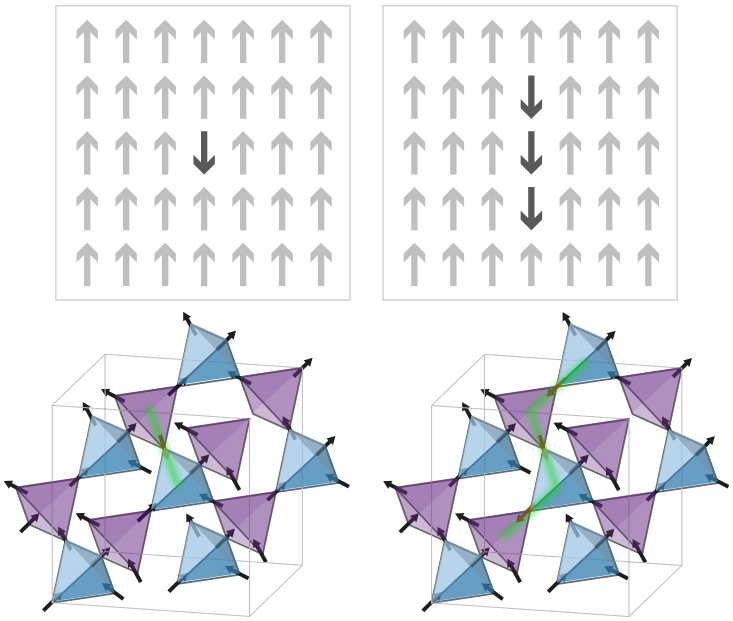

Figure 2.14: Comparison of defects in dipolar ice and in a ferromagnet. In an Ising ferromagnet on the square lattice (top panels) a spins can be added at the end of a string of spins that were flipped from saturation. On top of the Coulomb energy associated to the elongation of the strings, the energy contains also the energy for domain wall creation. In the case of spin ice (bottom panels) there is no creation of domain walls when the strings are elongated by adding spins to it (a domain wall is generated by violation of the rule only). As can be seen in the figure, the ice rule in the tetrahedra containing the defects on the left, are fixed when the string is elongated beyond them (right).

join the centres of the two tetrahedra to which the spins belonged. Hence, the dumbbells sit on the conjugate lattice to the pyrochlore, the diamond lattice. In the ground state, the ice rules constrain the total charge on each site of the diamond lattice (inside each tetrahedron) to sum zero, given that there are two heads and two tails pointing to each site (two positive and two negative charges), see figure 2.15. As discussed before, the elementary excitation of the system breaks the ice rules by flipping a single spin out of the spin ice manifold, or in monopole terms, creating excess of charge in two contiguous sites giving rise to a dipole in a vacuum of charge. This dipole can be elongated with zero domain wall cost at the only expense of separating two charges forming an even longer dipole. The overall energy cost of this process leads, therefore, to a Coulomb type interaction. In figure 2.16 the

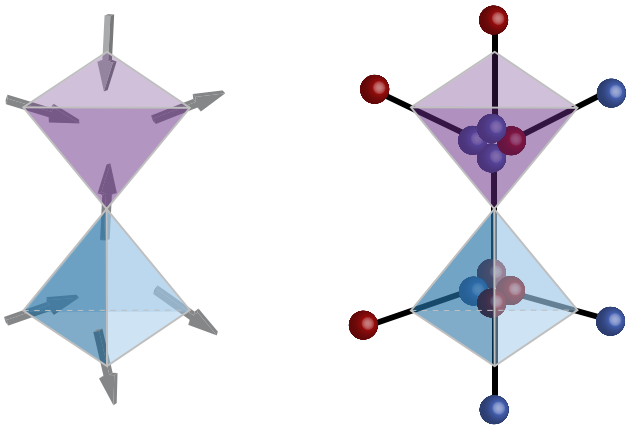

Figure 2.15: Illustration of the mapping from spins to dumbells. A defect in the spin system maps to unbalance of charge in the dumbbell picture.

original computation of the energy between monopoles is reproduced. To obtain it, a pair of monopoles of opposite charge were pulled apart in an spin ice background fulfilling the ice rules. The energy difference was then computed for the dipolar model equation 2.2.

The monopole charge can be easily constructed to match the spin strengths from the lattice dimension and the intrinsic magnetic parameters. It turns out to be $Q = 2\mu/a_d \sim 4.6\mu_B \text{Å}^{-1}$ with $a_d = \sqrt{3/2} r_{nn}$ the diamond lattice parameter and μ the magnetic moment of the spins.

At small distances, where the fine structure of the dipolar origin of the dumbbells is of importance, the monopolar mapping breaks down. The multipole correction to the picture are $O(1/r^5)$ terms that have to be added to the Coulomb interaction.

Monopoles offer the first analytical quantitative way to deal with the long range part of the dipolar interactions in spin ice. In this way, many previous results can be reinterpreted in the simple monopolar language. For instance, the ground state of dipolar ice corresponds to the absence of monopoles. In the case of the field applied along the [100] discussed in section 2.3.2, the defects at the ends of the strings can be thought of as monopoles. In the case of section 2.3.3, the Kagome ice-to-saturation transition is a first order transition that only appeared in the Monte Carlo simulations when the proper dipolar interaction was taken into account. Using monopoles, on the other hand, this transition can be thought of as a solidification of monopoles into an ionic crystal. The experiment of Higashinaka and Maeno of reference [40] can be interpreted in a similar way.

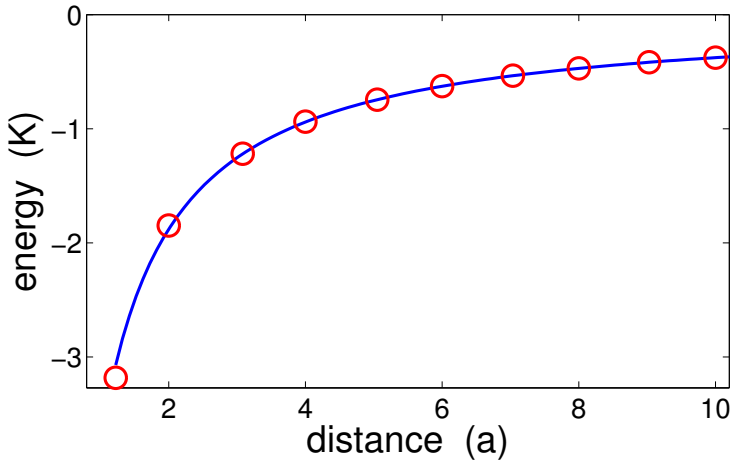

Figure 2.16: Energy needed to separate a monopole pair in a spin ice background. (From Castelnovo *et al.*[35])

Several experiments were specially designed and carried out to probe the validity of the monopolar picture [16, 42, 43, 44].

It is important to note that the monopole picture is only approximately correct, and does not provide a way to take into account the full dipolar interaction. For instance, two monopoles in an infinite spin ice background have a given total energy that changes when an infinite string of spins is flipped, even though this can be done without creation or movement of the monopole. The reason for this is the change in dipolar energy between the spins of the string and all the rest. A similar situation occurs when spins are flipped in a closed loop free of monopoles. The energy of the system can be changed due to dipolar terms, without affecting the configuration of monopoles.

2.4 Dynamics

In order to learn how to manipulate monopoles, it is interesting to study the dynamical behaviour of these excitations over parameter space, from high to low temperatures, and as a function of magnetic field.

The dynamics of dipolar ice was tested in a series of magnetic susceptibility experiments by Snyder *et al.* [45, 46, 47, 48], where the real and imaginary (χ' and χ'') part of the magnetic susceptibility were measured as a function of frequency, field and temperature. These experiments provided the theoreti-

cal community with the relevant dynamical parameters of $Dy_2Ti_2O_7$, namely the relaxation time as a function of temperature and magnetic field. The zero field experiments can be summarised in figure 2.17 from reference [45] where the spin relaxation time, as obtained from the inverse of the frequency at which χ'' has its maximum, is plotted as a function of temperature.

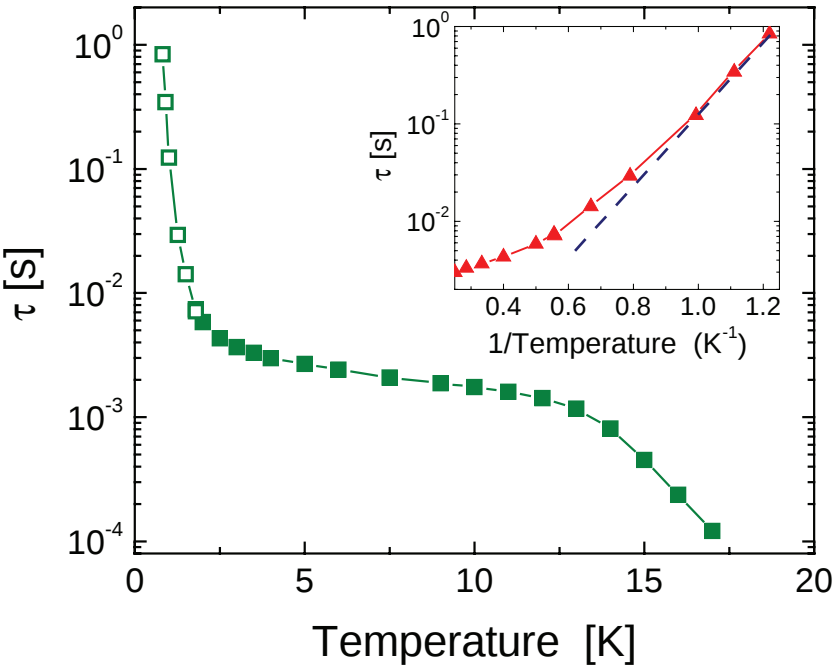

Figure 2.17: Temperature dependence of the spin relaxation time obtained by AC magnetic susceptibility. Full and empty symbols differ in the experimental setup used to obtained low temperatures (PPMS and dilution refrigerator). The high and low temperature regimes are thermal activated processes with an exponential decay for the inverse temperature (Ahrrenius). The intermediate regime shows a temperature independent plateau. **Inset**: low temperature behaviour plotted in Arrhenius form. (From Snyder *et al.* [45] Copyright©(2004) by the American Physical Society)

Three different regimes can be distinguished as a function of temperature; the high temperature part, with an exponential inverse temperature dependence typical for an Arrhenius process of thermal activation; an intermediate regime almost temperature independent; and a low temperature regime that again, depends exponentially on inverse temperature.

The energy scale of the Arrhenius fit for the high temperature regime (above 12K) is 210K consistent with the crystal field energy and is associ-

ated with thermally assisted transitions between different crystal field states (figure 2.7) [47].

The intermediate and low part of the low temperature regimes were studied and explained by Jaubert and Holdsworth [49] through a careful comparison of relaxation times, Monte Carlo simulations of the dipolar ice model and theoretical arguments, with the twofold reward of explaining the data and settling the bases for time dependent Monte Carlo simulations. For intermediate temperatures, between 2K and 8K, they found that a multi-energy Arrhenius law fitted with a relaxation time of $\sim$ 2ms, accurately described the data of references [45, 50]. The energies were taken from a partition function that took into account all possible configurations of contiguous independent tetrahedra. The low temperature regime below $\sim$ 2K was explained using simulations for which the experimental data at intermediate temperatures were used to fix the Monte Carlo time scale. In Monte Carlo simulations, the Monte Carlo time lacks any physical meaning unless the correct dynamics is used to flip the spins. In the case of the low temperature regime, the agreement between the fit of the experimental data and the simulation of a single spin flip dynamics was taken as evidence of such dynamics.

The mapping to monopoles was compared to the full dipolar model by the same authors [50] who found that, due to the high concentration of monopoles in the intermediate regime, the long range part of the Coulomb interaction is cut off by Debye screening, leaving mainly the nearest neighbour part unscreened. This explained why, and quantified the extent to which, the nearest neighbour model successfully reproduced experiments in the moderate temperature regime. This conclusion was also experimentally confirmed by Fennell *et al.* [43] using polarised neutron scattering.

A different aspect of the dynamics was explored theoretically by Castelnovo *et al.* [25] who investigated out-of-equilibrium thermal quenches by means of Monte Carlo simulations. This work stressed the existence of two different relaxation times when the temperature was rapidly lowered from 10K to very low temperatures. The first and faster relaxation is associated with the defects that can easily recombine and annihilate. The second relaxation relates to the generation of trapped defects upon a quench. These defects are given by a pair of contiguous monopoles that cannot annihilate by flipping their shared spin. They can only disappear by flipping spins in a loop of at least six spins, similar to the one discussed in section 2.3.1. These two relaxation times have not been measured experimentally at the time of writing this dissertation.

Part II

Methods

Chapter 3

Experimental Methods

This thesis is mainly based on the experimental work performed at the University of St Andrews, United Kingdom during the years 2007-2010. Also, neutron scattering experiments have been performed in the Helmholtz Zentrum in Berlin, Germany during the year 2008. The single crystals analysed during these three years, were grown, characterised and measured in house and through the SUPA collaboration at Edinburgh University, United Kingdom.

The main probe used to characterise the spin ice system was magnetisation at low temperatures. For this purpose we have developed a new magnetometer design to obtain the desired levels of sensitivity in our experimental equipment (cryostat and magnet system). For the analysis, numerical Monte Carlo simulations were performed in a computer cluster from the group of computational physics at La Plata, Argentina.

In the following we present the experimental and numerical methods used throughout this thesis with the exception of neutron scattering which will be presented in detail in a following chapter (section 6.1).

3.1 Sample preparation

We have grown single crystals of pure $Dy_2Ti_2O_7$, and of the corresponding 1% and 5% Gd and Y doped compounds[1] by the floating zone technique in an image furnace from NEC machinery company (model SCI-MDH), following the main guidelines of reference [51]. The image furnace is composed of a pair of semi-ellipsoidal mirrors that concentrate the power of two light sources placed in their focuses, into a very narrow region of space as illustrated in

[1] I grew these samples to perform a set of experiments that did not take place due to time contraints.

figure 3.1. In this region a sintered rod made out of a previously reacted polycrystal is melted, and fed to a counterrotating seed of the same material.

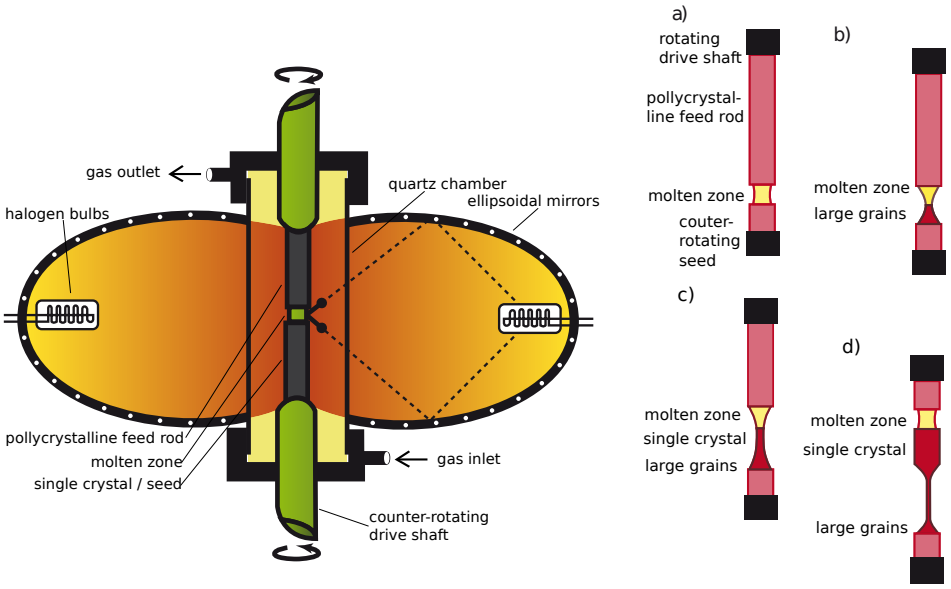

Figure 3.1: **Left**: schematic view of an image furnace. Two semi-ellipsoidal mirrors focus the light from two halogen bulbs in the centre of a quartz tube containing the polycrystalline powder that will be converted into a single crystal. **Right**: floating zone technique. **a)** a polycrystalline feed rod is approached to the melting zone by a rotating shaft until touching the counter-rotating seed. **b)** the seed and the feed are slowly pulled down through the melting zone generating large polycrystalline grains. **c)** and **d)** finally a single crystal starts growing out of the large grains.

In our case, the reaction was done from dry powders of the oxides Dy_2O_3 and Ti_2O (with a small amount of Gd_2O_3 and Y_2O_3 for the doped compounds) that were mixed stoichiometrically. These mixtures were then sintered into a rod of about 10cm length, which was baked for 5 days at 1200°C. Powder X-ray diffraction was used to characterise the crystallinity of this feeding rod (see figure 3.2). The method of refinement was used to determine the crystal structure. This procedure confirmed the purity of the rod to be better than 97%. From the reacted rod, a single crystal was grown in the image furnace. To avoid oxygen deficiency this was done under an atmosphere of 90% oxygen and 10% argon. The crystals tended to grow in the [110] direction at a relative high speed of $20 - 30$mm/hour. The final crystals were amber in color (inset of figure 3.2).

For different experiments, the samples were aligned in the direction of interest using a Laue X-ray camera (at Edinburgh University) with a goniometer that could be fitted into a wire saw which produces accurate cuts of the samples into their final shape to obtain the desired crystallographic direction and crystal shape.

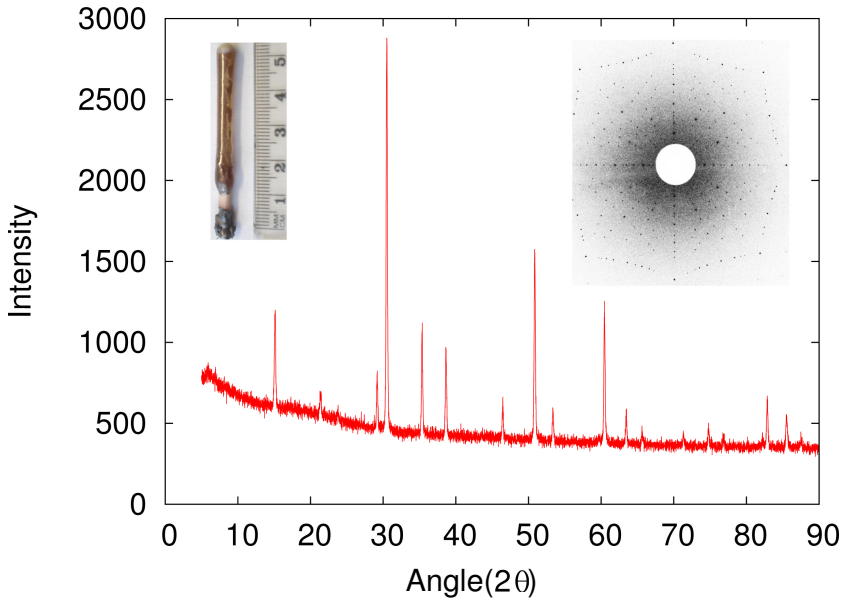

Figure 3.2: Laboratory X-ray pattern as a function of angle showing the $Dy_2Ti_2O_7$ crystalline structure. **Inset**: on the top left a typical single crystal just after growth. On the top right, a reflection-Laue picture of a single crystalline sample.

3.2 Bulk magnetisation measurements

There are many methods to measure magnetisation [52]. Figure 3.3 illustrates the different aspects of magnetisation and enumerates the probes that are commonly used to measure them. The first distinction comes from whether the methods are used to measure surface or bulk magnetisation. Examples of the former are: Superconducting Quantum Interference Device (SQUID) on a tip [53], and Hall probes. The latter can still be subdivided into local and global probes. On one side, local bulk magnetisation is measured by probes that interact with the magnetic local environment inside the sample. Representative of these are muons, Mössbauer spectroscopy, electron para-

magnetic resonance (EPR), nuclear magnetic resonance (NMR), etc. On the other side, global bulk magnetisation refers to the response of the whole sample to the stimulus of an external magnetic field, and is measured by inductively coupled probes such as SQUID, Vibrating Sample Magnetometry (VSM) and Field Modulated Susceptibility (FM). Different kinds of probe used to determine global bulk magnetisation are those that sense the force a magnetic sample experiences in a magnetic field gradient. The main representative of this class is called Faraday Force Magnetometry and it is the core of this thesis. A somehow different probe is Neutron Scattering in which the magnetic structure is directly imaged in reciprocal space. In some sense

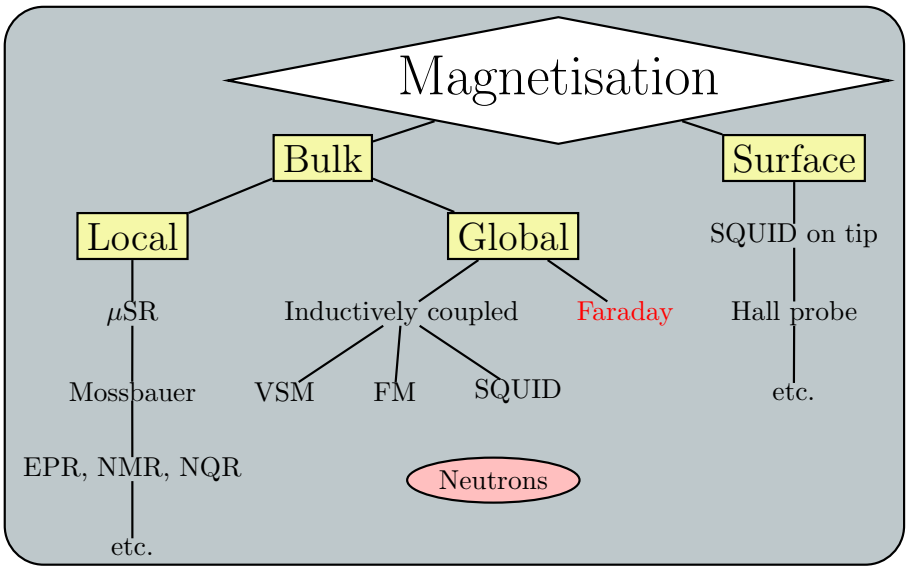

Figure 3.3: Classification of common experimental methods to measure magnetisation and the different aspects of it. Neutron techniques occupy a special place in the diagram given that different techniques using them can measure different aspects of the magnetisation (see text).

this bulk probe is local, but if the structure is known then the global magnetisation can be calculated from the intensity of the magnetic Bragg peaks. Also, neutrons can be used to measure reflectivity, in which case they are used to measure magnetic surface profiles.

In the following we describe the two main methods usually used in the laboratory to measure global bulk magnetisation:

Inductively coupled methods. In these, the sample is inserted into a coil and the magnetic induction is measured by either modulating the magnetic

field (Field Modulation)[2] or moving relatively to each other the sample/coil in an oscillatory fashion (Vibrating Sample Magnetometry/Vibrating Coil Magnetometry) [54, 55]. Although both these alternatives have been successfully applied over large temperature regimes, they are less suitable for sub-Kelvin temperatures where eddy current heating can affect the measurement. These problems are usually overcome at the expense of using dilution refrigerators with large cooling power and/or loss of simplicity on the probes. Another drawback is that the measurements are inherently oscillatory which limits the rate at which the magnetic field is swept and the power that the mixing chamber can stand at a given temperature of the setup. Another possibility is the use of extremely sensitive SQUIDs for the read-out. This, although suitable for low temperatures, is relatively slow and difficult to implement for high magnetic fields.

Force methods. In this case the magnetisation, **M**, is determined by measuring the force (per unit volume) that a magnetic sample experiences in an inhomogeneous magnetic field by means of a Faraday balance. The magnetisation is extracted using the equation

$$\mathbf{F} = \mathbf{M} \cdot \nabla \mathbf{B} \tag{3.1}$$

where **B** is the external inhomogeneous field and **M** is assumed to be homogeneous[3]. The different alternatives of the Faraday force method refer to the implementation of the balance and that of the gradient field.

In the high cryogenic temperature regime, a balance with an arm compensated at room temperature, and the other arm in the cryogenic environment has been generally used. For the sub-Kelvin regime, piezoelectric cantilevers (torque magnetometry see [56] and references therein) and capacitive balances [57, 58] have been implemented. In the latter, the whole experimental setup resides within the cryogenic environment which avoids the heat leak implied by balancing at room temperature. **M** is sensed by the change of the capacitance between two parallel plates, one fixed and the other movable. The force exerted on the movable plate by a sample attached to it (equation 3.1) is compensated by the restoring force of a spring. The correct operation of this kind of magnetometer is based on the assumption that at low temperatures the elastic constant of the spring generating the restoring force is temperature independent. A reliable measurement over a large temperature range could only be obtained by calibrating the magnetometer response with temperature.

[2] Although the outcome of this method is a response function because the sample is perturbed by the external field, in several cases the magnetisation can be extracted from it.

[3] Strictly, $\mathbf{F} = \nabla(\mathbf{M} \cdot \mathbf{B})$

The main drawback of any of the capacitive force methods is the mechanical stability of the movable platform against torque which affects the parallelism of the capacitor plates.

Regarding the generation of the magnetic field gradient, several approaches have been implemented. Dedicated Helmholtz coils for gradient generation were reported by Sakakibara *et al.* in reference [58], with linear gradients of up to 10T/m. For the case where a second set of coils is lacking, the stray field of the main coil is usually used as the gradient field by off-centering the sample. This method does not offer much control given that the stray field increases linearly with the applied field. Another variant was developed by Sakon *et al.* [59] where a film of Nickel was deposited a few millimeters below the magnetometer and then magnetised. This technique gives a gradient field peaked at 5T/m that varies rapidly with distance, and therefore, only allows measurement of small samples.

In the course of this thesis, we used a commercial Magnetic Property Measurement System (MPMS-SQUID) to measure the magnetisation of the different samples in the range 300-1.8K. For measurements at temperatures below 4K, a home built Faraday force magnetometer was developed following the design made in reference [58]. This will be referred to as the *'brass magnetometer'*.

One of the advantages of the Faraday method is that the magnetisation measurement can be integrated with other measurements [60]. This is because the balance of the probe can be used as the platform for a non-magnetic implementation of a second simultaneous experiment. With this concept, and based on our previous experience using the design of the capacitive magnetometer of Sakakibara *et al.*, we have developed a simple Faraday force magnetometer for the specific purpose of measuring the magnetisation and the instantaneous temperature of the sample. The magnetometer was designed to allow the magnetic field to be swept faster without heating the set-up. This second version based on the experience with the brass magnetometer was also developed to meet the requirements of the facilities at St Andrews University and will be referred to as the *'plastic magnetometer'*.

3.2.1 Brass magnetometer

The brass magnetometer of Sakakibara *et al.* [58] consists of a brass annular body used to clamp a pair of phosphor-bronze wires which are crossed at right angle at the centre. In figure 3.4 a schematic view of it is depicted. In this two pairs of wires are fixed at different z-positions (z being the symmetry axis of the magnetometer). The function of the second pair of wires is to help

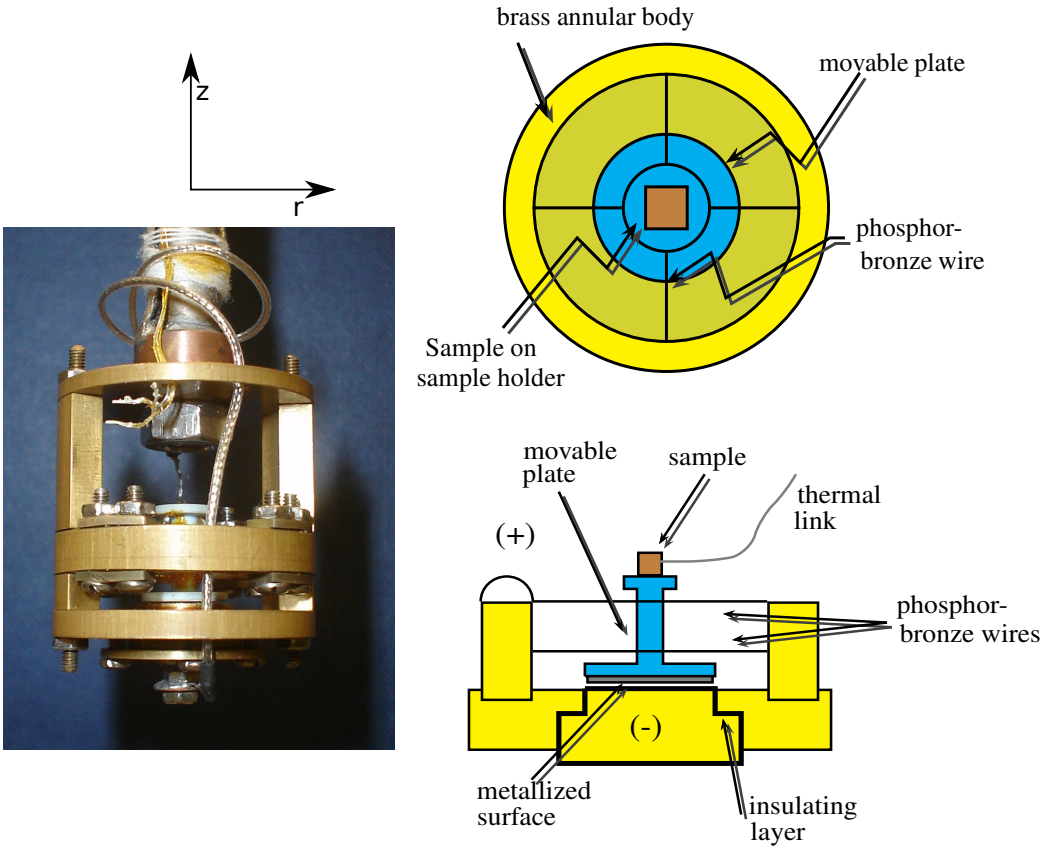

Figure 3.4: Photograph and diagram of the brass magnetometer. **Top view**: the plastic sample holder is suspended by a pair phosphor-bronze wires piercing it at right angles. **Side view**: a second pair of phosphor-bronze wires is included at a different height (one can only see one wire of each pair in this diagram). The movable plastic capacitor plate is painted with metallic paste at the bottom of the sample holder, and the fixed plate (represented by (-)) is isolated from the body by an insulating layer.

suspending the sample holder at the centre by preventing lateral deflections due to torque.

The sample holder made of Tufset plastic (Tufnol Composites Limited) is designed to accommodate one of the capacitor plates which is painted with metallic paste at the bottom. The sample space is located at the top part. In this design, when a magnetic sample is placed in a magnetic field gradient, the force that it experiences is compensated by the deflection of the wires, and the capacitance between the movable plate and the body changes. The capacitance is measured with a capacitance bridge (AH2500A, Andeen-Hagerling) which allows the magnitude of the displacement Δz to be inferred. This Δz, for small enough deflections, has a linear dependence on the force, and is therefore proportional to the magnetisation. The bottom plate of the plastic sample holder is painted with conductive silver paste (4929N, Dupont). In this way this surface is metallised to form the movable plate of the parallel plate capacitor, which is then electrically connected to a miniature coaxial cable (type SS, Lakeshore) through a 25μm gold wire. The sample is thermalised through thin 25μm gold wires silver bonded with epoxy to a thicker 0.5mm silver wire leading to the mixing chamber. The measurement system is depicted in figure 3.5.

On the original design, a sensitivity of 10^{-4}emu was reported [58] for a gradient field of 10T/m. Accordingly, we obtained in St Andrews a sensitivity of 10^{-3}emu with a gradient of < 1T/m.

In the course of our investigation it was found that the brass magnetometer had to be customised to fit our requirements and also to improve its sensitivity. The last was a necessary condition given that the brass magnetometer of Sakakibara *et al.* was designed for a 10T/m gradient and a cryostat with a cooling power of 100μW at 100mK whereas the magnet system and cryostat available in St Andrews could only provide a gradient field of < 1T/m and a cooling power of 25μW at 100mK respectively. Also, with the aim to characterise out-of-equilibrium phenomena in spin ice, we wanted to be able to sweep the magnetic field relatively fast without heating up the magnetometer.

3.2.2 Plastic magnetometer

The plastic magnetometer was designed to fit into St Andrews fridge 1 which has a 35mm bore vacuum can for a dilution refrigerator with a cooling power of 25μW at 100mK (Kelvinox25, Oxford Instruments). The main magnet of our system (Oxford Instruments) generates a magnetic field up to 17T, while a pair of superconducting modulation coils in gradient configuration can produce < 1T/m. A sketch of the magnet system and the capacitive

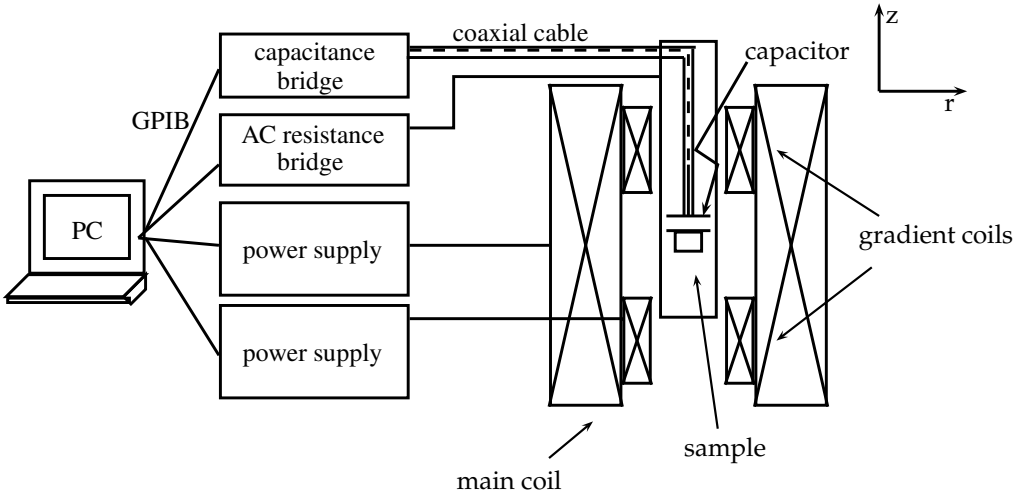

Figure 3.5: Schematic view of the magnet system and load cell. The capacitively sensed load cell is in the homogeneous magnetic field of a 17T main coil and in the centre of a set of Helmholtz coils in gradient configuration. The magnets are controlled by independent power supplies, the capacitance is measured with an automatic capacitance bridge, and the temperature is measured with an ac resistance bridge. The control and data adquisition is performed through GPIB protocol with a desktop computer and custom made software produced using the Labview (National Instruments) coding enviroment.

magnetometer is shown in figure 3.5 and is the same used for magnetisation measurements with the brass magnetometer. The magnets are controlled by independent power supplies, the capacitance is measured with an automatic capacitance bridge (AH2500, Andeen-Hagerling) operating at 1kHz, and the temperature is measured with an ac resistance bridge (SIM921, Stanford Research Instruments). The control and data adquisition is performed through GPIB protocol with a desktop computer and custom made software.

Because of the small cooling power of our cryostat and aiming for the possibility of fast sweep rates it was essential to avoid eddy current heating. In order to achieve this, and also with the purpose of thermally isolating the sample environment for precise measurements of the sample temperature, we opted for Tufset as the material for the magnetometer load cell.

In order to keep the design simple we have minimized the number of pieces by designing the magnetometer out of two assemblies, each of them containing one of the plates of the capacitor to be sensed. The first (pieces

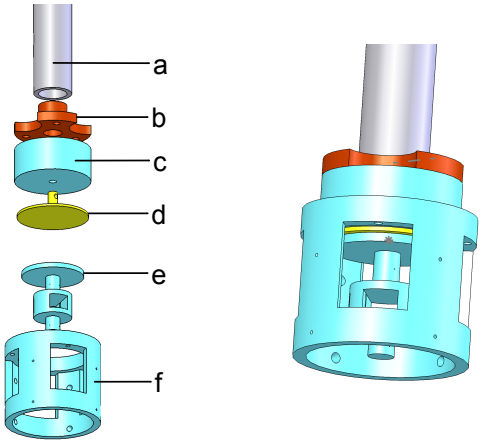

Figure 3.6: **Left**: the two assemblies that form the magnetometer: the rod assembly includes **a)** a stainless steel rod from the mixing chamber to the centre of the magnet, **b)** a oxygen free copper adapter, **c)** a threaded Tufset piece, **d)** the top plate of the capacitor made of brass. The magnetometer assembly is entirely made of Tufset and includes **e)** the sample holder plus movable capacitive plate and **f)** the body. **Right**: the assembled plastic magnetometer.

a to **d** in figure 3.6), hosts the fixed capacitance plate and includes the rod leading from the mixing chamber of the dilution refrigerator to the centre of the magnet. The second includes the moving part of the magnetometer assembly, and contains two pieces. The first one is a body (piece **f**) that screws into the rod assembly and serves as a base for the spring wires to be fixed. The second one is a sample holder (which includes the movable capacitor plate) suspended by wires (piece **e**). For this small design we inverted the geometry with respect to the brass magnetometer by placing the movable capacitor plate at the top of the sample holder as depicted in figure 3.6. In this way, the magnetometer assembly screws into the probe rod, allowing control over the initial capacitance and a much more straightforward wiring, as will be described below.

The magnetometer body consists of a 20mm outer and 18mm inner diameter cylinder machined out of a single piece of Tufset. It possesses four windows for easy access to the sample holder, and eight cone-shaped holes on the columns between the windows, that accommodate the spring wires suspending the sample holder.

Although not a critical constraint in our case, the small outer dimension

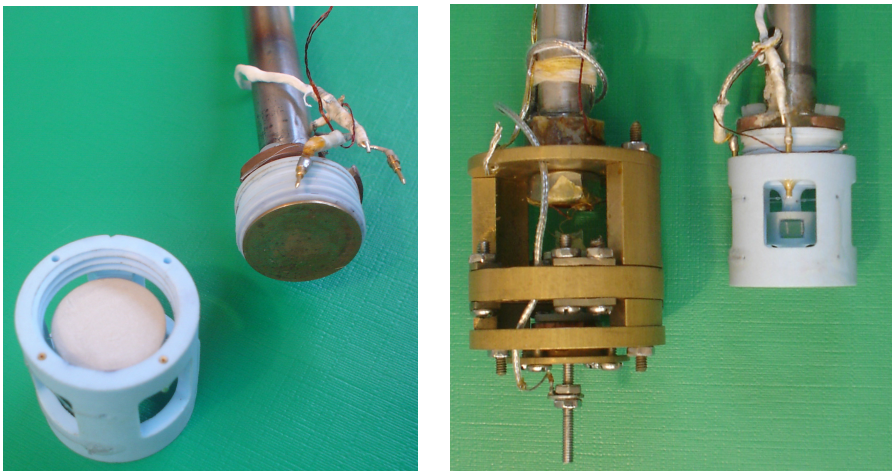

Figure 3.7: **Left**: photograph of the two assemblies that form the plastic magnetometer, the body and the rod. **Right**: photograph of the brass and plastic magnetometer side by side for comparison.

(see figure 3.7 for a comparison with the brass magnetometer) avoided the use of a centering mechanism. However, it also reduced the theoretical sensitivity with respect to the design of Sakakibara *et al.*. Modelling the deflection of a spring wire as the deflection of a beam yields a dependece of the sensitivity proportional to L^3, with L the length of the wires from the inner diameter to the sample holder at the centre [62]. In order to compensate for this loss in sensitivity we decided to change the wire material, eventually settling on 0.19mm nylon composite (fishing line) with the further advantage of reducing metallic components.

One nylon wire threading the eight holes of the magnetometer body and sample holder is used to hang the latter from the former. The holes are subsequently filled with epoxy (#1266, Stycast) to fix them in place.

The sample holder is also machined out of a single piece of Tufset. We have painted the capacitor plate on it (figure 3.8) with room temperature air-cured silver paste (4929N, Dupont) which we wired to a connector on the magnetometer body with a 25μm gold wire. The sample space on this piece is of 4mm by 3mm in the plane containing z, and 8mm depth (although the magnetometer is designed to accommodate mainly very thin samples). This space is divided into two by a sapphire plate of thickness 0.2mm that slides into a perpendicular slot and is fixed at the ends with vacuum grease (Apiezon N), leaving effectively a sample space of 4mm in depth (left of figure 3.8). We chose this material because it is non-magnetic and because

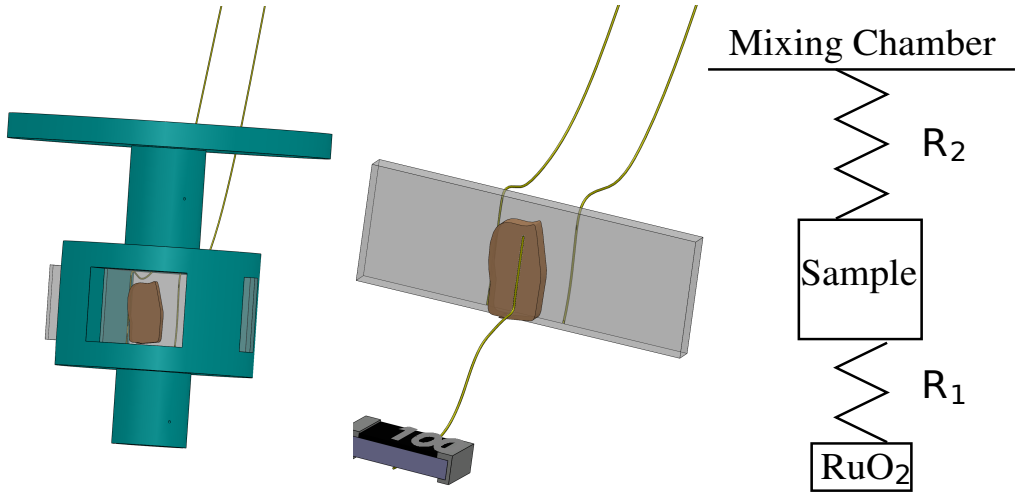

Figure 3.8: **Left**: sample holder with sapphire plate and sample. The sapphire plate is kept in place by applying vacuum grease to the sides (slots). **Centre**: detail of the sapphire plate. Gold wires at the back of it are used to thermalise the sample that is greased to the front of the plate. The sample is connected by another gold wire to a RuO_2 thermometer hanging from the magnetometer body by its contacts. **Right**: thermal resistance diagram, R_1 is much lower than R_2.

it presents a very good thermal conductivity at low temperatures compared to other insulators [61]. The sapphire acts as an orientation plane for the sample that is greased to the front of it with Apiezon grease, as shown in the centre of figure 3.8.

Two 25μm gold wires, of negligible spring constant compared to the magnetometer spring wires, coming from a connector on the magnetometer body are bonded to the the back of the orientation plate with silver paste (#6838, Dupont). Finally, a thick 0.5mm silver wire, screwed into the mixing chamber, thermally grounds the connector to the plastic body, as well as the sapphire plate and the sample. There are connectors for all wires coming from the rod to the magnetometer body, namely the thermometry manganin wires, the miniature coaxial cable (type SS, Lakeshore) to the lower plate and the thermal link to the mixing chamber. In this manner, the body assembly can be screwed into the rod assembly (see left on figure 3.7) to tune the initial capacitance at room temperature to a convenient value without twisting the wires.

As sketched in the centre of figure 3.8, in order to measure the tempera-

ture of the sample, we used as a thermometer a commercial 1kΩ RuO_2 chip (crg0805 smt, Tyco Electronics). This was attached to the sample using a 25μm gold wire and silver paste. In this way we obtained a much lower thermal resistance between the sample and the thermometer, R_1, than between the sample and the mixing chamber, R_2. The chip hangs by its leads from the magnetometer body.

The overall resolution yielded by the newly designed plastic magnetometer was better than 10^{-5}emu for an applied gradient field of < 1T/m.

3.2.3 Tests of the plastic magnetometer

The performance of the plastic magnetometer was tested by measuring the well known ruthenate $Sr_3Ru_2O_7$. $Sr_3Ru_2O_7$ is an anisotropic crystal that at low temperatures behaves like a paramagnetic Fermi liquid. For a magnetic field along the crystallographic c axis, this material undergoes a set of metamagnetic transitions where the magnetisation jumps discontinuously when a critical field is reached near $\sim$ 8T and below $\sim$ 1.2K. The value of the critical field depends on the relative angle between the c-axis of the sample and the magnetic field. This material was chosen because it is well known to our group and because it provides a valuable test for the mechanical stability of the magnetometer against the twisting of the sample platform, given that the magnetisation as a function of field lacks a feature around 12T that is manifested in the torque signal. This can be seen in figure 3.9 where the magnetic torque as a function of field is shown for a 5° tilted sample between 0.55K and 60K [63].

The experimental setup used to test the magnetometer performance is the same than the one used in the case of $Dy_2Ti_2O_7$. The single crystal of $Sr_3Ru_2O_7$ used in this experiment weighed 0.0498g and had dimensions $2 \times 2 \times 3$mm^3.

The initial condition of the experiment (T=100mK, H=0) corresponded to a capacitance of 26pF in the absence of any force. Measurements as a function of magnetic field presented features indicating metamagnetic transitions at fields H_{c1} and H_{c2} at low temperatures. Comparing the value of the critical fields for this experiment with the ones obtained by other techniques [64, 65] allowed us to infer the sample c-axis alignment, which resulted in a deviation angle of between 5 to 10 degrees from the applied field. Superimposed to the expected features associated with the metamagnetic transitions, the signal had a dominant quadratic component (even parity as a function of magnetic field).

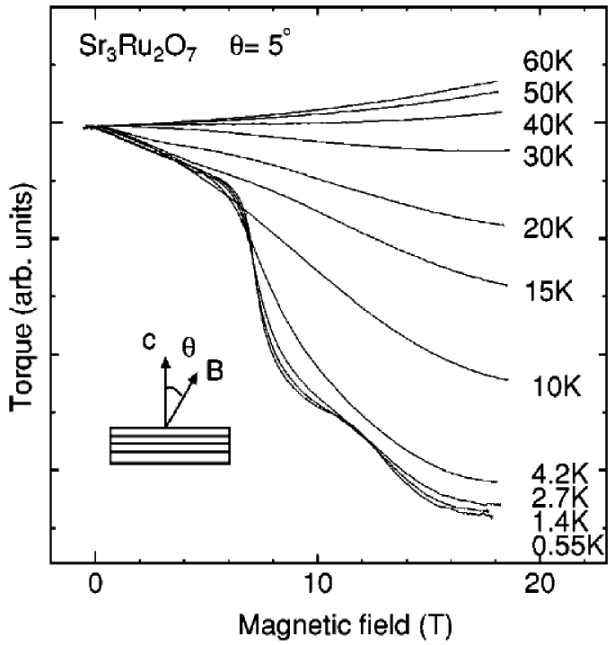

Figure 3.9: Magnetic torque data for $Sr_3Ru_2O_7$ at different temperatures between 0.55K and 60K. The magnetic field was applied in a direction tilted 5° form the c-axis. (From Omhichi *et al.* [63] Copyright©(2003) by the American Physical Society)

In metamagnetic materials such as $Sr_3Ru_2O_7$, the magnetic moment follows the applied magnetic field. We thus expect an odd-parity for $M(B)$ as the magnetic field is swept from positive to negative fields. For the torque signal we expect an even-parity trace given that:

$$\tau = \mathbf{M}(\mathbf{B}) \times \mathbf{B}; \quad \mathbf{M}(-\mathbf{B}) = -\mathbf{M}(\mathbf{B}) \quad \Rightarrow \tau(-\mathbf{B}) = \tau(\mathbf{B}) \tag{3.2}$$

Because the magnetisation comes from the odd component of the raw signal and the torque from the even, it is possible to separate both contributions to evaluate the twisting of the magnetometer platform. In figure 3.10 we show the results of doing this. The magnetisation was extracted by subtracting the data for a field sweep with a positive gradient field from that with a negative or null gradient field (divided by two). The torque contribution, in turn, was extracted from the sum of both signals (divided by two). In this way, the torque and magnetisation extraction shown in figure 3.10 are consistent with experiments performed by different techniques. The absence in the magnetisation of the torque feature at 12T is in agreement with the experiments of reference [63].

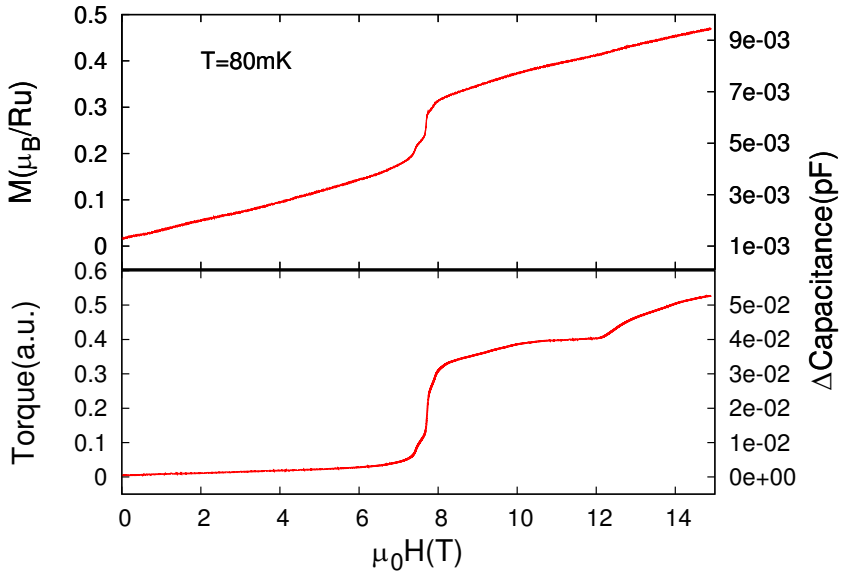

Figure 3.10: Magnetisation and torque of $Sr_3Ru_2O_7$ at 80mK. **Top**: antisymmetric part of the raw signal as regard to magnetic gradient. The magnetisation is extracted from the difference of the data with positive and with negative gradient. **Bottom**: symmetric part giving the torque. The right axis is proportional to the raw signal. Note that torque signal is almost an order of magnitude bigger that magnetisation for this starting capacitance of 26pF.

We performed a second experiment with a much lower initial capacitance of about 2.6pF. The raw data still showed a quadratic shape but with a much less pronounced behaviour (see appendix B)[4]. In any case, the subtraction and addition of the signals with a positive and negative gradient fields have proven to give the right magnetisation and torque in all cases.

For the magnetisation measurements on $Dy_2Ti_2O_7$ that will be presented on the following chapters the torque contribution to the signal was found to be neglegible on the measurements made with the plastic magnetometer. The results presented in chapter 6 and the first part of chapter 7 were obtained using the brass magnetometer. In those cases the plots shown were later postprocessed using the antisymmetrisation scheme.

We have also used the plastic magnetometer to test the idea suggested in reference [58] of alternating the gradient field to measure simultaneously

[4]It should be noted that higher initial capacitances amplify torque signals quadratically with inverse initial equilibrium distance.

magnetisation and susceptibility. This magnetometer is specially suited for these experiments given that the lack of metallic parts avoids eddy current heating. In this experiment we have used the same $Sr_3Ru_2O_7$ sample than previously.

The force per unit volume over the sample including the torque is,

$$\mathbf{F} = \mathbf{M} \cdot \nabla \mathbf{B} + \mathbf{M} \times \mathbf{B}/a \tag{3.3}$$

where a is the distance from a fixed point to the point where the force producing the torque is applied. If the gradient field is alternated on top of the gradient resulting from a stray field (for example, due to non-homogeneities in the magnet generating the constant component of the applied magnetic field $\mathbf{B_{dc}}$), then the total gradient is $\nabla \mathbf{B} = \nabla \mathbf{B}_{stray} + \nabla \mathbf{B}_{ac} \sin(\omega t)$.

We expect that any inhomogeneity in the field generated by the pair of Helmholtz coils will contribute to the signal obtained by any lock-in method when using these coils as excitation coils. This modulation together with the main field $\mathbf{B}_{dc}$ adds up to $\mathbf{B} = \mathbf{B}_{dc} + \mathbf{B}_{ac} \sin(\omega t)$. For the particular case of a paramagnet the magnetisation is proportional to the magnetic field $M = \chi B/\mu$ and then the force in the direction of the external magnetic field reads:

(for the magnetisation part)

$$F = M_{\parallel} \nabla B_{stray} + (M_{\parallel} \nabla B_{ac} + \chi_{\parallel} B_{ac} \nabla B_{stray}) \sin(\omega t) + \chi_{\parallel} B_{ac} \nabla B_{ac} \sin^2(\omega t) \tag{3.4}$$

and (for the torque part)

$$F = M_{\perp} B_{dc} + 2 M_{\perp} B_{ac} \sin(\omega t) + 2 \chi_{\perp} B_{ac}^2 \sin^2(\omega t) \tag{3.5}$$

where we used that $B_{dc} >> B_{ac}$ to replace χB_{dc} for M. We see that in equation 3.4 the first harmonic is proportional to the susceptibility and the two components of the magnetisation with different prefactors. One can see from the equations that the second harmonic gives the two susceptibilities $\chi_{\parallel}$ and $\chi_{\perp}$, one in the magnetisation signal and the other in the torque signal.

To test the a.c. method we replaced the automatic capacitance bridge for a manual capacitance bridge (1616, General Radio) to which we connected two lock-in amplifiers in series (SR830, Stanford Research Systems), in the configuration indicated schematically in figure 3.11. The output signal from one of the lock-ins was used to drive the capacitance bridge while the output signal from the other was used to drive the gradient coils.

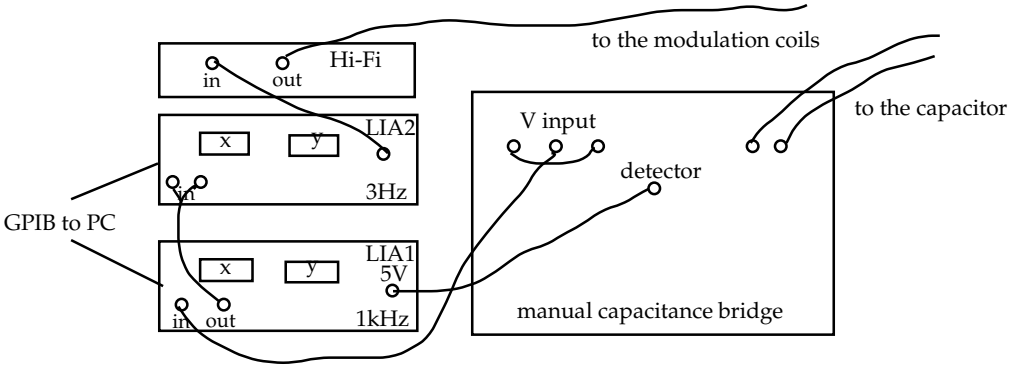

Figure 3.11: Schematic view of the susceptibility measurement configuration. The first lock-in amplifier (LIA1) operating at 1kHz is used in connection with the manual capacitance bridge. The latter is compensated at base temperature and zero field. Any imbalance (due, for example, to changes in the temperature or field) is measured as a difference ΔV by the LIA1. The raw signal is passed to the second lock-in amplifier (LIA2) which drives the gradient coils through a hi-fi amplifier at the excitation frequency (3Hz in this experiment) and locks into the susceptibility signal.

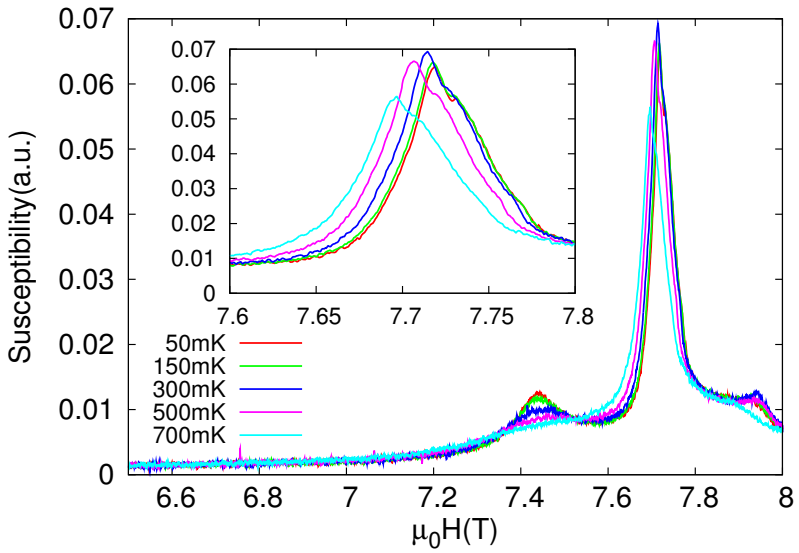

Figure 3.12: Gradient modulation susceptibility at 3Hz for different temperatures around the metamagnetic transitions. Three main peaks can be seen with a noise comparable to the one in reference [65]. **Inset:** blow up of the main peak.

Figure 3.12 shows the real part of the susceptibility measured at 3Hz around the metamagnetic transitions. This data has a noise comparable to the previously reported field modulated susceptibility data [65], where low temperature transformers, a passive element that is used to amplify the signal at low temperatures in the very well shielded enviroment of the cryostat, had been used to boost the signal. The main impediment to increasing the frequency was the increase in temperature due to eddy current heating probably coming from the material.

A potential limit to this technique is given by the resonance frequency of the moving parts of the magnetometer. We believe that the frequency range can be increased by keeping the excitation power constant, decreasing the current amplitude while increasing the frequency. Another route could be making a mechanical feedback in order to measure the feedback energy necessary to keep the capacitor plates static. In principle, this could overcome the problem of coupling into the mechanical resonance mode of the setup. This may allow measurement at much higher frequencies and broaden the sort of information obtained from the experiment.

Chapter 4

Monte Carlo simulations

Even if the Hamiltonian is known, the complex physics of $Dy_2Ti_2O_7$ at low temperatures and as a function of magnetic field makes exact analytical methods in the topic very rare. The main tools to tackle the problem come from numerics. In particular, Monte Carlo simulations have proven to accurately reproduce both equilibrium and dynamical features of experiments.

In principle, one could compute all possible states of a system for a given set of parameters and use them to generate the partition function to calculate its thermal averages over different macroscopic observables. This procedure is very computationally intensive, and hardly ever used (except for some zero temperature exact solutions of few particles). As an alternative, Monte Carlo simulations take advantage of the stochastic nature of statistical physics to numerically simulate the states of a system sampling a small portion of phase space that still gives the correct thermal averages. A complete description of the principles of Monte Carlo simulations is given in the text books of references [66, 67]; here we will only briefly discuss the basic concepts.

In a Monte Carlo simulation a system is allowed to relax to an equilibrium configuration defined by equilibrium transition probabilities between states. This is done following a convenient path where only a subset of the possible states of the system are sampled, in a procedure known as *importance sampling*. For the simulation to be realistic, it is crucial for the importance sampling to ensure ergodicity, *i.e.*, that all possible states are achievable. A second key condition is that the importance sampling must guarantee that, in equilibrium, the states are visited according to their Boltzmann weights. In equilibrium, the probability, p_μ, of being in a state μ is equal to the probability to transition to that state from any other state ν

$$p_\mu = \sum_\nu p_\nu P(\nu \to \mu) \tag{4.1}$$

where $P(\nu \to \mu)$ is the probability of transition. However, there are circunstances in which this condition does not lead unequivocally to the equilibrium distributions [66], and in general a more constrained version is required. The constrained version is known as the *detailed balance condition* and is stated as follows,

$$p_\mu P(\mu \to \nu) = p_\nu P(\nu \to \mu). \tag{4.2}$$

That is, in equilibrium, the probability to reach state μ from the state ν is equal to probability to reach state ν from μ. A Markov chain process is one whose state at each discrete time step only depends on the state at the previous time step. It is easy to show that the probabilities of a process that fulfils the detailed balance condition converge to the Boltzmann weights p_μ for long times [67].

The most common algorithm to implement Monte Carlo in general and in particular in spin ice is the Metropolis algorithm. In it, at each Monte Carlo step, the entities of the system (spins) are picked up randomly and a perturbation (flip) is proposed. If the perturbation decreases the energy of the whole system, then this virtual change is made real by accepting the move, changing the configuration of the system. This is done guided by the minimal energy principle. If the perturbation increases the energy, the virtual change is turned into a real one if and only if a random number with a uniform distribution in the real set [0,1], is bigger than the Boltzmann weight for the increase in energy ΔE, $\exp(-\Delta E/k_B T)$. In this way random thermal noise is simulated with a Boltzmann distribution. It is clear that following the Monte Carlo approach of importance sampling, a lot of computational time is saved that would be wasted otherwise in considering configurations which increase the energy beyond the limit given by statistical fluctuations.

The entities of the system in the case of spin ice are magnetic moments ('spins' in the usual jargon) that can point either towards the centre of the tetrahedra or out of them. In a computer, they can be represented by bits. One important issue of Monte Carlo is the freedom of choice of the dynamics, and it could be given by the choice of spins for which a perturbation is proposed[1]. This should be chosen accordingly for each different system, but there is no *a priori* better choice. In spin ice modelling, two main dynamics have been implemented for different purposes. On one hand, single spin flip is commonly used to accurately describe the system dynamics that reproduces most of the experiments, as thoroughly tested by Jaubert and Holdsworth [50] and discussed in section 2.4. On the other hand, loop algorithms (and

[1]It is also possible to change the dynamics by changing the probabilities for transitions as long as the detailed balance condition is preserved.

their variants, for instance, the Worm algorithm[2]) have been used in order to constrain the dynamics to spin ice configurations [23, 36]. These algorithms start from a state on the spin ice manifold and flip loops of spins without breaking the ice rule. As a particular example, an ordered ground state due to the dipolar long range interactions was found within the ice manifold at ~ 180mK using a mixture of both algorithms [23].

For the implementation of the Monte Carlo program, a cubic unit cell has been used for the spins. Each unit cell contains a base of 16 spins separated into 4 up tetrahedra. The total number of spins in the system is $L^3 \times 16$. For instance a system with $L = 2$ has 128 spins, one with $L = 3$ has 432 spins, one with $L = 4$ has 1024 spins, etc. The cubic unit cell has been chosen to facilitate the implementation of the Ewald summation technique discussed in the following.

4.1 Ewald summation

Long range interactions are defined as those whose integrals, when summed up to infinity, do not converge for a given dimensionality of the space. They present critical decay, *i.e.*, without a typical length scale and they typically adopt the analytical form $r^{-\alpha}$. With $0 < \alpha \leq 3$ they do not converge in three dimensions. The numerical implementation of the long range dipolar interactions hence requires closer attention, given that the simulation cell is finite and periodic, and a simple spherical cut-off scheme for long range interactions is known to yield misleading results (see discussion in reference [21]).

Among the different techniques to treat long range interactions, the method of Ewald summation is adequate for periodic boundary conditions [68, 69]. This method takes advantage of the linear superposition principle by adding or subtracting a convenient energy field to or from the bare one, and also takes advantages of the periodic boundary conditions by using them to calculate the contribution of the added energy field. The idea is to replicate the system in a periodic fashion in order to add a periodic energy field opposing the bare field at the particle positions (see figure 4.1) and hence force the energy to rapidly converge by introducing a length scale. While this field must be subtracted, it is periodic and can be easily calculated in Fourier space. The dipolar energy felt by one spin caused by the others after the

[2]For a dicussion see for instance, Isakov *et al.* [36]

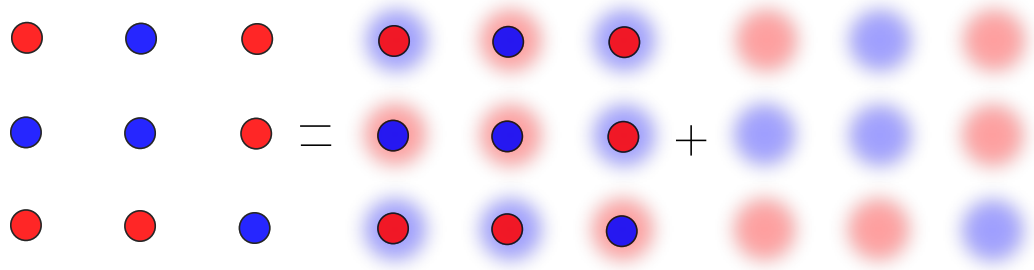

Figure 4.1: To the bare charge on the left side, a periodic energy field opposing it at the particle positions is added to force the energy to rapidly converge (first term on the right). While this field must be subtracted (note that the colours are interchanged in the second term on the right), it is periodic and can be easily calculated in Fourier space.

Ewald transformation reads [69],

$$\begin{aligned} U_{\mathbf{i}} &= \frac{D}{4\pi}\sum_{j=1}^{N}\left(\sum_{|\mathbf{n}|}(\mu_{\mathbf{i}}\cdot\mu_{\mathbf{j}})\,B(\mathbf{r_{ij}}+\mathbf{n})-(\mu_{\mathbf{i}}\cdot\mathbf{r_{ij}})(\mu_{\mathbf{j}}\cdot\mathbf{r_{ij}})C(\mathbf{r_{ij}}+\mathbf{n})\right. \\ &\quad \left.+\sum_{\mathbf{k}\neq\mathbf{0}}(\mu_{\mathbf{i}}\cdot\mathbf{k})(\mu_{\mathbf{j}}\cdot\mathbf{k})\frac{4\pi^2}{k^2}\exp(-k^2/4\kappa^2)\cos(\mathbf{k}\cdot\mathbf{r_{ij}})\right) \\ &\quad -\frac{2\kappa^3{\mu_{\mathbf{i}}}^2}{3\pi^{1/2}}+\sum_{j=1}^{N}\frac{4\pi}{3L^3}(\mu_{\mathbf{i}}\cdot\mu_{\mathbf{j}}), \end{aligned} \tag{4.3}$$

where the $\mathbf{n}$ refers to replica boxes through boundary conditions, N is the maximum number of particles taken into account, $\mathbf{r_{ij}}$ is the distance between the magnetic moments μ_i and μ_j, the constant κ is the artificial length scale introduced by the technique, L is the size of the system, and

$$B(\mathbf{r_{ij}}+\mathbf{n}) = \frac{\operatorname{erfc}(\kappa r)}{r^3}+\frac{2\kappa}{\pi^{1/2}}\frac{\exp(-\kappa^2r^2)}{r^2}, \tag{4.4}$$

$$C(\mathbf{r_{ij}}+\mathbf{n}) = 3\frac{\operatorname{erfc}(\kappa r)}{r^5}+\frac{2\kappa}{\pi^{1/2}}\left(2\kappa^2+\frac{3}{r^2}\right)\frac{\exp(-\kappa^2r^2)}{r^2}. \tag{4.5}$$

In equation 4.3, the first line corresponds to the real part, the second line to the Fourier contribution and the third line subtracts the self-interaction of the moment with its replicas through periodicity. The fictitious length-scale is a free parameter that can be chosen to obtain the fastest computational

times. Typically, $\kappa \sim 5/L$ and an spherical cut-off is imposed on the real sum $r_c = L/2$. For this choice, the error is of the order of $\exp(-\kappa^2 r_c^2)$ for the real sum and $\exp(-k_c^2/4\kappa^2)$ for the Fourier sum. For the two errors to be comparable $k_c \sim 4$.

In the case of $Dy_2Ti_2O_7$ the magnetic moments are spins on the corners of a pyrochlore lattice formed by the Dy atoms, pointing from and to the centre of each of the two tetrahedra they belong to. Because the direction of the spin is fixed, $\mu_\mathbf{i} = \mathbf{e_i} S_\mathbf{i}$ with $\mathbf{e_i}$ encoding the direction, and $S_\mathbf{i}$ the sense (in or out). Taking advantage of this fact, in a typical implementation, equation 4.3 is computed from pre-calculated values $\mathcal{J}_\mathbf{ij}$ using the equation

$$U_\mathbf{i} = S_\mathbf{i} \sum_\mathbf{j} \mathcal{J}_\mathbf{ij} S_\mathbf{j} \tag{4.6}$$

where the sum is over the neighbours j that are at a distance smaller than r_c. The numbers $\mathcal{J}_\mathbf{ij}$ are calculated from equation 4.3.

Part III

Results

A way to understand the different states of spin ice is to study the transitions between them. We can do this by using as many free control parameters as possible. In our case the experimental setup allows us to tune the temperature, the magnetic field strength, the crystal orientation respect to the magnetic field, and the sweep rate. This latter is of interest when the system goes out-of-equilibrium (*i.e.*, when the characteristic times of its dynamics become comparable to the experimental times). From all these parameters, the only one that we cannot control *in situ* on a magnetisation measurement is the crystal orientation respect to the applied magnetic field[3].

In the next chapters we present results obtained on the magnetisation process in $Dy_2Ti_2O_7$ from magnetisation and neutron scattering experiments, as well as numerical simulations. In chapter 5 we discuss the constraint that the freezing temperature posses over the experiments and the protocol adopted to perform them (zero field cooling, etc.), as well as some peculiarities of the freezing mechanism. In chapter 6 we study the existence of Dirac strings for a fixed field in the [100] direction, and we connect their existence to the possibility of a Kasteleyn transition as the magnetic field is swept in this crystallographic direction.

Also, we will find that a new phenomenon arises for low fields when the temperature is lowered below the freezing temperature. In both, the [100] and the [111] directions, very abrupt jumps of the magnetisation are triggered at a given field for magnetic sweep rates exceding a threshold. We extensively describe and give possible explanations for the occurence of these jumps in chapters 7 and 8. Finally, in chapter 9 we readdress the issue of the liquid-gas-like transition of monopoles to test the validity of the dipolar Monte Carlo model. In the same chapter we also give a closer look at the angle dependence of the magnetisation near the Kagome ice to saturation transition.

[3]This could be easily achieved using a vectorial magnet, see for instance [39, 40]

Chapter 5

Freezing temperature

Before we investigate the excitations that drive the magnetisation processes when a magnetic field is applied along different crystallographic axes, we will describe the protocol used to prepare the sample in its initial state for each experiment. Protocols are relevant given that, as we have seen, $Dy_2Ti_2O_7$ at low temperatures presents out-of-equilibrium behaviour which manifests itself as hysteresis. In order to study the low temperature behaviour of $Dy_2Ti_2O_7$, we measured, on a single crystal, field cooling (FC) curves down to 100mK and those obtained after a zero field cooling (ZFC) down to 100mK followed by increasing the field in the [100] direction to a fixed value and then increasing the temperature to 1000mK, always at 5mK/min. This experiment is similar to the one performed on polycrystalline samples by Snyder *et al.* [45] and is the standard procedure to find the onset of out-of-equilibrium in a variety of different systems. In equilibrium, the magnetisation only depends on the values of H and T and both FC and ZFC curves coincide. Differences in these curves are manifestations of departures from equilibrium. In figure 5.1 we have plotted these results and find that at a certain temperature, the FC and ZFC curves bifurcate. We can see that both curves coincide at high temperatures for the different magnetic fields applied, and that as the temperature is lowered the magnetisation curves split into two with the FC always showing a larger magnetisation than the ZFC.

The temperature at which the curves split is in the region close to $650 - 700$mK, depending on the magnetic field. The splitting of the FC and ZFC curves is very similar to the case of spin glasses except for the fact that in that case the introduction of a field decreases the splitting temperature. In $Dy_2Ti_2O_7$, for the lower fields shown in figure 5.1 (0.1T, 0.15T, 0.2T) the splitting temperature tends to increase with field, but it then decreases as the field is further increased. This fact was already pointed out by Snyder *et al.* for polycrystals. The increase of the splitting temperature for low fields is

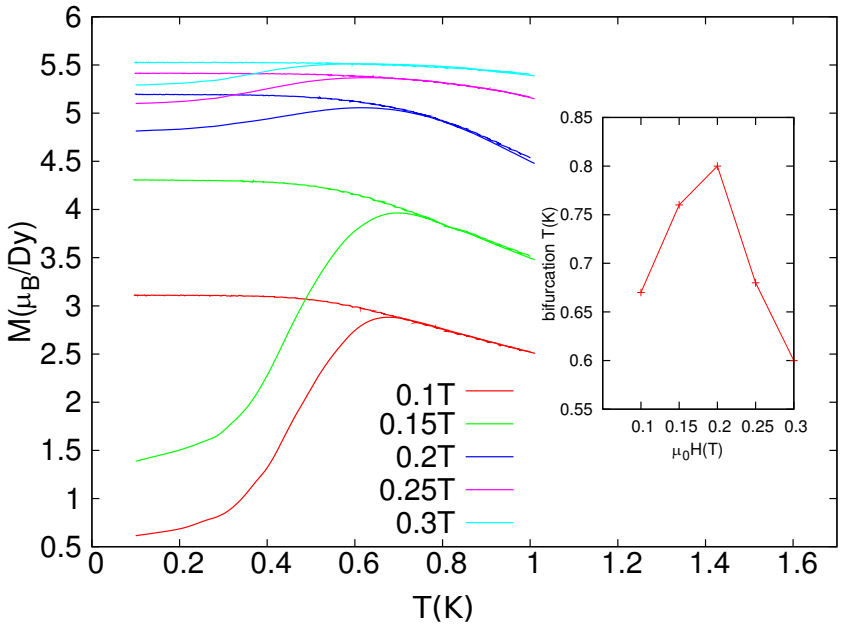

Figure 5.1: Temperature dependence of the magnetisation. First, a field cooling from 1000mK to 100mK at 5mK/min is measured. A second curve is then measured by making a zero field cooling to 100mK, then increasing the field in the [100] direction to a fixed value (0.1T, 0.15T, 0.2T, 0.25T and 0.3T) and finally the temperature to 1000mK, always at 5mK/min. **Inset**: bifurcation temperature as a function of field. Note that the bifurcation point increases with field for 0.1T, 0.15T, 0.2T and then decreases for 0.25T and 0.3T.

contrary to what is expected for a glass, in which the hysteresis has its origins on the ability of the system to explore the energy landscape. In that case, a magnetic field tilts the energy landscape making the different local minima more accesible by decreasing the effective energy barrier. This allows thermal fluctuations to explore them, quickly lowering the freezing temperature as sketched on figure 5.2. In the case of $Dy_2Ti_2O_7$ with an applied magnetic field in the [100] direction, the magnetic field favours the freezing mechanism which suggests that the freezing in this material is somewhat different from the one occurring from structural or chemical disorder in magnetic glasses.

From the results obtained in this chapter, we decided to erase the history dependence of $Dy_2Ti_2O_7$ using a protocol in which we perform a FC or ZFC from temperatures above 700mK before each experiment.

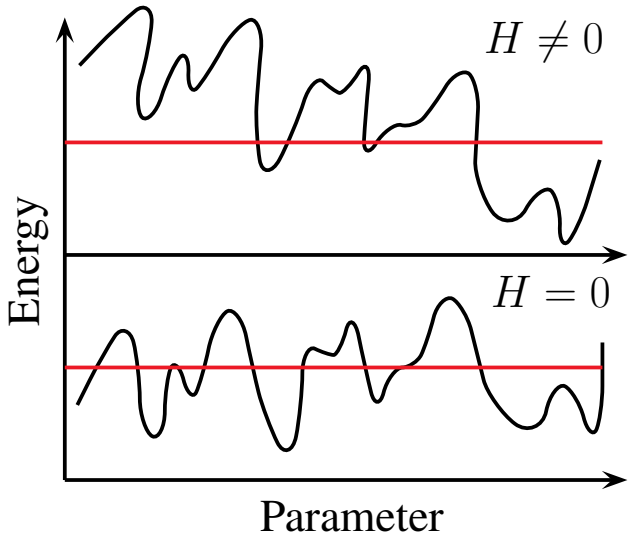

Figure 5.2: In a glass, a magnetic field can tilt the energy landscape making the different local minima more accessible by decreasing the effective energy barrier. This translates into a decrease of the freezing temperature with increasing applied magnetic field.

Chapter 6

Magnetisation process in [100]

The crystallographic direction [100] in $Dy_2Ti_2O_7$ is interesting mainly because in this direction the state with all spins maximally aligned with the external magnetic field and satisfying the crystal field constraints preserves the ice rules. In other words, the state of saturation generated by a strong magnetic field belongs to the spin ice manifold as can be seen from figure 6.1 by inspection. This fact led to the idea of entropically driven strings of spins. These strings are formed as the external magnetic field is decreased or the temperature is increased, and are the main mechanism for demagnetisation from the saturated state. As discused in section 2.3.2, strings excitations are energetically favourable over the more simple excitation formed by isolated pairs of defects (monopoles).

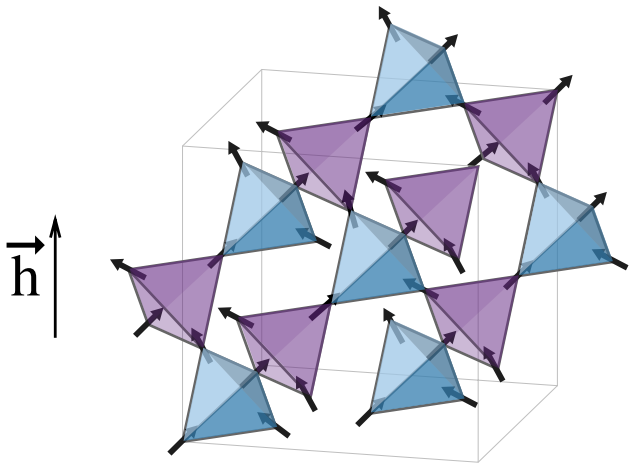

Figure 6.1: The ice rules are consistent with all up tetrahedra in an 'x' configuration.

A theoretical prediction was made by Jaubert *et al.* for the transition from the saturated state obtained by the application of a strong magnetic field, to zero magnetisation, as the magnitude of the applied field is lowered [24]. In their work, they found that for the nearest neighbour spin ice model, *i.e.*, neglecting the long range part of the dipolar interaction, and for temperatures $T << J_{eff}$, the two competing terms in the free energy, F, the entropic and the magnetic field dependence, crossed at a particular line in parameter space given by the condition $F = 0$ in the equation

$$F = \frac{2}{\sqrt{3}}\mu H - k_B T \ln 2 \tag{6.1}$$

where $m = (2/\sqrt{3})\mu$ is the Zeeman energy cost to flip a spin for a field applied along the [100] direction. As explained in section 2.3.2, for perfect spin ice, this transition line is given by the crossover from Zeeman energy dominated to entropy dominated free energy. The resulting transition was theoretically shown to be a case of a special topological transition, the 3D analogue of a topological transition known as Kasteleyn transition in the case of 2D systems [26]. Systems where Kasteleyn transitions occur have many similarities with the behaviour of standard paramagnets. These similarities stem from the fact that in both cases there are no energy scales involved aside from μH and $k_B T$, as can be checked for the case of spin ice using equation 6.1. In this sense all physical properties can only depend on boundary conditions, and in the infinite crystal case, on the dimensionless factor H/T. The scaling of all properties with this factor is the usual paramagnetic scaling explained in appendix A, and is one of the hallmarks for this kind of physics in spin ice.

In what follows we show magnetisation studies performed to unveil the mechanism of the magnetisation process in [100]. There are a few things to be aware of when programming an experiment for direct comparison with the theory. First, the most similar example of pure spin ice known to date is $Dy_2Ti_2O_7$, which is a well established example of dipolar ice; therefore, we have to understand the role that dipolar interactions play in the theory. Second, the range of temperatures at which the experiment must be undertaken is cut-off from above by $J_{eff} \sim 1.1$K, because the ice rules must be satisfied for the argument to be valid. The temperature is, in turn, cutoff from below by the experimental constraint imposed by the freezing (within the experimental measurement time) of the spin dynamics below 700mK, a fact that keeps the system out of equilibrium below this temperature (see section below). The coupling constant and the freezing temperature narrow down the range where the theory can be expected to apply.

6.1 Strings

Before going any deeper into the possibility of a Kasteleyn transition we experimentally demonstrate a necessary condition for it which is the existence of strings of spins with magnetisation opposing the almost saturating magnetic field.

One way forward if one wants to image a magnetic structure like a magnetic string is to use neutron scattering techniques. Neutrons can diffract from a magnetic structure creating a diffuse image in a detector due to a degree of coherent interference. These patterns are interpreted in reciprocal space, along with Bragg peaks from other ordered patterns (for example, the nuclei in a crystal) by comparison with theory or simulations. In particular, spin ice can be prepared to obtain high magnetic contrast by polarising all spins to form the 'x' configuration in each tetrahedron via a strong enough magnetic field in the [100] crystallographic direction (figure 6.1). As discussed in section 2.3.2 (figure 2.9), the appearence of strings will show up in a neutron diffraction pattern with a strong contrast given by the '$\pm y$' and '$\pm z$' tetrahedra obtained by flipping half of the spins on an 'x' tetrahedron as a string passes through it. At high string densities, *i.e.*, low magnetic field, strings cross among themselves and allow for '$-x$' tetrahedra where all spins in an initially polarised 'x' tetrahedron have been reversed.

The experiment to search for strings was performed in the flat cone diffractometer E2 at Helmholtz Zentrum Berlin in Germany. A specially isotopically enriched ^{162}Dy sample was grown in St Andrews to reduce the neutron absortion cross section and therefore, data collecting time as well as ensuring better thermalisation due to a lower heat input from collisions [16]. The experimental parameters, H and T suitable for the proliferation of strings were obtained from magnetisation measurements which were used to estimate their density. The requirement $T_{freezing} < T << J_{eff}$ was fulfilled with a maximum contrast just above the freezing temperature. This latter was experimentally estimated using magnetisation measurements by the loss of the H/T paramagnetic type scaling at zero field which yielded a temperature near 700mK (see figure 6.6 further below).

In the Kasteleyn picture the departure from the saturation magnetisation as the magnetic field is decreased is given solely by the appearence of strings of reversed spins. Furthermore, from magnetisation measurements one can roughly infer the density of strings. A temperature of 700mK and the magnetic field of around $B = 0.05$T were chosen to give a low density of strings as required to obtain high contrast. In all the different experiments the saturated 'x' pattern was measured and subtracted in order to reduce

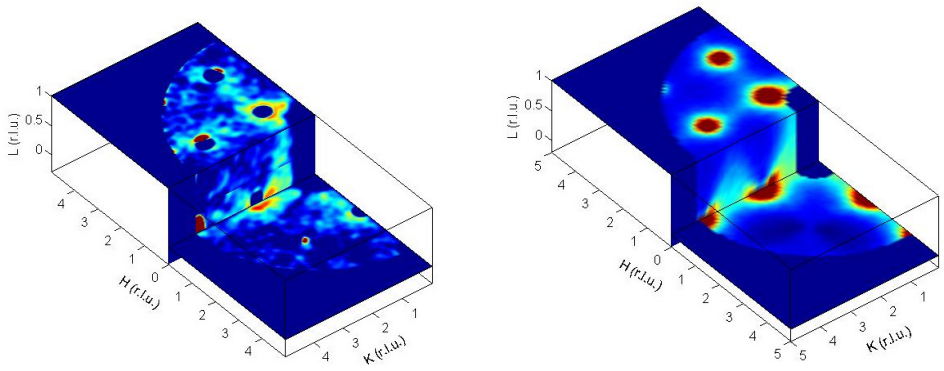

Figure 6.2: **Left**: neutron diffraction pattern at 700mK and 0.045T in the [100] crystallographic direction. **Right**: simulated neutron diffraction pattern for a random walk of strings on the pyrochlore lattice using the same experimental parameters (form factors and instrument characteristics) as in the left plot. At each step a new spin is flipped, restoring the ice rule in the previous tetrahedron by moving the defect to the next tetrahedron. For better match a bias of 53 : 47 was applied, corresponding to a small misalignment.

background contamination of the diffuse scattering.

On the left panel of figure 6.2 the experimental neutron diffraction pattern for $B = 0.045$T on [100] and $T = 700$mK is shown. Diffuse scattering is seen to emanate from [020] ($[H, K, L]$) in the form of a cone similar to a pinch point at zero field [70]. Pinch points are the fingerprints of the ice rule. The ice rule implies that the pseudospins on two given contiguous [100]-planes have to oppose in order to preserve the two in two, out rule. This means that the two [100]-planes within a tetrahedron are correlated antiferromagnetically. These correlations are inside the magnetic unit cell, and give rise to scattering peaks at [200]. In the absence of a magnetic field the scattering pattern has a six-fold symmetry given by the six possible realisations of the ice rules. When a magnetic field is applied along the [100] direction, random walks of strings form, giving rise to a four-fold symmetry in the $H - K$ plane given by the proliferation of '$\pm y$' and '$\pm z$' tetrahedra as can be seen in figure 6.2 or checked by the symmetry of on the bottom right frame of figure 6.3.

In order to check the string scenario, we have modelled and simulated a random walk of strings in a pyrochlore lattice. Using the corresponding structure factors ($f(\mathbf{k})$), this model was used to calculate the diffraction pattern that would be obtained from it in an experiment by means of the following equation:

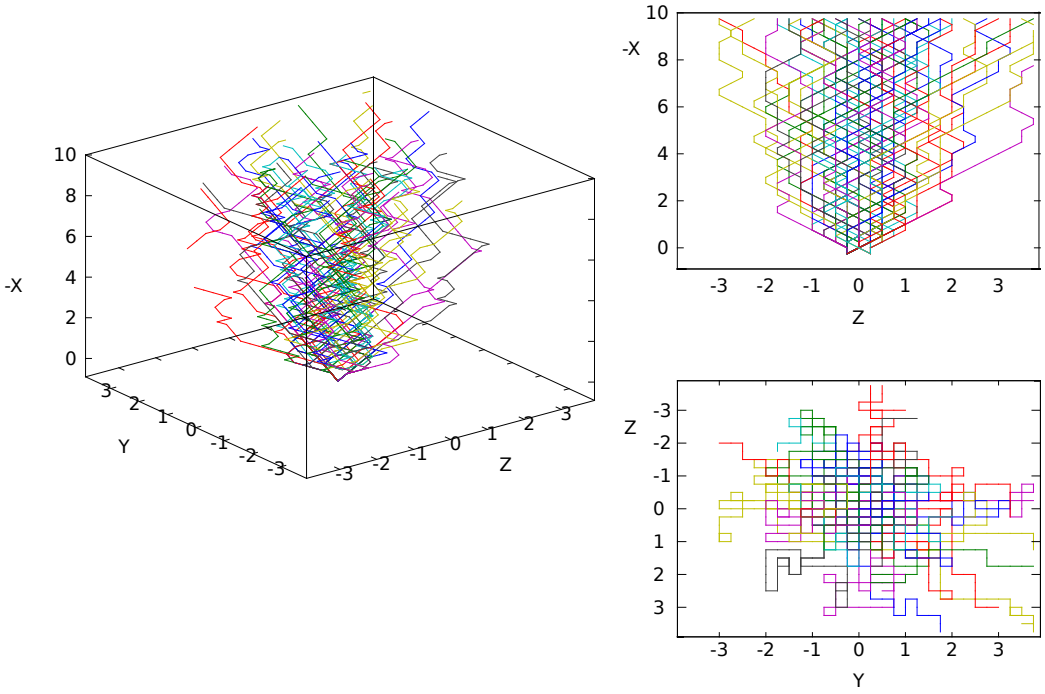

Figure 6.3: **Left**: random walk in 3D space as obtained from the simulations. The strings start from the same point and evolve randomly in the $-x$ direction as described in the text. **Right top**: $(z, -x)$ projection of the plot on the left. The diffraction pattern obtained from this picture gives the diffuse features that are compared to the experiment. **Right bottom**: (y, z) projection of the plot on the left. The cubic nature of the underlying lattice can be clearly seen. This nature will be evident in the simulated diffraction patterns (figures 6.2, 6.4). Courtesy D.J.P. Morris.

$$\frac{d\sigma}{d\Omega} \propto |f(\mathbf{k})|^2 \sum_{l,l'} \sum_{\alpha,\beta} \left(\delta_{\alpha\beta} - (k_\alpha k_\beta)/k^2\right) \epsilon_l^\alpha \epsilon_{l'}^\beta \langle \mu_l(\mathbf{k}) \mu_{l'}(-\mathbf{k}) \rangle \tag{6.2}$$

where α and β are Cartesian coordinates x, y, and z which also correspond to the cubic crystal directions a, b and c, and l and l' sweep all spins in the string[1]. The ϵ_l^α are the easy-axis directions and μ_l are pseudospins with value 1 or -1 depending whether the spins point in or out of an up tetrahedron.

The random walk takes place in the y-z plane by flipping tetrahedra from the 'x' configuration to the '$\pm y$' or the '$\pm z$' as the strings evolve in the $-x$ direction. In this simplified picture, the time of the random walk is counted in steps on the $-x$ axis and 'kinks' inverting the magnetisation on a tetrahedron

[1]Recall that the background has been substracted.

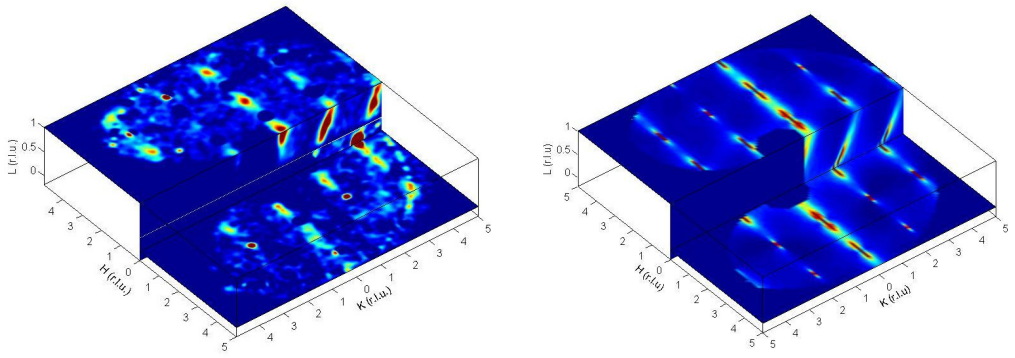

Figure 6.4: **Left**: neutron diffraction taken for the same experimental parameters as figure 6.2 but with a field misalignment. **Right**: random walks in tilted field with a bias 0.8:0.2 on the plane perpendicular to [100]. The similarity of the experimental and simulated patterns is remarkable for the diffuse traces. The cone of diffuse scattering collapses into sheets of scattering at an angle of 54°, matching the opening angle of the original cone. This sharp sheet in reciprocal space widens with decreasing field.

('x'→'$-x$') are omitted. This is shown in figure 6.3 in which different strings have been generated from the same starting point.

The result of the simulation is plotted next to the experimental results on the right side of figure 6.2. The overall agreement between the simulation and the experiment supports the existence of strings as opposed to randomly distributed defects (monopoles).

To further check the string picture we can compare an experiment in which the magnetic field is tilted about 10° from the [100] direction towards the [011], with simulation of the random walk of strings for the same tilting. This tilt favours the tetrahedron magnetisations '$+y$' and '$+z$' over their negatives according to the Boltzmann factor ratio:

$$\frac{p(+)}{p(-)} = \exp\left(\frac{2m|h|(\cos\theta_1 - \cos\theta_2)}{k_B T}\right) \tag{6.3}$$

where θ_1, θ_2 are the angles the spins in the '$+$', '$-$' configurations make with the external magnetic field. The simulation pattern with a bias of $0.8 : 0.2$ is shown on the left panel of figure 6.4. Using the weighting factors of equation 6.3 and modelling the new ensemble of Dirac strings, the tilts and widths of the scattering are well reproduced by the right panel of the same figure. The cone of diffuse scattering collapses into sheets of scattering at an angle of 54°, matching the opening angle of the original cone corresponding to the angle

that the spins make with the [100] direction (see top right panel in figure 6.3 as a guide and imagine a bias). This sharp sheet in reciprocal space widens with decreasing field.

The overall agreement of the experimental neutron diffraction patterns with the model of random walk of strings for unbiased and biased walks is a strong evidence for the existence of strings. This is the first step towards the validation of the Kasteleyn transition theory.

6.2 3D-Kasteleyn transition

The neutron experiments from the previous section presented compelling evidence in favour of magnetic string excitations driving the magnetisation. Although the theory for the string-driven Kasteleyn transition of Jaubert *et al.* was demonstrated only for the nearest neighbour model over the spin ice manifold (*i.e.*, without breaking of the ice rule), the existence of magnetic strings in the real material suggests the possible realisation of the transition in the presence of long range dipolar interactions and a non-zero density of defects.

To explore the phase diagram one can begin by substituting the magnetisation per spin for $Dy_2Ti_2O_7$ ($m = 10\mu_B/\mathrm{Dy}$) into the free energy for strings. Assuming equilibrium, we can use equation 6.1 to express the temperature of the transition as a function of magnetic field, to obtain the red straight line with the positive slope shown in figure 6.5. The large slope in the T-H plane implies that the transition should be seen at low fields. In the same figure we have represented with horizontal lines two temperature scales: an estimation for the freezing temperature (blue) and the effective nearest neighbour interaction J_{eff} (green) which bounds the theoretical temperature region available to find the transition, as discussed on section 2.3.2. We have also included in the background a colour plor for the density of monopoles per tetrahedron for the same parameters as calculated from Monte Carlo simulations of 1024 spins ($L = 4$) interacting via a long range Hamiltonian (equation 2.2) using single spin flip dynamics. This plot illustrates clearly where in parameter space and to which extent the ice rules are obeyed by the system. The dark regions represent absence of monopoles, and the lighter implies their existence in very low densities of up to about 10%. Below $\sim$ 700mK the system freezes and the monopole density decreases, suggesting that these two facts are correlated.

At non-zero temperatures, the temperature scale is set by the ice rule energy scale. At a temperature comparable to J there will be a finite density of monopoles, corresponding to the appearance of finite size strings ending

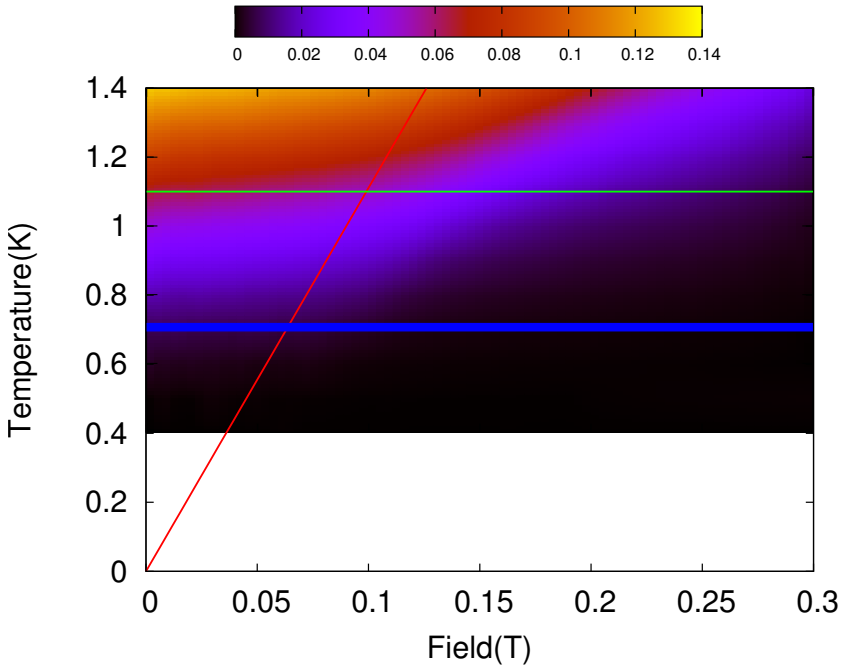

Figure 6.5: Red line: Kasteleyn transition line. Blue line: Freezing line (below this line the density is out of equilibrium). Green line: $T = J_{eff} =$ 1.1K, above this temperature the density of monopoles increases rapidly. The background map reflects the monopole density per tetrahedron as calculated from Monte Carlo simulations of 1024 spins ($L = 4$) interacting via the long range Hamiltonian 2.2. The most likely region to check for the Kasteleyn transition prediction is above but near the freezing line where the monopoles are strongly suppressed and the system is still in equilibrium.

in monopoles. In principle a finite length of strings obtained by a non-zero density of monopoles could lead to a rounding of the Kasteleyn transition by the introduction of J as an energy scale. This will severely affect the H/T 'paramagnetic' scaling that is obtained for a scale free magnetic system in the defect-free 3D Kasteleyn theory for $Dy_2Ti_2O_7$.

The fingerprint of a Kasteleyn transition in $Dy_2Ti_2O_7$ is an infinite susceptibility at the transition point when it is reached from the string side (low field, high temperature: the area to the left of the red line in figure 6.5). Recall that saturation for [100] is given by a unique state that belongs to the spin ice manifold and that has all tetrahedra in the 'x' configuration. This state acts as a vacuum for the entropically generated magnetic strings responsible for the decrease in magnetisation. As the ratio H/T is lowered, at the tran-

sition point the entropic term overruns the magnetic one in the free energy and strings can form. At this point, strings see no resistance to piercing the material with any string density (apart from the mutual entropic repulsion), and their creation manifests as an infinite susceptibility. Although it is quite possible that the presence of monopolar excitations rounds the transition through fluctuations, the remains of the infinite susceptibility may still be visible in the magnetisation curve which should have a positive curvature for increasing magnetic field in the string dominated region.

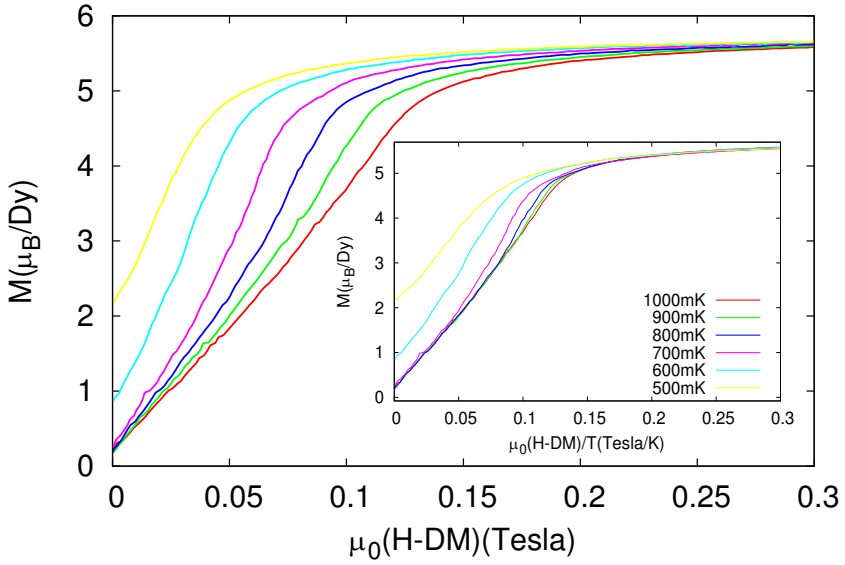

Figure 6.6: Magnetisation vs. internal magnetic field for [100] field sweeps at different temperatures between $500 - 1000$mK and at a sweep rate of 0.05T/min. The field is swept down from a saturated state at 1.5T. The remanent magnetisation at zero field in this experiment means that below a temperature of $\sim$ 700mK the system falls out of equilibrium. The transition to saturation is rounded as expected, but the residual signature of a Kasteleyn transition can be see in the convex curvature of the magnetisation. **Inset**: internal magnetic field/temperature scaling as a function of field for the curves in the main frame. The curves do not collapse over the full range of fields; the collapse is seen only for low fields. As the temperature is lowered, the system departs from equilibrium and the collapse fails even at low fields. The demagnetisation factor of the sample was $D = 0.116$.

As can be seen in figure 6.6, this is indeed the case in the experiment. The magnetisation as a function of internal magnetic field ($H_i = H - DM$) in the [100] direction is shown for different temperatures between 1000mK and

500mK. In this case the demagnetisation factor of the sample was $D = 0.116$. These curves were measured with the field swept down from saturation at 1.5T. As expected, the saturation process is not as abrupt as it is in the pure spin ice theory (without defects) and presents a significative rounding. However, the magnetisation on the string side (low fields) is clearly convex. We have checked by means of Monte Carlo simulations that the rounding was not an artifact due to misalignment. Within 5° tilting towards [111] and [110] directions, the convexity remains and no rounding appears (not shown). The convex curvature is a strong indication of Kasteleyn physics playing a major role. Below 700mK the curves start deviating from the common trend as a result of the spin system freezing out, as will be discussed later in chapter 7.4.

Strictly, the magnetisation as a function of [100] field for a defect-free spin ice system should have Kasteleyn characteristics. It will also scale as H/T, because of the lack of an intrinsic energy scale. Although everything in the last figure points towards underlying Kasteleyn physics, the same magnetisation data from the main frame plotted in the inset of figure 6.6 as a function of H_i/T do not collapse over the full range of fields, but do so only for low fields. The departure from a single curve on this plot (which would be the pure spin ice case) is systematic, with a better collapse for the curves measured at higher temperatures.

In the same way that for a paramagnet all physical properties depend on H/T, in the theory of the Kasteleyn transition for spin ice, the ice rules are satisfied everywhere which implies that there is no intrinsic energy scale present. Therefore, the behaviour of the system can only depend on the reduced variable H_i/T. The departure from the H_i/T behaviour can only be compatible with the existence of magnetic strings demonstrated by neutron diffraction experiments if the strings posses finite length and hence an energy scale associated with it.

In figure 6.7 magnetisation loops are shown for different temperatures ranging from 1000mK to 500mK. The main findings of this figure are related to the departure from equilibrium at a higher temperature than the one expected. We can distinguish the presence of hysteresis from around 800mK downwards. This value is slightly larger than the 700mK used for annealing the sample using the protocol discussed in chapter 5. This field dependence of the freezing temperature could already be seen in figure 5.1 in which the bifurcation point for FC and ZFC curves increased with increasing fields of values up to about 0.2T. This behaviour agrees with the one measured in polycrystalline samples by Snyder *et al.* [45].

As can be seen in the figure, at 800mK the difference between up and

down sweeps is concentrated close to the transition. This probably indicates that the hysteresis can be interpreted in terms of different velocities for the magnetisation and demagnetisation processes at the Kasteleyn transition point, where magnetic strings enter the material.

The hysteresis shown in figure 6.7 is very peculiar in the sense that the upward sweeps do not present the positive curvature seen in the case of figure 6.6. Further experiments should be carried out in order to understand this behaviour.

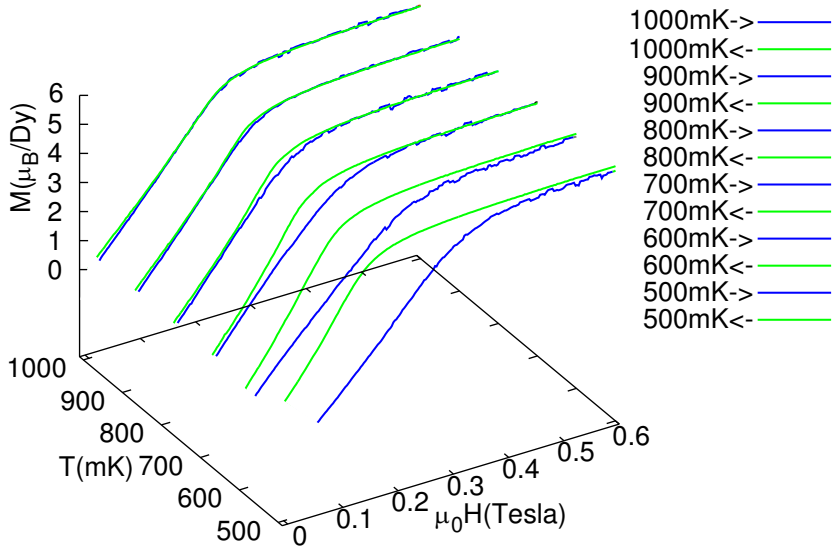

Figure 6.7: Magnetisation loops obtained by reflecting around zero the magnetisation corresponding to negative fields of magnetic field sweeps between 1.5T and −1.5T. In blue up sweeps, in green down sweeps.

We can now compare the outcome of the experiments with those of Monte Carlo simulations of the dipolar model for 1024 spins ($L = 4$). For this we used single spin dynamics and found, that the long range dipolar interaction still preserves the convexity for the M vs. H with respect to the nearest neighbour model, in agreement with the Kasteleyn prediction. This can be seen in red on the right panel of figure 6.8 which shows up and down sweeps for temperatures 1000mK, 900mK, 800mK and 700mK. Both up and down curves retrace the same path in contrast to the case of the experimental data. This is not surprising since no effort was made to match the Monte Carlo time with the measurement time. In the same plot we have added the experimental data for down sweeps in blue (left panel). For low fields, a relatively good agreement is obtained, but it becomes worse as the field is

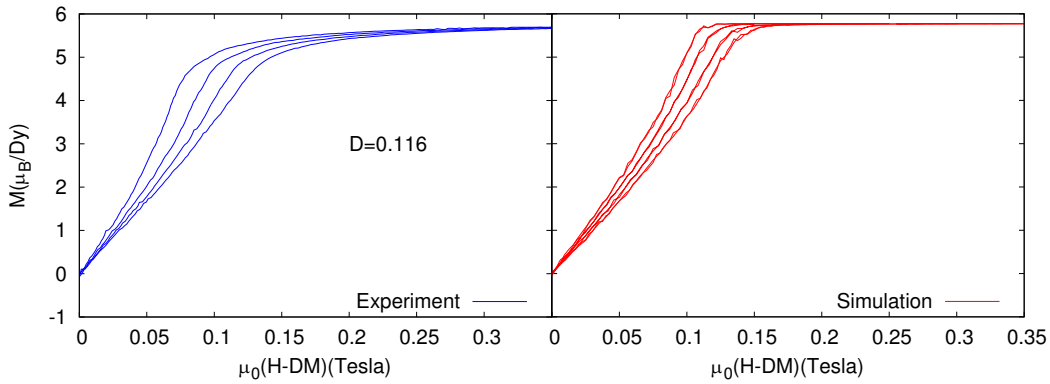

Figure 6.8: **Left**: experimental magnetisation vs. internal magnetic field for 1000mK, 900mK, 800mK and 700mK decreasing the magnetic field (same data than in figure 6.6). The demagnetisation factor of the sample is $D = 0.116$. **Right**: Monte Carlo simulation of the dipolar model for single spin flip dynamics. Magnetisation loop after a zero field cooling for the same temperatures.

increased or the temperature is lowered. In particular, the simulated data present a rather abrupt transient to saturation while the experimental data have a very rounded one. This could be a consequence of a finite size effect on the simulation or the use of an inadequate Hamiltonian that does not capture all the physics. Finite size effects could affect the mean value of string length which in turn affects the monopole density and with it the freezing temperature. On the other hand, a magnetic field in [100] tends to suppress defects (monopoles) by driving them to the edges of the sample. We have performed finite size effect studies but failed to detect a tendency towards the experimental result mainly because of computational constraints. We would strongly benefit from the deeper insight that could be achieved by the use of more powerful computers to simulate larger systems. Also it would be possible to change the dynamics from single spin flip to a Worm algorithm that has a larger acceptance rate as shown in reference [71] by Jaubert who succeeded at simulating much larger systems up to $L = 125$ in the nearest neighbour model. It remains to see whether this algorithm should still be more convenient than single spin flip in the case of long range dipolar interactions.

Chapter 7

Low field magnetisation in $Dy_2Ti_2O_7$

The most salient features of the behaviour of $Dy_2Ti_2O_7$ under the influence of a magnetic field applied in the [111] crystallographic direction were introduced in chapter 2.3.3. In this section we will focus on the magnetisation process that takes the system from the spin ice state at zero field to the Kagome ice state which is, as mentioned before, characterised by a magnetisation plateau (the 0T to 0.7T region in figure 7.1).

In the absence of a bias field, when the temperature is lowered from a temperature above the freezing point down to base temperature (zero field cooling), the sample adopts a spin ice configuration with an extremely low density of quenched disorder [25], and with zero magnetisation. This configuration is formed by an equal number of tetrahedra of each of the six spin ice configurations '$\pm x$', '$\pm y$' and '$\pm z$' discussed in section 2.1. After this zero field cooling, the field is increased from zero and the system evolves towards the Kagome plateau at a magnetisation value of $3.33\mu_B$/Dy. In this plateau the spins form a state that belongs to a subset of the spin ice manifold which is characterised by the apical spins being polarised in the field direction. In this state, the tetrahedra are in any of the three '$+x$', '$+y$' and '$+z$' positive configurations. This submanifold still allows for three different possibilities per tetrahedron which in turn gives, for a macroscopic number of tetrahedra, a macroscopic entropy. The process that we will address in this chapter has to do with the polarisation of the zero field random apical spins obtained after a zero field cooling (half of them pointing along the [111] direction and the other half along the $[\bar{1}\bar{1}\bar{1}]$) towards the in-field collinear apical configurations where all of them point along the [111] direction.

There are only two ways of changing magnetisation in spin ice with a field

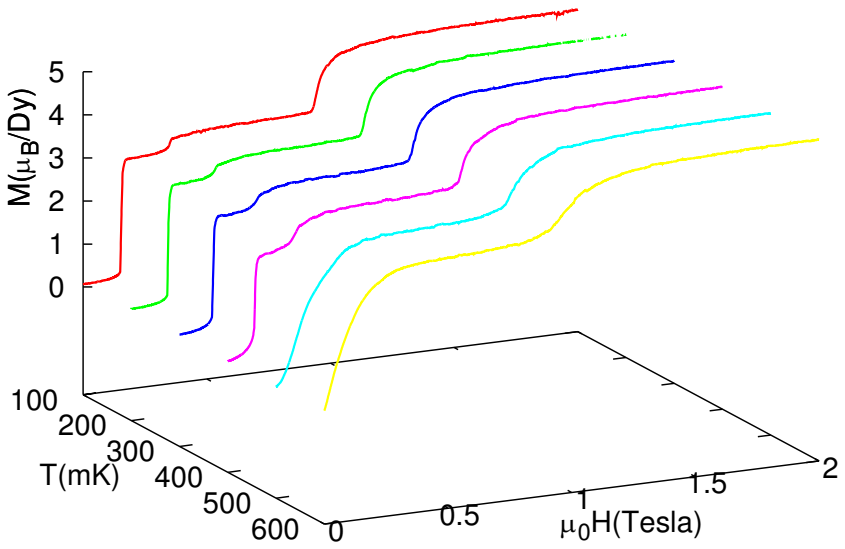

Figure 7.1: Magnetisation trace of $Dy_2Ti_2O_7$ under the influence of an applied magnetic field in the crystallographic [111] direction for different temperatures. This plot is comparable to the one measured by Sakakibara *et al.* which is reproduced in the figure 2.11 of section 2.3.3.

applied along the [111] direction. Either the ice rules are broken at intermediate stages creating finite size strings ending in monopoles (this includes isolated monopolar defects which always appear in pairs), or collective spin flips forming strings spanning the whole length of the sample in the field direction. The latter, is similar to the case of the strings found with the field applied along the [100] direction in the case of pure spin ice. Because the process that takes the system from zero magnetisation to the Kagome plateau implies a change in magnetisation, both cases should be analysed. The latter scenario of infinite strings was proposed by Isakov *et al.* in reference [36]. In terms of energy, long strings are preferred over isolated pairs of monopolar defects, because their energy is lower for the same number of spin flips (see section 2.3.2). From the entropic side, the entropy associated with strings and monopolar defects is very similar in [111], given that the planes perpendicular to the [111] direction are very much uncorrelated due to the fact that defects on these Kagome planes can travel within them at zero energy cost (for the nearest neighbour case).

Either way, the transformation of '$-$' tetrahedra into '$+$' by flipping apical spins and fixing the ice rules to move the system from zero magnetisation to the Kagome plateaux deserves special attention. The study of the dynamics of this situation was the body of the publication "Unconventional

magnetisation processes and thermal runaway in spin ice $Dy_2Ti_2O_7$" [72], and will be presented and expanded below.

7.1 Temperature dependence

7.1.1 High temperature: a cooperative paramagnet

Within the ice manifold spin ice is a geometrically frustrated system that shares some features in common with paramagnets even at temperatures below its effective coupling constant. This is a common characteristic of frustrated systems that is usually called cooperative paramagnetism [73]. The scale free behaviour typical for a cooperative paramagnet in the temperature regime below J_{eff} has its origin in the extensive degeneracy of the ground state: in our case, the spin ice manifold. As we have seen in the last chap-

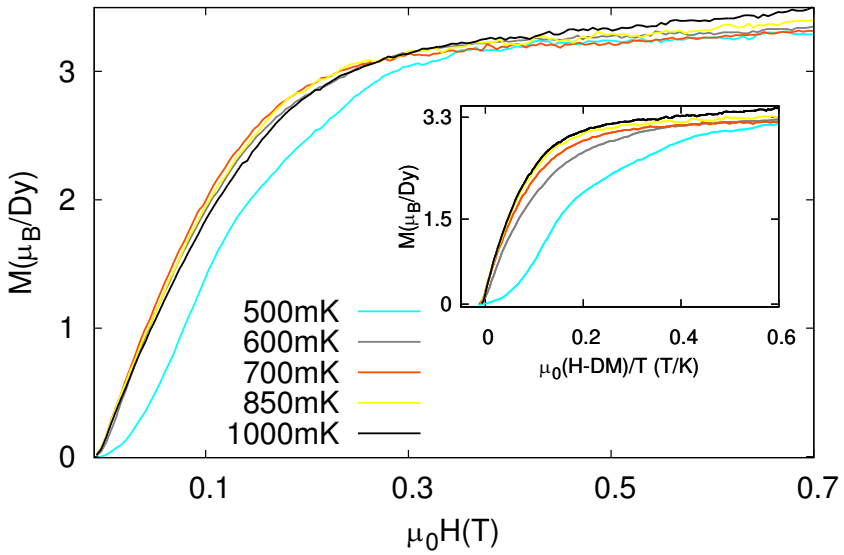

Figure 7.2: Low field magnetisation for [111] magnetic field sweeps between zero field and the Kagome plateau, at different temperatures between 500 − 1000mK, and at a sweep rate of 0.1T/min. The curves below 700mK were prepared by a zero field cooling to 700mK. Below this temperature the curves fall out of equilibrium. **Inset**: H_i/T cooperative paramagnetic scaling (see text). The out-of-equilibrium behaviour is illustrated by the low field side of the curves departing from scaling.

ter, the degeneracy implies that no pure spin ice configuration is subject to an energy scale, which in turn means that any excitation that perturbs the

ground state has an associated energy that has to be considered strong in the sense that it will dominate the dynamical processes that will characterise the material's behaviour. The absence of an energy scale for the ground state is reflected in the H/T scaling in any measurable quantity of the system.

The magnetisation for low fields between 0 and 0.7T along the [111] direction is shown in figure 7.2 for different temperatures between 500mK and 1000mK. These curves were measured at a sweep rate of 0.1T/min and after a zero field cooling when suitable. A recurrent feature from the case of the magnetic field in the [100] direction (figure 6.6) is the observation of freezing as identified by the departure from a paramagnetic scaling (see inset) at very low fields. Again, for temperatures above the freezing temperature ($\sim$ 700mK) the magnetisation rises linearly from zero as expected for a cooperative paramagnet [73], and it rounds towards the Kagome plateau in a narrow set of field values.

The inset of figure 7.2 explicitly presents the H/T scaling using, instead of the nominal field H, the internal field $H_i = H - DM$ where $D = 0.115$ is the calculated demagnetising factor based on the geometry of the sample [74]. In this, the collapse is evident for temperatures above the freezing temperature at small fields.

7.1.2 Low temperature: magnetisation jumps

As the temperature is decreased below the freezing temperature, the magnetisation curves depart from the H/T scaling. This is shown in the inset of figure 7.3 where the magnetisation is plotted as a function of internal field. Indeed, at the lower fields the curves at 700mK, 600mK and 500mK, increase their magnetisation at a much slower pace than for a cooperative paramagnet. The departure from the H/T scaling marks the onset of out-of-equilibrium dynamics and the start of a dramatic change of the behaviour of the system. Near zero field the magnetisation increases almost linearly with a tiny slope that depends on the temperature, with higher slope for higher temperature. After that, a temperature dependent field is reached where the magnetisation jumps abruptly to a value close to that at 700mK. These jumps are very sudden and can hardly be resolved by our instrument recording 1 point every $\sim$ 2s.

After the jump, the magnetisation remains almost constant, evolving into a quasi-plateau of magnetisation value ranging from 2.4 μ_B/Dy at 400mK to 2.8 μ_B/Dy at 100mK. Note that the jumps are huge, given that the change in magnetisation accounts for about half of the magnetisation at saturation for this field direction. As the field is increased, the transition from the quasi-plateau to the Kagome plateau happens in either a smooth fashion

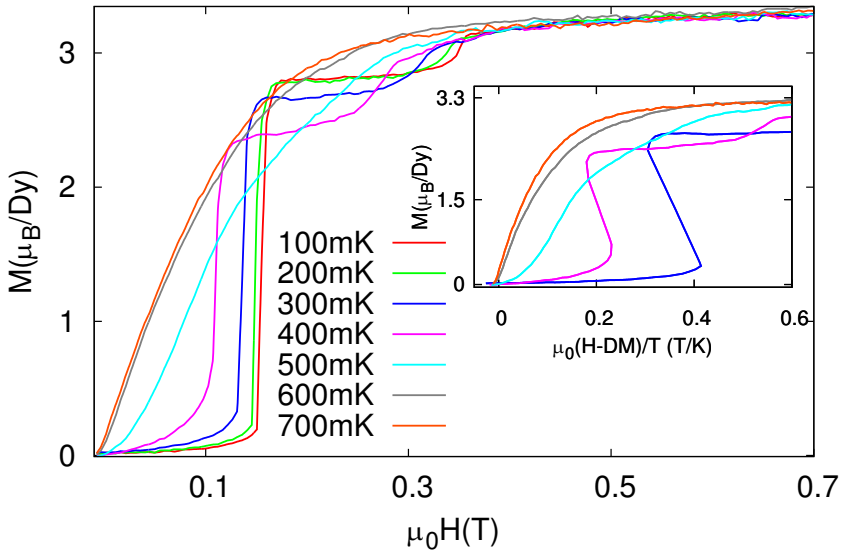

Figure 7.3: Low field magnetisation for [111] field sweeps between zero field and the Kagome plateau for different temperatures ranging between $100 - 700$mK. The curves were prepared by a zero field cooling from above 700mK, and they were measured at a sweep rate of 0.1T/min. The curves fall clearly out-of-equilibrium with a sub-Curie susceptibility. For the lowest temperatures, the magnetisation jumps abruptly. **Inset**: H_i/T cooperative paramagnetic scaling. The jumps for the lower temperatures have negative slope as a function of the internal field indicating that they are triggered events.

or through a second jump depending on the temperature. As a general feature, both the intermediate plateaux and the jumps become sharper with decreasing temperature.

In the inset of figure 7.3 one can notice that the jumps present a negative slope in the H_i/T scaling, indicating that they are triggered events. In a triggered event there is an ignition threshold (an energy barrier) above which the material starts a process that cannot be stopped even if the triggering parameter at a later moment is below that threshold. In the case of the magnetisation jump, triggering occurs at an internal field H_j which, in a simple picture[1], can be associated with a given energy μH_j. Even though the internal field during and after the jump becomes lower than the triggering field (manifested by a negative slope) the magnetisation continues increasing

[1]Strictly, the free energy should be counted, but because of the clear out-of-equilibrium dynamics given by the loss of ergodicity, the concept of entropy lacks any sense.

after the jump.

The triggering in $Dy_2Ti_2O_7$ is similar to the ignition of a piece of paper where an initial fire has to be set in order to start the burning process. Once the first fire is set, the fire front propagates fast, giving no time to the paper to diffuse the heat away. Furthermore, the heat coming from the fire feedbacks positively into the burning process by increasing the probability of thermally overcome energy barriers due to the high temperature. This process is called deflagration and in the case of magnetism was observed and characterised in a series of publications on specially prepared molecular magnets [75, 76, 77, 78, 79] for which a theory was proposed by Garanin and Chudnovsky [80]. The details of the deflagration process in $Dy_2Ti_2O_7$ will be analysed in chapter 8.

Now, we want to expand on the experimental quantities extracted from the jumps of figure 7.2. These jumps are characterised by the field at which they occur and by the magnetisation value attained on the plateau immediately after the jump, two values that are strictly reproduced over runs. The jump field is temperature dependent, happening at increasingly higher fields for lower temperatures: (400mK, 0.1T), (300mK, 0.13T), (200mK, 0.15T) and (100mK, 0.16T). The tendency is to a unique real triggering field at zero temperature, and presumably the different triggering fields are only due to the thermal contribution to the threshold energy for different temperatures.

Focusing in the microscopic origin of the jumps, we can assume that the flip of the apical spins precedes that of the basal spins given that the spin projection over the applied field is three times larger for the first, and knowing that at the Kagome plateau all apical spins are collinear with the magnetic field direction. At 100mK and at the threshold field for that temperature, the change in magnetic energy due to an apical spin flip from down to up is $2\mu H_j \sim 2.2$K. Taking into account the fact that the energy to break the ice rule by flipping an apical spin from a spin ice state is $4J_{eff} = 4.4$K (2.2K per tetrahedron) in the nearest neighbour model, we see that the energy scale for the jump is consistent with a deconfined defect picture where breaking the rules in only one tetrahedron is allowed at a cost of $2J_{eff} = 2.2$K. As an activated process, this can only happen either at the boundaries or at defects in the bulk.

This is not the first appearance of this energy scale. In reference [50] the relaxation time measured in the susceptibility experiments discussed in section 2.4 was fitted with an exponential decay (Ahrrenius law) indicative of an activated process. The best fit in the region $2.5 - 5$K was obtained for the characteristic energy $2J_{eff} = 2.2$K, corresponding to the energy of single topological defects. In that case, it was argued that this energy scale came from the fractionalization of defects giving half of the energy to each

of the topological defects created by a single spin flip and by the strong screening due to the proliferation of monopoles. In this case, however, we believe that screening cannot be invoked given that the monopole density at these temperatures is extremely low.

7.2 Field sweep rate dependence

Although the magnetisation jumps were absent from the magnetisation studies by Sakakibara *et al.* [29] (figure 2.11) using a Faraday force magnetometer, they were observed in indirect measurements of the magnetisation by means of neutron diffraction experiments on $Dy_2Ti_2O_7$ by Fennell *et al.* [14, 81]. We could solve this apparent inconsistency by measuring the dependence of the out-of-equilibrium dynamics of $Dy_2Ti_2O_7$ on the magnetic field sweep rate.

In figure 7.4 the magnetisation as a function of internal magnetic field at 200mK is shown for magnetic field sweep rates spanning a factor of about thirty. The curves in this figure can clearly be separated into two groups: those showing one or more jumps, with sweep rates v greater or equal to 0.025T/min, and those showing a continuous growth of the magnetisation, from 0.01T/min to 0.003T/min. This difference already reconciles the previous experiments from Fennell *et al.* and Sakakibara *et al.*, assigning the discrepancy to the magnetic field sweep rate dependence of the magnetisation. Presumably the latter experiment was performed at a much slower field sweep rate than the former, and then missed the jumps. Also in the same figure, the orange curve is formed by the points reached after a series of field coolings at different fields.

In the group of curves that show a magnetisation jump, the height remains unaltered with a magnetisation value around $2.8\mu_B$/Dy. In the other group, the slope of the continuous curve seems to be quite similar. The main difference within this last group comes from the behaviour of the curves at low fields (below 0.15T). Given that at a slower sweep rate the system has more time to relax, the curves increase linearly from zero field, with a larger slope for the slower sweep rates. Eventually, all slow curves tend to merge into a single curve at field above ~ 0.15T. This common curve has a similar slope the field coolings curve (orange curve).

Another feature that should be noted in the same figure is the abrupt change in slope close to 0.25T joining the slow sweep rate curve below this field with the Kagome plateau above it. This behaviour will be found to be more marked later in the discussion of the results obtained with the plastic magnetometer.

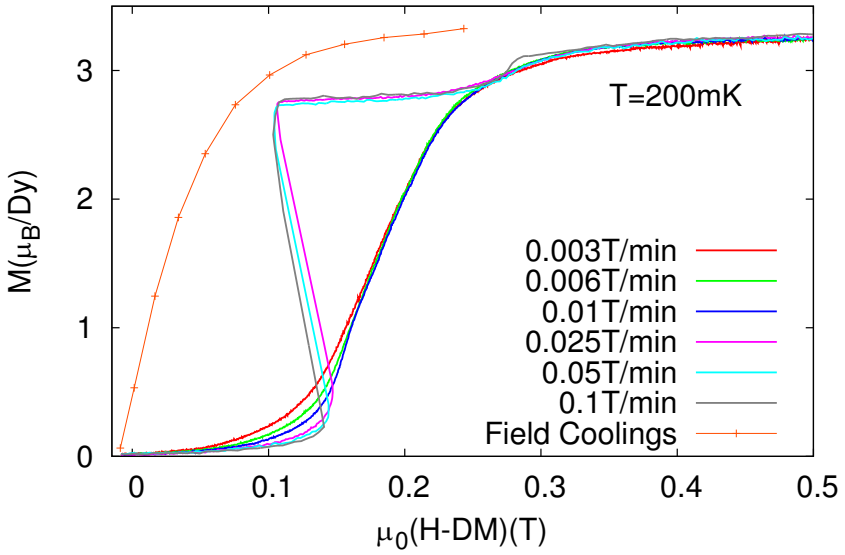

Figure 7.4: Low field [111]-magnetisation for different field sweep rates at a temperature of 200mK and after a zero field cooling. The orange curve is formed by the initial points reached after a series of field coolings run at different fields. This curve have a very similar slope to the slow sweep rate curves.

We can introduce now a theory for the mechanism of the low field magnetisation based on the dynamics of the monopolar excitations introduced in section 2.3.4. If the magnetisation proceeds via field-driven motion of these excitations, the maximal rate at which the system can respond should be given by $(dM/dt)_{\max} \sim \rho_m \, 10\mu_B/\text{ms}$, where ρ_m denotes the density of thermally activated unbound monopoles that is independent of field for very weak fields and strongly suppressed at low temperature; and the use of the single spin flip time scale of 1ms is based on the work described in section 2.4. In this case, even the slowest experimental sweep rate in figure 7.4 requires processes where M changes much faster than $(dM/dt)_{\max}$ to maintain equilibrium for $T \ll T_{\text{equil}}$. As a result, the system enters a strongly out-of-equilibrium regime where the magnetisation remains very small despite the presence of the applied magnetic field.

In this picture, even though the density of monopoles is low as in the case of the field in [100], the effect of a single monopole can be large because it can flip a string of spins increasing the magnetisation $O(L)$ as is swept to the sample surface.

In most materials, the Zeeman energy released by the magnetic moments

when they flip to align with the applied field, is quickly transported away by the vibrational degrees of freedom. In spin ice, presumably, there will be a range of parameters where the area density available for filament creation would be low enough for their Zeeman energy release to be absorbed by the rest of the system: we identified this with the slow-sweep regime. As we will argue below, in this picture, the fast-sweep regime corresponds to the situation where this is no longer the case, and a thermal runaway is induced. The increased rate at which Zeeman energy is dumped into the system as the field sweep rate increases overtaxes the ability of the lattice (the phonons) to equilibrate the local lattice temperature with that of the rest of the bath. As a result, the sample heats up locally, leading to the creation of more (and more easily unbound) monopoles. These in turn dump more energy as they move in the field direction and thermal runaway is 'ignited' above a critical sweep rate.

In this scenario, the slow sweep rate curve would be given by an energy landscape that is tilted by the applied magnetic field, similar to what happens to glasses (see figure 5.2). In order to agree with experiment, this landscape should be very shallow given that it is only seen at the lowest temperatures. This mechanism may also be helped by a localised heating produced by the spin flips which, though not being enough for triggering a cascade may influence the turning of spins in the close vicinity.

7.3 Field-cooled jumps

The field at which the jumps occur for the faster sweep rates can be tuned by preparing the sample into different initial states of magnetisation as can be seen in figure 7.5. In it, the magnetisation is plotted as a function of internal magnetic field for a sweep rate of 0.1T/min measured after cooling the sample to 200mK in different applied magnetic fields (orange). In the same plot slow curves (0.01T/min) at 200mK (blue) and 700mK (black) are also included. Note that the magnetisation value for each field cooled curve, similarly to the quasi-plateau case, hardly changes until the curve crosses the slow rate trace. Shortly after, it suddenly jumps up to its equilibrium value at a magnetisation very similar to the one corresponding to the field of the jump of the magnetisation trace for a temperature of 700mK.

The existence of a gap would naïvely imply that the triggering field should be at a fixed value of the magnetic field when correcting the curves by the demagnetisation effect. That is why it is very important to emphasize the fact that the triggering field for the field cooled curves is not unique, as can be seen from the plot. This means that the cause of the triggering

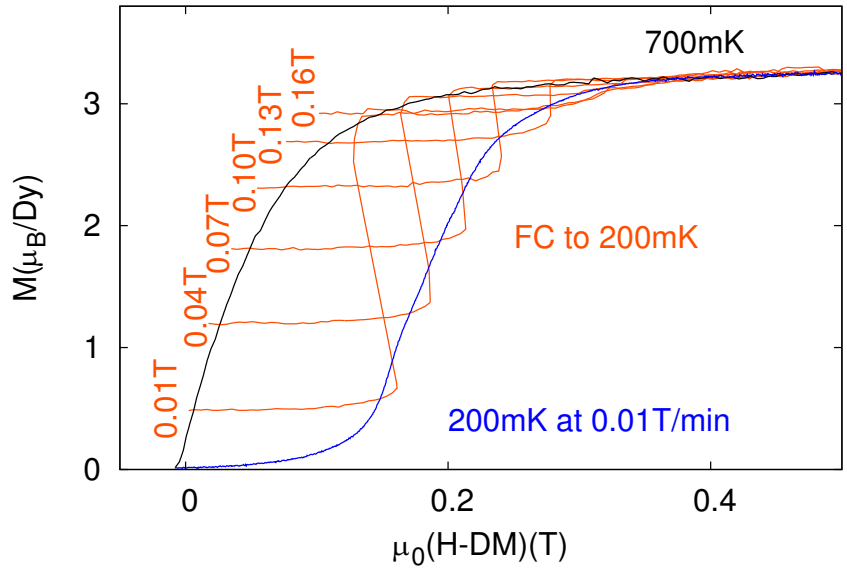

Figure 7.5: Magnetisation vs. internal magnetic field at 0.1T/min and 200mK for different starting field cooled states (as indicated in each curve), together with the slow curve (at 0.01T/min) and the 700mK curve. The field-cooled jumps are roughly contained within these two limiting curves.

jumps is strongly dependent on the field and/or the magnetisation, this last comprising the spin configurations.

A last thing to point out is the fact that the triggering field starting from different field cooled curves is surprisingly parallel to the curve made by joining the starting points of the field cooled curves.

7.4 Low temperature magnetisation in [100]

We now turn to the study of the low temperature magnetisation process for fields along [100] where we will find, similarly to the case of [111], sweep rate dependent magnetisation jumps.

As we depicted in figure 6.5, below the freezing temperature there is a departure from Kasteleyn physics due to the loss of equilibrium. In figure 7.6 the magnetisation vs. magnetic field is plotted for different temperatures at a sweep rate of 0.05T/min. We see again that, as the temperature is lowered, the initial slope of the curves decreases, and finally plateaus for the lower temperatures. This behaviour is in clear contrast with Kasteleyn and with the simple cooperative paramagnet, where H/T scaling is also expected. As

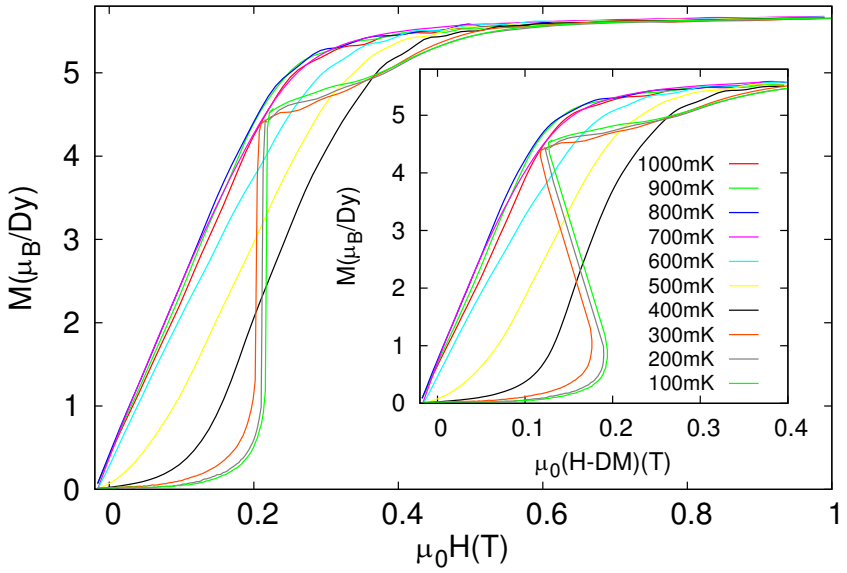

Figure 7.6: Magnetisation vs. magnetic field for different temperatures below 700mK. The curves were measured at 0.05T/min. **Inset**: same curves plotted as a function of internal magnetic field.

the field is increased we find that, for the curves below 300mK, the initial plateau evolves into a very sharp magnetisation jump in a similar way as for the field along the [111] direction discussed in the previous sections. This jump occurs in over approximately 2s and spans a magnetisation change of about $3.5\mu_B \mathrm{Dy}^{-1}$. In the inset of the figure the same magnetisation data is plotted as a function of internal magnetic field. In this case, the sudden jumps of the magnetisation acquire a negative slope, a clear indication of out-of-equilibrium physics. As in the case of [111], these jumps are triggered events that, once started, cannot be stopped until the spins responsible for the mechanism either flip or equilibrate.

Another important feature of the plots in figure 7.6 is the fact that, as seen for $H//[111]$, the jumps stop at a value different from saturation and very similar to the one corresponding to the 700mK curve at that field. However, instead of following a quasi-plateau from this point, the curves evolve almost linearly towards saturation with well defined slopes lower than the equilibrium one. This last behaviour is different from that obtained for the [111] case. The field at which the magnetisation jumps occur varies with temperature but for the lower temperature it can be seen to be $H_j = 0.19\mathrm{T}$. This field implies a Zeeman energy per spin of $(2/\sqrt{3})\mu H_j = 1.46\mathrm{K}$ which is $\sim 2/3$ of the energy needed to create a single defect in the nearest neighbour

model ($2J_{eff}$).

The resemblance with the case of the field in the [111] direction goes even further if we consider the magnetisation as a function of internal magnetic field at different field sweep rates and at base temperature. The results are depicted in figure 7.7 for sweep rates of 0.01, 0.02, 0.04 and 0.05T/min. The magnetisation only jumps for the fastest rate. The curves without a jump present a consistent, although very slow, approach to equilibrium. This can be seen as a displacement of them to the left, manifested by an earlier take-off from the initial plateau.

We have also plotted the magnetisation curves for different field coolings (orange) in the inset of figure 7.7. These curves were measured at base temperature and sweeping the magnetic field at 0.1T/min. In the same plot we have included for comparison several other experimental curves such as the one obtained by joining the initial magnetisation points for different field coolings (black), and the magnetisation curve at 700mK as well as a slow field sweep rate curve at base temperature extracted from the main figure (both in gray).

The field cooling curves at base temperature are very similar to the corresponding zero field cooling curves in the sense that they all start out of a plateau and then jump up to a value very similar to the value of the 700mK curve at H_j. After the jump they also increase their magnetisation in a linear way towards saturation. We should point out the fact that there is no unique H_j for the demagnetisation corrected curves, which seems to suggest that there is no unique triggering field, and that the triggering energy depends on the state of the system just as in the [111] case. Another feature present in the inset is the marked parallelism between the FC curve and the curve formed by the different H_j. Again, these curves have a very similar slope to the one of the slow sweep rate curve for magnetisation values over $2\mu_B$/Dy.

The out-of-equilibrium behaviour described in figure 7.6 and figure 7.7 is not reproduced by Monte Carlo simulations. The nearest neighbour model equilibrates at all temperatures for reasonable simulation times. The simulation of the Hamiltonian 2.2 departs from equilibrium at about the same experimental temperature, although it fails to reproduce the exact jump features. In Monte Carlo simulations an initial plateau appears and then a series of jumps lead the way to saturation. As will be extensively discussed in the next section, we will have to incorporate an additional ingredient to the Hamiltonian in order to explain these jumps. This ingredient will be shown to be the spin-phonon coupling.

The last thing we would like to address about the low temperature mag-

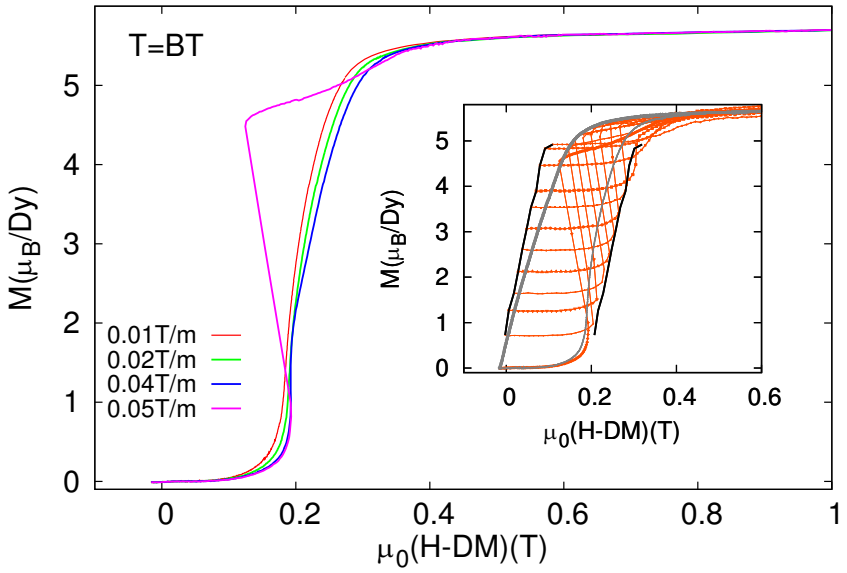

Figure 7.7: Magnetisation vs. internal magnetic field for the different sweep rates (0.01, 0.02, 0.04 and 0.05T/min). At sweep rates above 0.04T/min the magnetisation presents a jump. **Inset**: magnetisation vs. internal magnetic field for different field coolings (orange) at a sweep rate of 0.1T/min. In the same plot we have included for comparison the magnetisation curve at 700mK, and one field sweep rate curve obtained after cooling the sample from 700mK to base temperature (both in gray). Also we have joined the initial magnetisation points for different field coolings (black), and copied the same curve moved by 0.21T to the right. Note the similarity of this curve with the one formed by the points where the magnetisation jumps.

netisation in [100] is the process itself. In other words, does it take place at a slower rate but with the same principle as in equilibrium? We have demonstrated that in equilibrium string excitations are the precursor of magnetisation changes. As explained in section 2.3.2 strings are energetically favourable over isolated monopoles because they preserve most of the ice rules for the same increase in magnetisation. The existence of strings is an experimental demonstration of the fact that this energetic term prevails over isolated monopoles to drive the changes in magnetisation which are entropically more favourable [2]. As the temperature is lowered, the entropic term becomes less important and the energy and Zeeman terms dominate. This means that

[2]Strings in [100] define some order which diminishes their entropy with respect to isolated monopoles. This is the same order that allows us to distinguish them in the neutron diffraction pattern.

strings are even more favourable than at higher temperatures. Without an entropic term, strings should cross the system aligning the magnetisation with the field direction for the tiniest applied field. Instead, the magnetisation after a zero field cooling starts with an increasingly longer plateau as the temperature is decreased. This can be interpreted as the appearence of a gap to excitations that does not allow the magnetisation to evolve until the threshold for excitation creation is reached with the magnetic field. If that were the case this gap should be a function of the magnetisation (or more generally, the state) of the system, because different field coolings show the jump preceding the initial plateau appearing at different internal magnetic field values. However, there should be a relation in the fact that all initial plateaus are the same length, independently of their starting point.

7.5 Plateau after jump in [111]

Coming back to the [111] case, a difference with that of [100] is the appearance of the quasi-plateau after the jump. This plateau has an extraordinary stability and a specific value of magnetisation that is reproducible. We discuss a possible configuration that fulfils these criteria at the lowest temperature for the quasi-plateau, approaching the value $M = 2.8\mu_B/\mathrm{Dy}$ for the zero field cooling curve.

Given that the apical spins are more likely to flip before the basal spins as the field is increased from a ZFC situation, a guess for the microscopic nature of the jumps could be that all the apical spins that point down after a zero field cooling (those spins on the tetrahedra that are left in the '$-$' configuration) flip together at once when the triggering field is reached, hence giving the jump. In this scenario, the energy gap supplied by the ice rules assigns a low probability to flipping the apical spins pointing down at zero field. As the field is increased, the magnetic energy becomes larger until the threshold is reached and it becomes enough to overrun the ice rules. Of course, this picture neglects entropic terms, a sensible approximation given that the system is strongly out-of-equilibrium.

After a field cooling, the starting magnetisation is finite. Therefore, if we assume that the state obtained after a field cooling belongs to the spin ice manifold, the number of apical spins pointing up would be in excess from the number of apical spins pointing down. This difference can be calculate from the following considerations: the initial magnetisation after a field cooling, M_0, corresponds to

$$M_0 = 3.33X\frac{\mu_B}{\mathrm{D}y} \tag{7.1}$$

or more explicitly

$$M_0 = \left[3.33X + 3.33\left(\frac{1-X}{2}\right) - 3.33\left(\frac{1-X}{2}\right)\right]\frac{\mu_B}{\mathrm{D}y} \tag{7.2}$$

where $3.33\mu_B/\mathrm{Dy}$ is the magnetisation per spin of a tetrahedron fulfilling the ice rule with its apical spin pointing up; and X is the fraction of apical spins pointing up in excess from those pointing down. When there are no apical spins pointing down the magnetisation equals the Kagome magnetisation $3.33\mu_B/\mathrm{Dy}$. The final magnetisation after all apical spins pointing down flip can be calculated replacing the value $3.33\mu_B/\mathrm{Dy}$ in the last term of equation 7.2 for the value $1.66\mu_B/\mathrm{Dy}$ corresponding to the case of a tetrahedra with the apical spin pointing up in a configuration that breaks the ice rules.

$$M = \left[\frac{1}{4}M_0 + 2.5\right]\frac{\mu_B}{\mathrm{D}y} \tag{7.3}$$

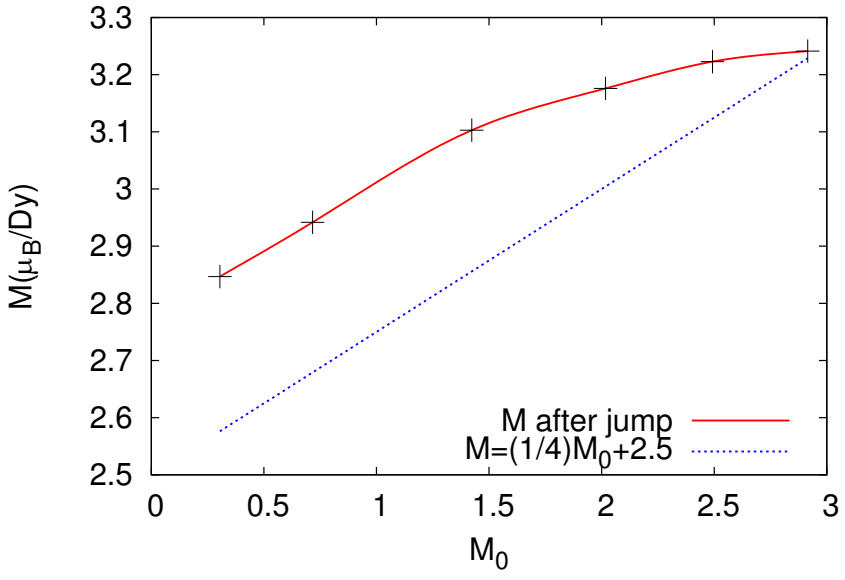

Figure 7.8: Final magnetisation as a function of initial magnetisation. In red the magnetisation after the jump is plotted for different field coolings (see figure 7.5). In blue we plotted equation 7.3.

In figure 7.8 the final magnetisation as function of the initial magnetisation (equation 7.3) is plotted along with the experimental data showing the final magnetisation value after the jump for the different field coolings shown in figure 7.5. The state at zero temperature obtained by flipping all apical

spins that were pointing against the field direction in a zero field cooled state has a magnetisation value of $M = 2.5\mu_B$/Dy. This value is close but still different from the plateau value at base temperature ($M = 2.8\mu_B$/Dy).

In terms of monopoles, the state after the jump would have a high density of monopoles. At first glance it seems that this state is unstable to the flipping of a second spin (one of the two basal spins with negative projection onto the field direction), which would effectively annihilate two monopoles, leaving a one-chain longer string behind. This would both fix the ice rule in up to two tetrahedra and gain magnetic energy. However, this mechanism can only be invoked for those pairs of connected tetrahedra that started with their apical spins pointing down before the jump. Presumably, where the basal spins do flip, their contribution to the magnetisation sums up with the $M = 2.5\mu_B$/Dy from the apical spin flipped to give the value of magnetisation of the quasi-plateau. The fact that the remaining tetrahedra cannot use this mechanism to decrease their free energy could be the reason for the stabilisation of the quasi-plateau. In this case, in order to continue increasing the magnetisation, monopoles have to be separated at the energy cost of their mutual Coulomb interaction. In particular, this argument for the stability of the quasi-plateau is in agreement with the jumps seen in the [100] direction where there is no plateau after the jump since there is no distinction between apical and basal spins for the field in that direction.

Chapter 8

Deflagration

The experiments described in the previous chapters were performed with the brass magnetometer presented in section 3.2.1. In this chapter we report on the experiments performed with the plastic magnetometer, showing the consequent improvement in signal quality and providing new information on the magnetisation processes, due to the ability to measure the sample temperature using the experimental configuration detailed in section 3.2.2.

In figure 8.1 we present an experiment in which the field is swept at 0.05T/min. Initially, the saturated magnetisation state was prepared by cooling the sample in a field of -3T. The different temperatures at the mixing chamber ranged between 100mK and 600mK. In the plot, we only show the low field part of the curves, in particular the interval $[-0.5, 0.5]$T, placing special emphasis on the positive values of magnetic field. In this case the constant magnetisation regions at the ends correspond to the Kagome plateaus at $-3.33\mu_B$/Dy and $3.33\mu_B$/Dy. On the right panel of the figure the sample temperature, T_s, measured by the sample thermometer is shown for positive values of magnetic field.

For the magnetisation, we found a marked asymmetry between negative and positive fields which indicates out-of-equilibrium behaviour in the form of hysteresis, given that the response of the system is different when the field increases or decreases. Even the 600mK curve is asymmetric due to freezing. This asymmetry is absent from the higher temperature field sweeps shown in the inset of the left frame of figure 8.1 for the same range of magnetic fields.

As can be seen in the main frame, as the field is swept from negative to positive values, the magnetisation starts undulating on top of a steady increase. The undulation increases in amplitude for lower temperatures, and eventually a temperature is reached at which the slope of the magnetisation is so steep that a magnetisation jump is triggered.

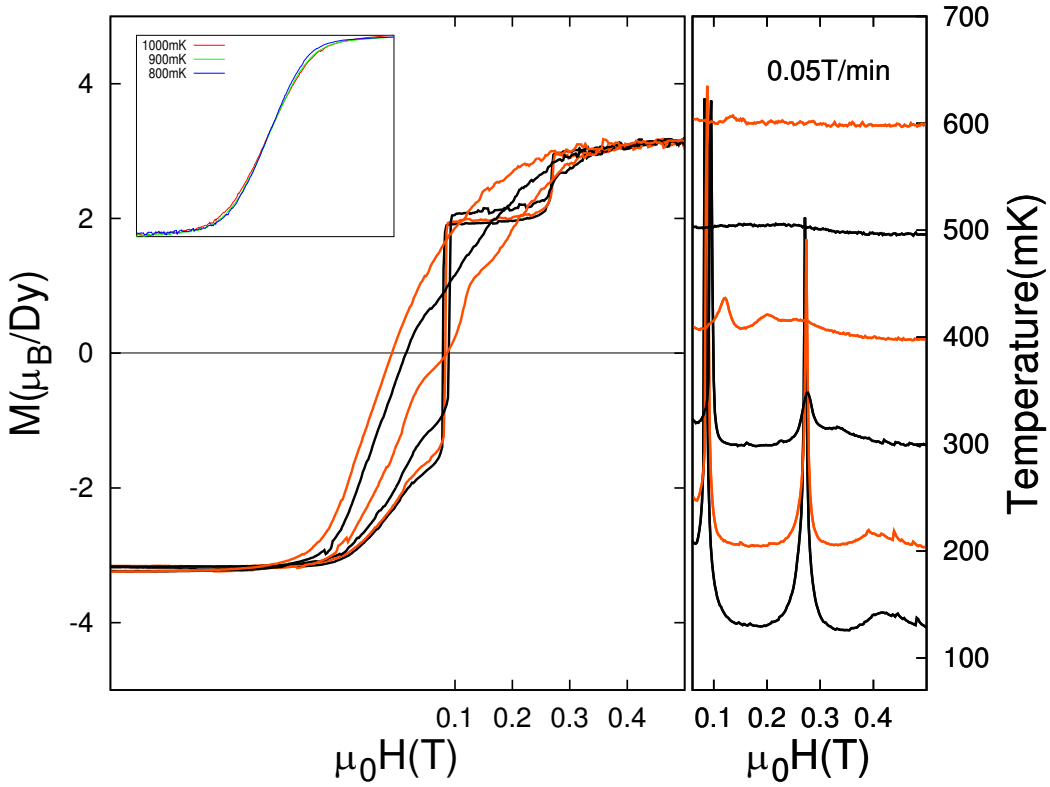

Figure 8.1: **Left**: magnetisation vs. magnetic field for different mixing chamber temperatures ranging from 100mK to 600mK at a field sweep rate of 0.05T/min. The initial state was prepared by field cooling to the saturated magnetisation state at -3T. Note the marked asymmetry between negative and positive fields. This is an indication that the system is out of equilibrium. For the lowest temperatures the magnetisation presents abrupt jumps. **Inset**: M vs. H for the same field range as the main frame but for higher temperatures. Above 600mK the magnetisation is symmetric in field. **Right**: temperature of the sample, T_s, as a function of magnetic field for the same parameters as for the magnetisation curve on the left. All magnetisation traces map onto traces on the sample temperature. For instance, the jumps correspond to a steep increase in the sample temperature, and the undulations in M correspond to bumps in T_s. Note that regardless of the initial temperature, the first set of temperature jumps reach the same temperature just above 620mK and the second around 500mK.

The temperature trace measured with the thermometer in contact with the sample is shown in the right panel and contains important information that complements the magnetisation data on the left. The most impressive feature of this plot is the temperature increase at the same fields where the magnetisation jumps, H_j. The first temperature rise corresponding to the first magnetisation jump has its maximum just above 600mK for a very different set of initial temperatures (100mK, 200mK and 300mK). This is similar to what happens on the magnetisation side where the jumps stop at approximately the magnetisation value found at H_j for the field sweep at 600mK.

One possible explanation for the maximum in temperature reached at the jumps could be that above about 600mK, the system can efficiently release to the phonon bath the excess energy stored in its out-of-equilibrium configuration, which can equilibrate the system by coupling spins at different positions. If this were the case, then the configuration after the jump would be a frozen image of an equilibrium one obtained by heating the system up to $\sim$ 650mK and quickly lowering the temperature down to that of the mixing chamber. Therefore, measuring this configuration by means of neutron diffraction would be a stringent test for the scenario of all apical spins flipping at the magnetisation jump proposed in section 7.5.

For the field sweeps at temperatures where the magnetisation does not jump, there is still an increase in temperature which corresponds to the undulations in the magnetisation curves. This can be seen at 400mK. The second set of jumps mimics the first, with the only difference that the maximum temperature decreases $\sim$ 120mK from the first jump, for all different starting temperatures.

The correspondence between events in magnetisation and in sample temperature is due to the particular dynamics of $Dy_2Ti_2O_7$ at low temperatures and is only seen due to our experimental arrangement. In our set-up the sample is weakly thermally coupled to the magnetometer head, but strongly thermally coupled to the mixing chamber, giving a very efficient path for the heat generated by the sample to diffuse towards it (see section 3.2.2).

The diffusion of heat from the sample to the mixing chamber can be modelled using the continuity equation: $\frac{d}{dt}(F)+\nabla\cdot\mathbf{J}=0$, with $F=U-MH$, the internal energy and $\mathbf{J}$ the flux of heat. This equation can be transformed into

$$C\frac{dT}{dt} = -G(T-T_{mch}) + \frac{d\mathbf{M}}{dt}\cdot\mathbf{H} + \mathbf{M}\cdot\frac{d\mathbf{H}}{dt}, \tag{8.1}$$

by using the chain rule on the left hand side to convert the internal energy

into the specific heat of the sample by means of $C = \frac{dU}{dT}$[1]. On the right hand side of the equation, T is the temperature of the sample, T_{mch} is the temperature of the mixing chamber, and G is a positive heat conduction constant. The last term represents an increase in energy due to the change in magnetic field. This term is the one responsible for the magnetic jumps, because it stores Zeeman energy whenever the magnetisation departs from equilibrium. In equilibrium, the magnetisation is able to adapt to changes in parameters (H and T) continuously, decreasing the free energy by dumping the excess energy to the phonon bath. Out of equilibrium, the magnetisation can lag behind the equilibrium value, storing energy in a configuration that, when changed towards equilibrium, can release a considerable amount of energy. Equation 8.1 is specific to the out-of-equilibrium case where the entropic contributions can be neglected given the small value of $\frac{dU}{dT}$. This means that the energy balance has to be computed one to one, in the sense that a given spin pointing opposite to the field direction gives away its excess energy by creating a phonon which carries it away, instead of using the energy to equilibrate the spin sub-system. We want to stress the fact that because of the out-of-equilibrium condition in this case, the further the departure from the equilibrium curve, the larger the magnetic energy stored in the out-of-equilibrium unflipped spins and then, the larger the heat release upon jumps through the last term in equation 8.1.

The specific heat of $Dy_2Ti_2O_7$ is indeed very small in the region of parameters shown in figure 8.1 ($T < 0.5$, $H < 0.6$) [41], and the thermalisation very good (dT/dt is very small, and the sample quickly adopts the mixing chamber temperature) [17], which means that the left hand side of equation 8.1 can be neglected with respect to the right hand side. The main contribution from that equation is given by:

$$T = T_{mch} + G^{-1}\frac{d\mathbf{M}}{dt} \cdot \mathbf{H} \tag{8.2}$$

This proportionality between temperature and heat release can be experimentally confirmed. In figure 8.2 we derive (a) the magnetisation, (b) the temperature of the sample and (c) the derivative of the magnetisation with respect to time multiplied by the field; from magnetisation and sample temperature measurements for different sweep rates at a temperature of ~ 80mK. The overall agreement of the last two panels on this figure demonstrates the validity of equation 8.2. Note that in the case of out-of-equilibrium, the last term on this equation heats up the system, both when the field is increased

[1]Given that the heat capacity and thermal conductivity of the plastic at these temperatures is very low, the contribution of the sample holder can be neglected

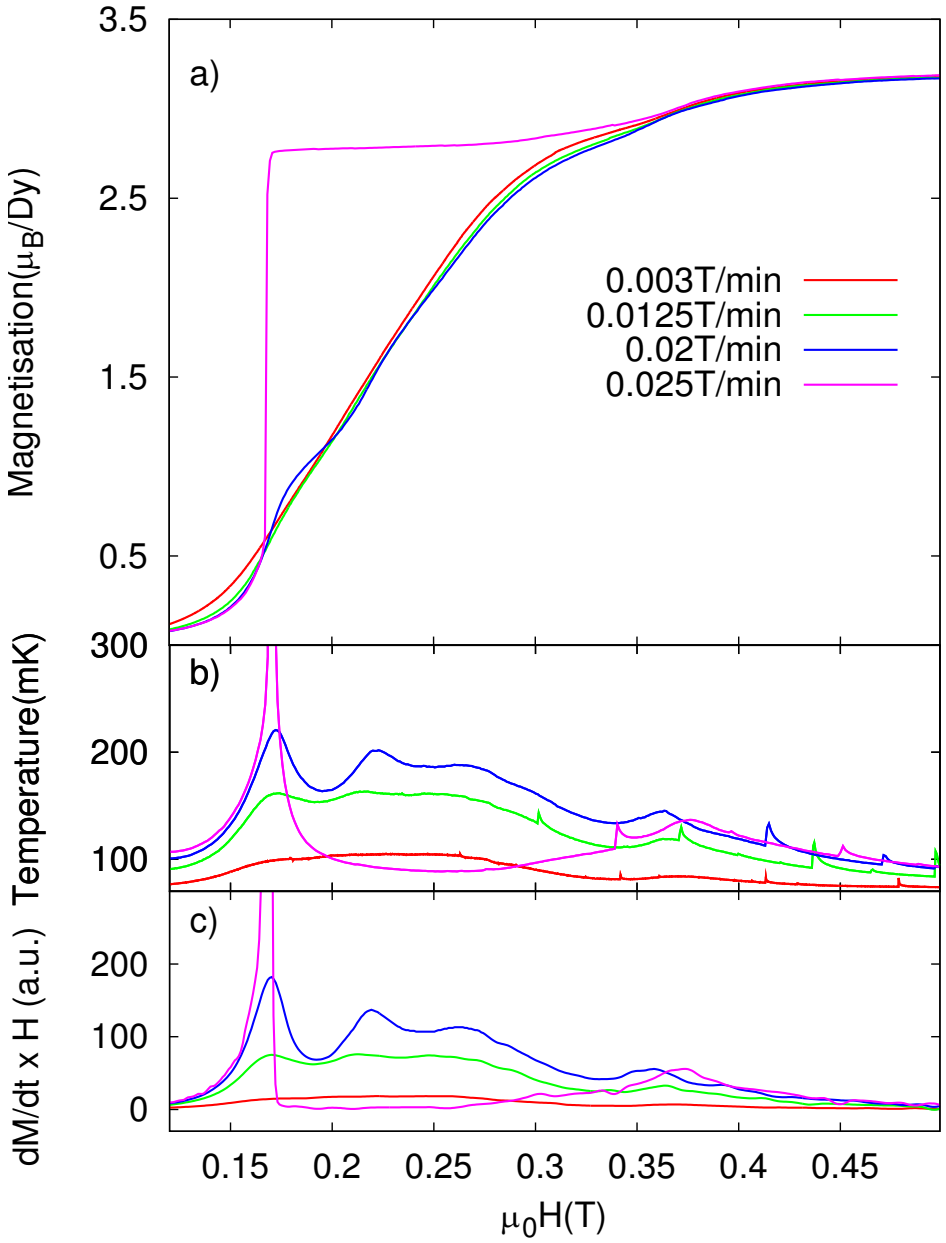

Figure 8.2: **a)** magnetisation vs. magnetic field for different sweep rates at base temperature ($\sim$ 80mK). **b)** temperature vs. magnetic field as measured from the RuO_2 thermometer on the sample for the same parameters of a). **c)** derivative of the magnetisation respect to time multiply by the magnetic field (*i.e.*, rate of heat generation) as a function of magnetic field. The similarity between b) and c) illustrates the validity of equation 8.2.

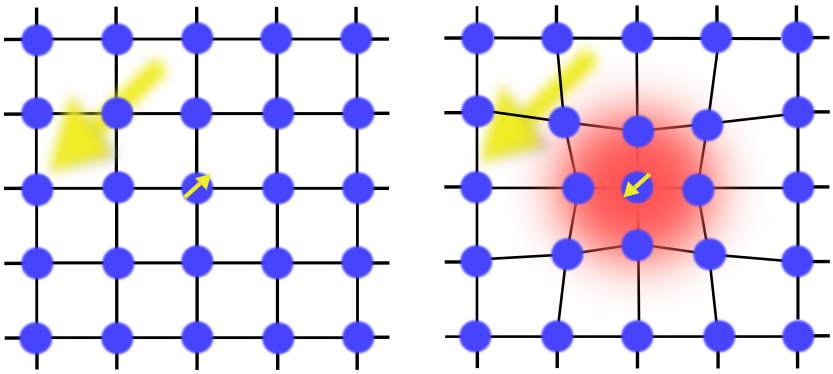

Figure 8.3: Sketch of the process by which the spins release their excess energy. The big arrow indicates the field direction. **Left**: a spin pointing opposite to the field direction will decrease its magnetic energy by flipping. **Right**: the spin flips by giving its excess energy to a phonon, locally heating up its environment.

and when it is decreased. This is because the system always seeks to attain the free energy minimum by decreasing its energy via the release of its excess in the form of lattice vibrations.

In order for the transition to happen, spins need to emit a phonon wave-packet with energy equal to the energy difference between the states with the spin flipped and not flipped (and of course, they need to conserve linear and angular momentum within Heisenberg's uncertainty principle). When this process occurs the material heats up as a result of the increasing amount of atomic vibrations due to the conversion of magnetic energy into phonon energy. This situation is sketched in figure 8.3.

To understand this out-of-equilibrium situation better, we can compare it with equilibrium in an Ising paramagnet. In an Ising paramagnet at finite temperature, the zero field state of the system has a value of entropy which is at its maximum ($S = Nk_B \ln(2)$) and an absolute value of magnetisation that is at its minimum ($M = 0$). The increase in magnetisation due to the application of an external magnetic field partially orders the system and hence decreases its entropy heating up the lattice through the magnetocaloric effect. In the case where the magnetisation is lowered by decreasing the magnetic field, the systems cools down as a result of the absorption of phonons by spins that flip opposite the magnetic field, increasing the entropy and balancing the free energy. The paramagnet behaves in this way provided that there are enough phonons to equilibrate the spin sub-system. When this is not the case and the phonon bath cannot equilibrate the spin

sub-system, it could happen that the system goes out-of-equilibrium. This was first proposed by Van Vleck [82] and is commonly called phonon bottleneck. This effect is particularly important at very low temperatures where the phonon density of states quickly vanishes, critically diminishing the spin-phonon coupling channels.

The case of $Dy_2Ti_2O_7$ has all the characteristics of a phonon bottleneck, namely: at low temperatures the system runs into out-of-equilibrium dynamics and it has a very small heat capacity. We can test the phonon bottleneck scenario by means of simulations of the spin ice and dipolar ice models, using the reduced Hamiltonian 2.2 (with and without dipolar interactions), which is constructed for a system that is allowed to quickly thermalise, *i.e.*, it does not explicitly take into account phonons.

We present simulations of a 1024 spins ($L = 4$) of the magnetisation as a function of magnetic field for different temperatures between 100mK and 600mK. The different curves were calculated using single spin flip Metropolis algorithm and waiting several Monte Carlo steps for equilibrium before averaging the data, and a similar preparation protocol, where the system is slowly cooled down at zero field from a temperature above $\sim$ 700mK (in our case 1.4K). For the nearest neighbour spin ice model (top left panel of figure 8.4) we can see very smooth curves at all temperatures, which is an indication that the pure spin ice system is able to equilibrate within reasonable Monte Carlo times. In the top right panel of the figure, this statement is supported by the H/T scaling which is reproduced to the lowest temperatures.

Instead, the dipolar model (bottom left panel of figure 8.4) presents a similar behaviour to the experiment. Below $\sim$ 700mK, the curves start increasing the magnetisation at a lower pace as the temperature is decreased, in clear contrast with the common trend of a cooperative paramagnet. This can be seen in more detail in the bottom right panel of the figure, where the magnetisation is explicitely plotted as a function of H/T. The departure from the H/T scaling occurs in the same way that in the real experiment (figure 7.2), showing that the sudden freezing of the dynamics at $\sim$ 700mK is not related with phonons. The comparison of the experiment with the simulation of the dipolar model seems to indicate that the freezing is due to the arrangement of dipolar interactions in the pyrochlore structure that generates a complex energy landscape, similarly to the cases of glasses discussed in chapter 5.

Different parts of the system can be located at different local minima in the energy landscape. When a spin flips, the landscape changes around that spin and the local heat released in the process can help overcoming the energy barriers for neighbouring spins to flip.

Although the dipolar model contains the freezing characteristics of the

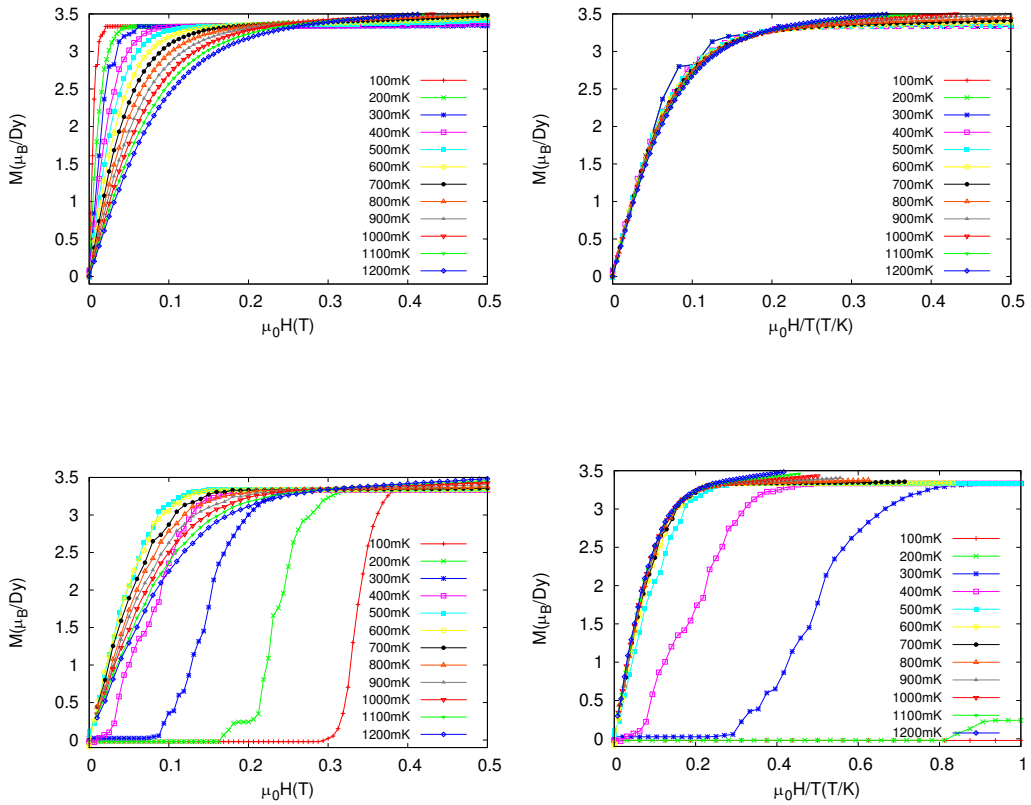

Figure 8.4: Simulations of the nearest neighbour model and the dipolar model at low fields for different temperatures after slowly cooling a system of 1024 spins ($L = 4$) in zero field from 1.4K. **Top right**: nearest neighbour model simulation of the spin ice system. The system equilibrates at all temperatures. **Top left**: the magnetisation scales with H/T to the lowest temperatures. **Bottom right** : the dipolar ice model shows similar behaviour to the experiment. The curves start increasing the magnetisation at a lower pace as the temperature is decreased, contrary to cooperative paramagnetic behaviour. The dipolar model contains the freezing temperature, which is the onset of out-of-equilibrium, without adding phonons or local temperature to the model. **Bottom left**: as in the experiment, the magnetisation does not scale with H/T at low temperatures.

real material, the exact jump behaviour cannot be simulated using this model. We performed extensive simulations searching for the exact behaviour at the jumps by varying the system size, equilibrium times, interaction parameters, etc.. None of these attempts succeeded at reproducing the experimental results.

We believe that local temperature should be added in order to reproduce the exact magnetisation features presented throughout the last chapters. Adding local temperature to the model implies a study of thermal conductivity, to finely tune the parameters for the competition between magnetic field sweep rate and thermal diffusion of heat. It also requires simulating larger systems in order to improve locality within the sample given that in an $L = 4$ system, except for very fine tuned parameters, the heat release by spins upon flip affects either all spins in the system (high thermal conductivity) or none of them (low thermal conductivity). Simulating larger systems and adding local temperature is a computationally challenging task.

Coming back to figure 8.2, we now discuss in detail the sample temperature information obtained for the sweep rate dependence. For slow sweep rates the sample is able to release to the mixing chamber the heat produced by the out-of-equilibrium flipping events, and hence the temperature increase is small. For the next two sweep rates 0.0125T/min and 0.02T/min, there is no jump in the magnetisation and consequently no jump in temperature, but in both cases the temperature increases in the form of a set of peaks and valleys. In the faster case the temperature jumps as in the case of figure 8.1.

One feature that is common to all sweep rates is a bump in temperature at 0.37T that corresponds to the abrupt change in slope in the magnetisation when it starts to collapse into the Kagome plateau. We commented on this feature when it appeared in figure 7.5 (in that case it happened at 0.25T because that data was corrected by demagnetisation), and we can see now how it affects the temperature of the sample. The flipping probability goes with the Boltzmann factors and since the spin component in the field direction of the apical spins is three times larger than the one for the basal spins, the basal spins are 'activated' later, and then one can assign the second bump to the activation of basal spin flip once the apical spins are almost completely polarised.

In the following section we will gain further insight into the dynamics of the magnetisation process in the region between zero field and the Kagome plateau by discussing several experiments exploring the time dependence of the magnetisation in different situations.

8.1 Dynamical issues

The out-of-equilibrium dynamics of $Dy_2Ti_2O_7$ below the freezing temperature has been investigated from the experimental point of view by means of ac susceptibility in a series of publications by Snyder *et al.* and Matsuhira *et al.* [45, 46, 47, 48] (see section 2.4). These experiments explored the response of the system to an alternating excitation field. The typical relaxation time was then obtained from the maximum of the susceptibility as a function of temperature. Because these studies were conducted on polycrystalline samples, the magnetic field dependence of the relaxation time was an entangled combination of contributions from all different crystallographic directions.

In a recent publication Giblin *et al.* [83] have studied the relaxation of the system by measuring magnetisation in a single crystal. They applied a very small field (< 50mT) and measured the magnetisation as a function of time after quickly ramping down to zero the external magnetic field. In this work, they were able to model the relaxation time characteristics, by applying to monopoles on $Dy_2Ti_2O_7$ the theory of the Wien effect usually used for electrolytes [84]. The outcome of their work is very limited in parameter space given that the theory that the authors proposed was only valid in their experiment at the base temperature of 360mK and at fields below 50mT.

We have investigated the relaxation process for different fixed magnetic fields applied along the [111] direction of the crystal. Because of the out-of-equilibrium dynamics and the sweep rate dependence of the magnetisation, we expect strong relaxation processes as a function of applied magnetic field. In particular, at base temperature, the magnetisation curve departs so strongly from the cooperative paramagnet behaviour that if we stop sweeping the field at a given point and wait long enough, we expect the system to relax towards the equilibrium magnetisation.

The relaxation times necessary to reach the equilibrium configuration could be rather long, which is why we opted to measure and compare the relaxation of the magnetisation at different fields for a fixed amount of time. The different panels in figure 8.5 summarise the information obtained. The experiment consisted of preparing the system by cooling the sample in zero field down to base temperature (~ 80mK), and then sweeping the magnetic field at 0.015T/min up to a fixed field which was held for 30 minutes, while recording the magnetisation. After this time, the field was swept at the previous sweep rate up to the Kagome plateau.

In the inset of figure 8.5 **a)**, the magnetisation is plotted as a function of magnetic field. When the field is stopped, the magnetisation increases at different rates for different fields. The relaxation during the holding time in the

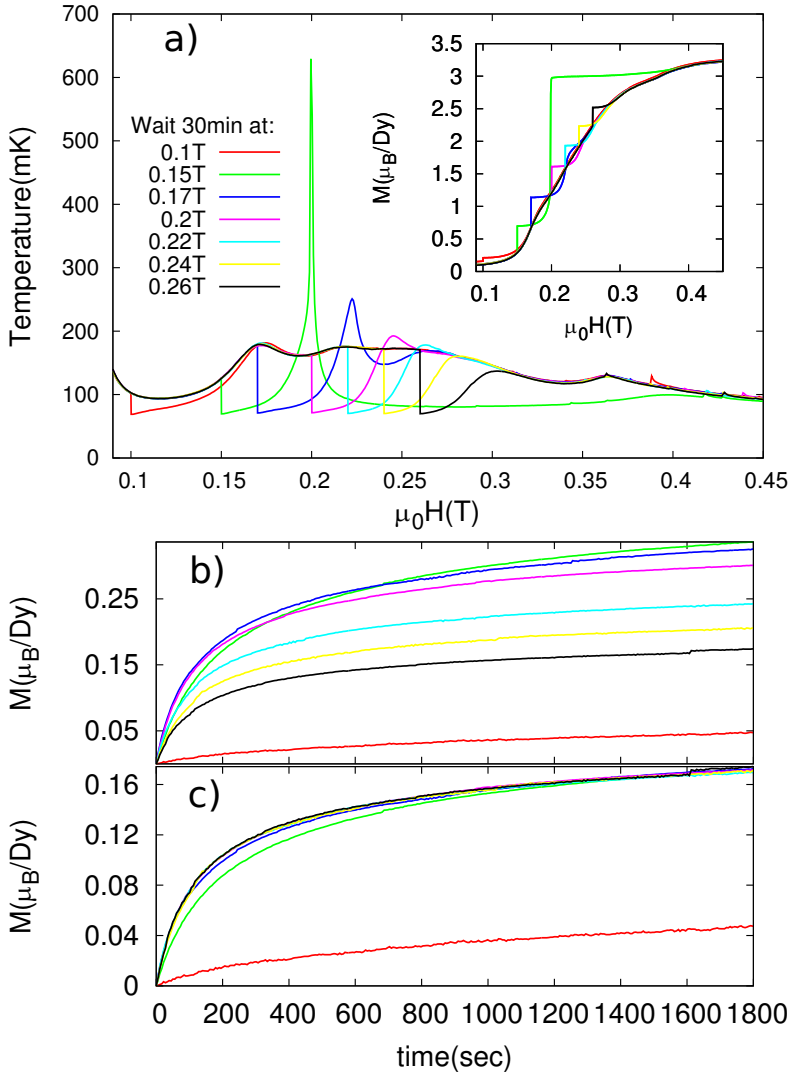

Figure 8.5: **a)**: sample temperature vs. magnetic field, stopping at different magnetic fields for 30 minutes. The system is prepared by cooling the sample in zero field down to base temperature ($\sim$ 80mK), then the magnetic field is increased at 0.015T/min to a fixed field where it is held for 30 minutes. After the waiting time, the magnetic field is increased at the same rate up to the Kagome plateau at the same. **Inset**: magnetisation vs. magnetic field measured simultaneously with the temperature. The system relaxes at different rates depending on the applied field. **b)**: magnetisation increase during the 30 minutes of holding time. The relaxation is maximum near $H = 0.15$T. **c)**: the magnetisation relaxation of the four larger measured fields 0.2T, 0.22T, 0.24T, 0.26T have been scaled by the multiplication of a constant increasing linearly with temperature which collapses most of the curves.

initial plateau at 0.1T gives very little magnetisation increase, in agreement with the energy of the spins being, on average, within a gap. In the case of a gap to the creation of monopolar defects, the magnetisation increase is slowed down by the need for monopoles to act as precursors of magnetisation changes by flipping out a string of spins. As the static magnetic field is increased over the initial plateau, the magnetic relaxation also increases substantially, up to $0.35\mu_B$/Dy in 30 minutes at 0.15T. When the sweep is restored after the holding time, the magnetisation initially plateaus and, for all cases except the one at 0.15T, joins the limiting curve of the slow sweep rates shown in figure 8.2. In that figure, the limiting sweep rate was larger than 0.02T/min, but in figure 8.5 at 0.15T the curve presents a jump at the slower sweep rate of 0.015T/min. This seems couterintuitive because the magnetic energy stored in the system (last term in equation 8.1) is what fuels the deflagration, and is being consumed during the holding time without jumping due to the increase in the magnetisation. Naïvely, we would have thought that this would have left the system in a more stable situation (stable against deflagration) than not waiting. On the contrary, when the magnetic field is swept again, the system experiences an abrupt jump in magnetisation very similar to the one studied in the previous sections (it has a maximum in temperature just above 600mK as can be seen in the main frame of this figure). This situation happens even at a slower sweep rate than the minimum sweep rate measured for jumps without the waiting protocol presented in figure 8.2. In conclusion, the waiting time destabilises the system.

One mechanism that could be responsible from this behaviour is the blocking of the apical spins. In equilibrium, strings have to form across the [111] direction in order to increase the magnetisation from zero to $3.33\mu_B$/Dy at the Kagome plateau. If we assume that the out-of-equilibrium magnetisation as a function of magnetic field develops in the same way as in equilibrium but with a much longer characteristic time scale, the uneven flip of apical spins with respect to basal spins will block sites for the strings to pass. That is, the strings need one apical spin per unit length in the [111] direction, and if there is no available spin near, strings will be impeded from advancing, and magnetic energy will again be accumulated throughout the system. This could lead to deflagration in the same way as explained in chapter 8.

The temperature dependence of these experiments can be seen in the main frame of figure 8.5. a) The temperature mimics the magnetisation through equation 8.2. Indeed $dM/dt \times H$ vs. H is equal to the temperature plot (not shown). During the holding time the temperature of the different runs decreases to the mixing chamber temperature. This is an indication that the power generated at fixed field is much lower than the cooling power of the cryostat. After the holding time, the temperature increases and overshoots

before collapsing into the characteristic temperature profile for the slow sweep rate at 0.015T/min.

In the bottom panels of figure 8.5 the magnetisation during the holding time is shown as a function of time. b) shows the raw data. In it, the trend of relaxations as a function of static magnetic field can be observed: after a slow relaxation at 0.1T there is a maximum at 0.15T and then the relaxation slows down. More importantly, in c) the magnetisation relaxation of the four larger measured fields 0.2T, 0.22T, 0.24T, 0.26T has been scaled by the multiplication of a constant increasing linearly with temperature. This allows us to collapse the curves to a very good degree within experimental error. The only curve that does not collapse is the one at 0.1T, for which the relaxation is much slower. This is a further indication of the possibility of a gap at low fields for the creation of deconfined monopoles to drive a magnetisation increase. The collapse of the other curves indicates that for these fields the magnetisation relaxation, M_r, has a unique functional form modulo a multiplication constant, that reads as follows:

$$M_r = A(H)f(t) \tag{8.3}$$

where $A(H) \sim aH + b$, with a and b constants. The linear dependence on magnetic field recalls the almost linear dependence of the magnetisation slope in this region of fields for the slow rates seen in figure 8.2.

In order to further investigate the relaxation process, we performed time dependence studies of the magnetisation relaxation at $H = 0.15T$ (the maximum relaxation from the previous experiment) and for two different temperatures: base temperature ($\sim$ 80mK) and 200mK. Given the fact that at base temperature the limiting sweep rate for jumps was greater than 0.02T/min (figure 8.2), it is sensible to think that as the holding time tends to zero for a field reached at a sweep rate inferior to 0.02T/min, no magnetisation jumps should occur. There will therefore be a critical holding time between 0 and 30 minutes (based on the experiment presented in figure 8.5), at that (H, T) point from which a jump will occur after restoring the sweep of the field. Indeed we see this behaviour in figure 8.6, in which we have plotted the curves obtained by sweeping the magnetic field at 0.015T/min up to 0.15T and holding it there for different amounts of times, both at base temperature and 200mK. After the elapsed time the field is increased at the same sweep rate up to the Kagome plateau, similar to the procedure used in figure 8.5.

In the main plot the dependence on holding time of the jumps can be seen. For the base temperature, waiting less than 15 minutes is not enough for a magnetic jump to occur, while at 200mK any holding time above 5 minutes evolves into the deflagration regime.

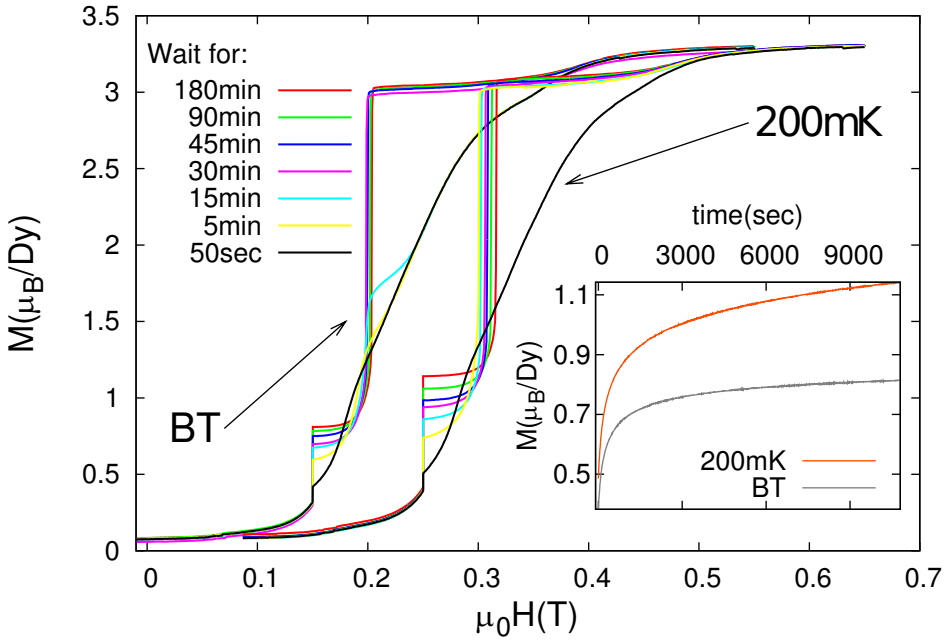

Figure 8.6: Magnetisation vs. magnetic field after cooling the sample in zero field down at base temperature ($\sim$ 80mK) and at 200mK (offset in field for clarity). The magnetic field is swept at 0.015T/min up to $H = 0.15$T where is held fixed for a given time. The curves in the plot correspond to different holding times from a minute up to 3 hours. After the holding time the field is increased up to the Kagome plateau at the same rate as previously. **Inset**: magnetisation increase during the holding time.

The plateau reached after the magnetic jump has a very similar value for all the holding times at both temperatures. This is different from the case of the field coolings depicted in figure 7.5 where the magnetisation of the plateau after the magnetic jump strongly depended on the magnetisation at which the jump was triggered.

The role of the temperature can be seen in the inset, where relaxation of the magnetisation is plotted for the longest holding time at the two temperatures. The relaxation at 200mK is double that at base temperature. These two curves cannot be made to collapse by simple multiplying a scaling factor.

The underlying mechanism for the dynamical behaviour of $Dy_2Ti_2O_7$ remains an open question that needs more simulations and further experimentation to be understood thoroughly.

Chapter 9

High field magnetisation along the [111]

This chapter is devoted to the study of the metamagnetic transition under an applied [111] magnetic field at low temperatures that drives $Dy_2Ti_2O_7$ from the Kagome ice state characterised by a magnetisation plateau at $3.33\mu_B$/Dy, to saturation at $5\mu_B$/Dy. In the Kagome state, one of the basal spins in the Kagome plane is still pointing against the magnetic field direction, supported by the ice rules. During the saturation process, the magnetic energy gained by flipping this spin overcomes the ice rule energy.

As we have already discussed in section 2.3.3, the numerical study of the characteristics of this process paved the way for the monopolar picture in its prediction of a liquid-gas-like condensation of monopoles [35]. The monopolar theory predicts a clear first order phase change where monopoles in the gas phase, driven by their mutual (Coulombic) interaction, condense as the temperature is decreased. In this way, monopoles in $Dy_2Ti_2O_7$ were used to explain the experimental first order phase transition found by Sakakibara *et al.* in their study of magnetisation as a function of a [111] applied field [29] (shown in figure 2.11).

In section 2.3.3, we also introduced the fact that in thermodynamic equilibrium, small tiltings away from the [111] direction generated an order on the Kagome planes, and that there was a Kasteleyn-like transition for the magnetisation in the perpendicular direction. This transition was explained in terms of a topological dimer-monomer transition in the nearest neighbour model. Both the topological dimer-monomer transition in a tilted field and the first order transition have been measured experimentally on either $Dy_2Ti_2O_7$ or $Ho_2Ti_2O_7$ [37, 29]. While the first was predicted [34] before being measured, the second was explained after experimentation [34, 35].

However, the question of their compatibility was never addressed. How does the tilting affects the first order character, or how do dipolar interactions affect the Kasteleyn behaviour of the perpendicular magnetisation?

These questions were partially addressed by Sato *et al.* [39] who studied the field-angle dependence of the magnetisation. These experiments, shown in figure 2.13, yielded the intriguing result that the transition to saturation split into two distinctive peaks for small rotation angles (below 10°) away from the [111] towards the [112] direction, with no splitting for rotations toward the [110] direction. These findings allowed us to understand the apparent incompatibility between the experimental results obtained in references [29] and [41] which found quite different results measuring the same transition to saturation under a [111] applied magnetic field by means of two very different experimental techniques: magnetisation and heat capacity. The magnetisation studies measured only one peak at the transition, while heat capacity could discern the emergence of a second peak as the temperature was decreased, presumably due to a small misalignment in accordance with Sato's result. To the best of our knowledge, the reason for the splitting remains a mystery.

Here we study by means of magnetisation experiments and numerical analysis the transition from Kagome ice to saturation. Also, we have revisited the field-angle experiment by Sato *et al.* using Monte Carlo simulations.

9.1 Temperature dependence

A well defined, completely ordered state in which all the spins have a positive component pointing along the [111] crystallographic direction is achieved by applying a large magnetic field in this direction. Such a state is referred to as saturation because it possesses the maximum magnetisation ($5\mu_B$/Dy) along this direction. An important difference with the situation where the field is applied along [100] is that in [111], the saturated state allocates a monopole in each tetrahedron given that the basal spins in each tetrahedron point either all three into the up tetrahedra or all three out of the down tetrahedra (see right case in figure 9.1 further below).

Departing from this state and decreasing the magnetic field at fixed temperature, one of the basal spins in the Kagome plane of each tetrahedron flips against the magnetic field (bottom case in the same figure), driven by entropy and the energetics of recovering the ice rules, and thus the system reaches the Kagome state. In thermodynamic equilibrium, the Kagome state acquires a configurational entropy provided by the symmetry of the choice

of the spin pointing against the magnetic field from all the three basal spins on the Kagome plane perpendicular to the [111] direction.

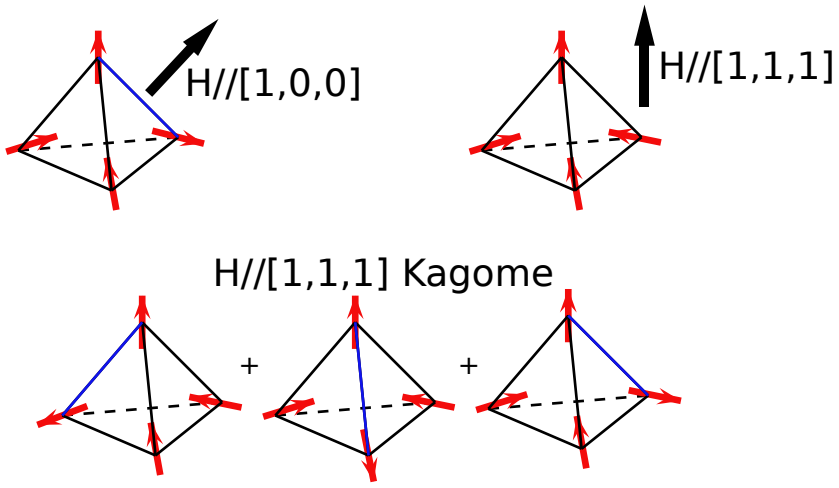

Figure 9.1: For the case where the magnetic field is applied along the [100] direction, the saturated state preserves the ice rules (**left**). In the case where the magnetic field is applied along the [111] direction, saturation breaks the ice rules (**right**). Starting from saturation in [111], and decreasing the magnetic field at fixed temperature, one of the basal spins on the Kagome plane of each tetrahedron flips against the magnetic field, driven by entropy and the energetics of recovering the ice rules. The Kagome state is characterised by three degenerate possibilities for the arrangements of spins in the basal plane of the tetrahedron (**bottom**).

Still in equilibrium, a small perpendicular field (non-zero projection on the Kagome planes) will bias the choice of the basal spin that flips in each tetrahedron, favouring the one with higher component along the perpendicular field (or two for a fine tuned direction) over the others. This bias on the choice of the spin grows very quickly with angle because it is proportional to the Boltzmann factor.

We have investigated these different states experimentally. We start by showing a portion of the field sweep magnetisation for different temperatures that reproduces the experiments of reference [29] used in section 2.3.3 to explain the [111] magnetisation process. In figure 9.2 we show the magnetisation after cooling the sample in a field of 0.7T, well into the Kagome plateau. From this point, the magnetic field is swept up to 1.6T at a field sweep rate of 0.0125T/min. Note first that, the magnetisation of the 300mK,

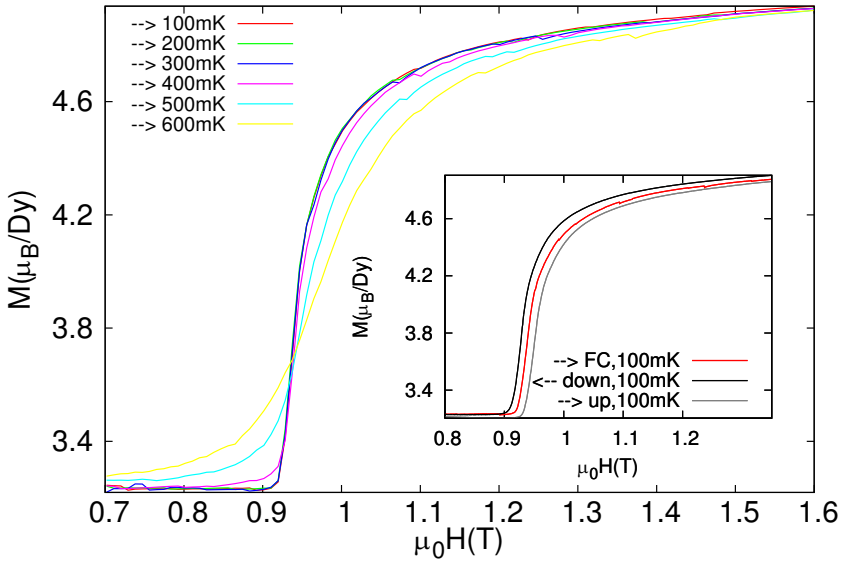

Figure 9.2: Magnetisation vs. field at different temperatures. The system was prepared by cooling the sample at fixed field of 0.7T. Next, the field was swept at constant temperature up to 1.6T. The arrows on the label indicate the direction the field was moved. The magnetisation of the 300mK, 200mK, and 100mK curves coincide. **Inset**: hysteresis loop at 100mK after cooling the sample in a field of 0.7T. The system responds differently whether the magnetisation is increased after cooling the sample in field or after returning from high fields. Hysteresis can be observed between up and down curves, but different up field sweeps, the red and the gray, do not coincide.

200mK, and 100mK curves coincide within experimental resolution. Beside this, the figure agrees very well with the experimental results by Sakakibara *et al.* shown in the introductory section (figure 2.11), showing a steep increase in magnetisation, steeper as the temperature decreases, followed by a rounded approach to saturation. Also, similarly to the previous experimental report, the curves cross at a unique point in the (M,H) plane for all temperatures. In the inset of the same figure, a very special hysteresis loop is depicted. The 100mK red curve is obtained by increasing the magnetic field up to 1.6T after cooling the sample in a field of 0.7T. The black curve is measured right after the red one by decreasing the magnetic field from 1.6T back down to 0.7T. Finally, in the gray curve the magnetic field is increased up again to 1.6T. We observe hysteresis between up and down curves similarly to the bottom right panel of figure 2.11, but, to our surprise, different up field sweeps, the red and the gray, do not coincide. This experimental

curve shows that the transition to saturation depends on the preparation of the system, and in particular, on the configuration of the Kagome plateau which we used as a starting point. This behaviour is a clear indication of departure from equilibrium.

We know that the experimental error in the orientation of the sample lies within $\pm 3^\circ$ from the applied field direction, and also, that we cannot control the direction of the deviation. Assuming that we were indeed away from the apical axes, it is possible to understand the difference between the red and gray curves as a consequence of different initial states at the Kagome plateau.

As previously discussed, cooling the sample in field would generate a Kagome ice configuration with a bias of $\exp\left(\frac{2m|h|(\cos\theta)}{k_B T}\right)$, where θ, is the tilting angle away from [111], m is the basal magnetic moment in that direction, and $|h|$ is the magnitude of the applied magnetic field. This is the red curve for a field of 0.7T. In the case of the gray curve the bias would be given by the same expression but using the transition field (~ 0.9T) instead of 0.7T. This is so, because the basal spins have been exposed to fields up to 1.6T (black curve) which saturates them almost completely. As the field goes down some of these spins flip at ~ 0.9T. At low temperature and between 0.7T and 0.9T the dynamics is strongly suppressed by the dipolar interaction and the absence of monopoles, which suggests that the initial state for the gray curve should be similar to the state of the black curve just after the transition. Hence, the Boltzmann factor for the field in the Kagome plane has to be calculated using the transition field. In this picture, the difference in the bias fields should be responsible for the differences between the red and gray curves.

An extension of last figure is plotted in figure 9.3, where we show hysteresis loops similar to the one shown in the inset of figure 9.2, but this time at different temperatures. The starting point of these curves is attained by cooling the sample in a field of 0.7T, after which the field is swept to 1.6T. Following this preparation, the magnetisation of the system is measured first down to 0.7T (green curve), and then back up to 1.6T (blue curve). The panels on the left show the temperature as a function of field measured by the thermometer on the sample for the same field sweeps. We recall that the liquid-gas like first order transition measured in reference [29] had a critical end point at about 400mK (see figure 2.12), below which there was a latent heat associated with the transition. In the bottom left panel, corresponding to a field sweep at 100mK, we can see a marked asymmetry between the down and up field sweeps: in both cases there is an increase in the temperature of the sample upon crossing the transition field. However, the down sweep heats up considerably less than the up sweep. Going up in mixing

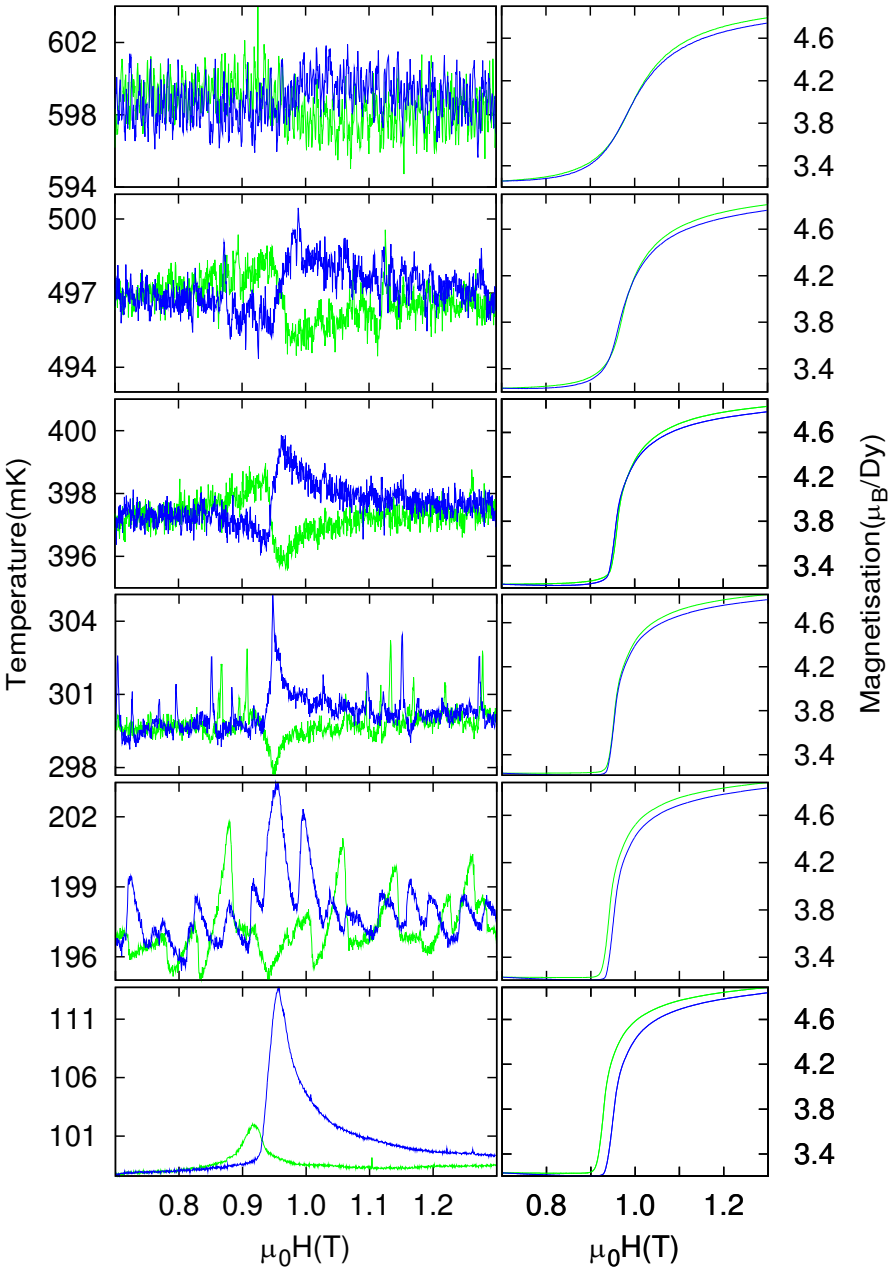

Figure 9.3: Hysteresis loops starting from a state attained by cooling the sample in a field of 0.7T followed by a field sweep up to 1.6T. The green curve is the down sweep and the blue is the up sweep. **Left**: panels show the temperature of the sample measured by our experimental configuration as a function of field. Note the magneto-caloric effect persisting up to 600mK. The undulations at 200mK are probably due to mixing chamber stabilisation problems. **Right**: panels show the magnetisation traces corresponding to the left panels.

chamber temperature, we can see that the magneto-caloric effect appears in the form af a mirror reflected temperature pattern, clearly discernible above 300mK. Above 300mK the sample cools down on crossing the transition point from the saturation side to the Kagome side and heats up on crossing the transition in the opposite direction.

Assuming the sample is able to equilibrate within the characteristic time of the experiment, this can be understood in terms of degrees of freedom. In a perfect adiabatic case, when the field is decreased, new degrees of freedom open, given by the possibility of flipping a basal spin against the magnetic field, and the entropy becomes larger at expense of taking heat from the environment. As a consequence the sample cools down. In contrast, increasing the magnetisation towards saturation from the Kagome side by increasing the applied magnetic field orders the system, diminishing its entropy and releasing energy.

In our case the experiment is not performed under perfect adiabatic conditions, and for this reason the temperature increase and decrease cannot be easily translated into energy. However, the mere existence of magneto-caloric traces above 300mK is an indication that the system is able to equilibrate at these temperatures. In particular, we see that the magneto-caloric effect persists at least up to 600mK where it starts being buried in the noise of the measurement.

Interestingly enough, the typical magneto-caloric mirror trace for up and down sweeps across a first order phase transition is only seen above 300mK, where the magnetisation in the right panels of figure 9.3 does not show discernable hysteresis. Previous magneto-caloric studies did not concentrate on the sign of the effect, and only showed measurements above 350mK where the first order transition reaches its critical end point [38]. After that the transition becomes a cross-over.

Coming back to the bottom panel, it seems that the magneto-caloric effect is hidden by some secondary effect that heats up the sample regardless the direction which the transition is crossed. This is reminiscent to the out-of-equilibrium behaviour at low fields and low temperatures seen in the previous sections, where the spin subsystem was badly coupled to the phononic bath making thermalisation difficult. In that case the law governing the dynamics was the conservation of energy instead of the conservation of the free energy, which yielded a negligible effect on the entropy of the system. The main difference here is that the freezing temperature has significantly dropped from $\sim$ 700mK to $\sim$ 400mK. This difference in temperature could be probably understood in terms of the landscape of energy provided by the long range interaction in both cases. At zero field there are more energetically favourable possibilities for spins on the pyrochlore lattice than at a field that sets the

system in the Kagome state. The order of the Kagome state can be associated with a smoother and shallower energy landscape. In contrast to the situation at low fields, no deflagration can be observed in our high field measurements, other than the abrupt jump to saturation experience by the magnetisation of the system.

Returning to figure 9.3, it is also possible that due to the out-of-equilibrium dynamics seen at low temperatures in previous sections, the nucleation of excitations could be constrained by a phonon bottleneck. In that case, the excitations would be prohibited by conservation of energy, since there would be no phonons to carry away the excess energy, and the system could super-magnetise, similarly to a super-heated liquid in which the phase transition is suppressed because of the lack of nucleation centres.

Just to make it clearer, we would like to summarise the current understanding on the transition between the Kagome ice state and saturation. One way to do this is to think of the saturation configuration as an ionic crystal of monopoles in which the up tetrahedra allocate the monopoles given by three spins pointing in and one pointing out, and vice versa for the down tetrahedra. In this picture, as the field is decreased, energy is absorbed from the enviroment to destroy the bonds of the crystal by annihilation of monopoles. At the transition point, this should maintain the temperature constant; while islands without monopoles grow until the transition is complete when there are nearly no monopoles left. The inverse process happens when the field is increased from the Kagome plateau; an increasing number of monopoles clusters into a lower energy configuration, giving away the excess energy to the system, while growing in size until completing their crystallisation at saturation.

The experimental evidence for a first order transition comes from the hysteresis seen in magnetisation below 400mK and, from the transition line that was shown to be in agreement with a Clausius-Clapeyron relationship for the entropy release measured with the magneto-caloric effect as a quasi-discontinuity [38] (although we note that the system studied in that work was clearly not in equilibrium). The specific heat experiments could resolve neither a very sharp peak nor the latent heat (although the latter should, in theory, be huge) which would have confirmed the first order transition scenario [41]. This failure was ascribed to the fact that the critical line is nearly parallel to the temperature axis. From the numerical point of view, there is a clear prediction of a first order transition seen as the condensation of monopoles to form an ionic crystal. In these Monte Carlo simulations, hysteresis is seen in the corresponding M vs. H characteristics when further neighbour or long range dipolar interactions are included, but it is absent

from the simulations incorporating only nearest neighbour interactions.

We now pass to study the hysteresis seen at the lowest temperatures.

9.2 Hysteresis loops

We have performed several experiments in which we measured hysteresis loops at base temperature ($\sim$ 80mK) starting from different initial configurations. The results of these experiments can be seen in figure 9.4, where two different loops as a function of internal magnetic field are shown. The sweep rate for all curves was 0.0125T/min and they were measured at a base temperature of $\sim$ 80mK. At first sight, in both cases the data corrected by the effect of the demagnetisation field are very sharp just at the transition, and become rounded as the magnetisation approaches saturation.

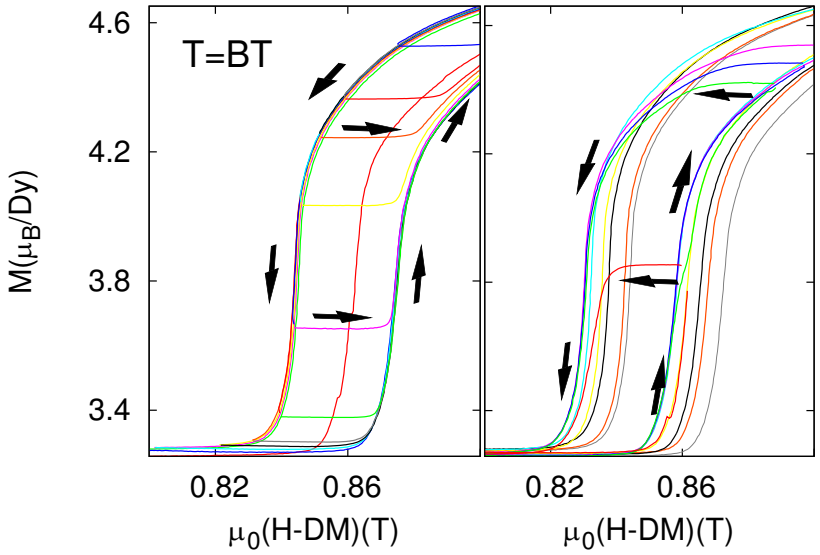

Figure 9.4: **Left**: loop obtained after cooling the sample in a field of 0.85T, from which the field was increased to 1.6T. From this point, the curves went down every time to higher field values: 0.85T, 0.87T, 0.89T, etc. and then back again up to 1.6T. **Right**: loop obtained by field cooling at a fixed field of 0.825T, from which the field was swept up and then back down to the starting field, reaching fields of increasingly higher values: 0.91T, 0.94T, etc. Both loops were obtained by sweeping the field at 0.0125T/min at the base temperature of $\sim$ 80mK. The arrows indicate the field sweep direction. We have changed the colour of the curve to indicate each time that the field sweep direction was changed.

In the loop of the left, the starting point was obtained after cooling the sample in a field of 0.85T, from which the magnetic field was increased to 1.6T. As in the inset of figure 9.2, this curve traverses through the middle of the loop. Every time smaller loops were obtained as the curves went down from 1.6T to higher field values: 0.85T, 0.87T, 0.89T, etc. and then back again up to 1.6T.

We can clearly see that once the magnetic field has reached 1.6T, saturating the sample, the up and down curves always follow the same magnetisation trace independent of the history of the run.

Another way of preparing the system is shown in the right panel of the same figure, where we show a different hysteresis loop. The starting point for this loop was achieved by cooling the sample in a fixed field of 0.825T. From this point the field was swept up and then back down to the starting field, making the loop every time larger by reaching fields of increasingly higher values: 0.91T, 0.94T, etc. In this case, the initial configuration probes how the hysteresis behaves when starting from a field cooling. Recall, that the curve starting from a field cooling at a field which sets the system into the Kagome plateau crosses through the middle of the hysteresis loop obtained by sweeping the field down from saturation and then up again. The loop in the figure shifts little by little to higher fields as the magnetic field reaches larger values, until it finally coincides with the one in figure 9.2. A recurrent feature from both plots are the plateaux joining the up and down sweeps. In the left panel of figure 9.4 the plateaux of constant magnetisation that form at the beginning of each up sweep join the gap between the up and the down curve and are the expression of the hysteresis itself.

As discussed previously, one possible explanation for the loop shifting is that the Kagome planes become increasingly magnetised by the increase in the perpendicular field. In that case the history from the field cooling would be erased only for the curves in which the sample was exposed to high field values (large perpendicular component for tiltings).

9.3 Field-angle magnetisation

The second peak appearing in heat capacity (Higashinaka *et al.*[41]) and susceptibility (Higashinaka [85]) experiments, for a field being swept in the [111] crystallograhic direction promoting the system from the Kagome plateau (0.5T to 0.8T) to saturation (above 0.9T), came as a surprise because it was not predicted by any theory. The experiment by Sato *et al.* [39] described in section 2.3.3 has proven to be very important in identifying its nature. In their experiment they found that as the field was rotated around the $[\bar{1}10]$

direction, from [111] towards [112], there was a narrow region of angles, between 1 and 10 degrees, where the [111] magnetisation presented a second peak (see figure 2.13). In this way, this experiment shed some light on the origin of the second peak, assigning it to a misalignment. Furthermore, it provided also the direction of the misalignment, since it was found that there was no secondary peak when the field was rotated from the [111] to the [110] direction.

We have analysed the field rotation experiment by Sato *et al.* from a different perspective with the help of numerical Monte Carlo simulations, hoping to understand the microscopic origin of the second peak. Although this was not fully achieved, we found what we believe is a very good method to test modifications to Hamiltonian 2.2 in order to obtain better agreement between simulations and experiments.

As the magnetic field is rotated around the $[\bar{1}10]$ direction, the field sweeps the plane containing the [110] direction at $-35.3°$, the [111] direction at zero degrees and the [112] at $19.5°$. We reproduced the rotation experiment numerically by computing the magnetisation of the sample in the direction of the magnetic field, M_H, to compare with the experimental data. In figure 9.6 we show experimental data from Sato *et al.* along with the results of simulations, for different fixed fields at 300mK. The simulations were performed on an $L = 8$ (8192 spins) system with nearest neighbour interactions, and an $L = 4$ (1024 spins) system with long range dipolar interactions computed by Ewald's method, for the same parameters (H, T). We have also superimposed the magnetisation value for the specific arrangements (on average) of spins in a tetrahedron depicted in figure 9.5. These curves are shown as full lines in gray colour and the notation used is defined on the up tetrahedra by assigning a four-component vector to each average configuration as seen in figure 9.5. From the four components, the first represents the average value in a given configuration of the apical spins defined by the field direction [111] at zero degrees ($< a >_{111}$), and the other three the average value of the other three basal spins ($< a >_{1\bar{1}\bar{1}}, < a >_{\bar{1}1\bar{1}}, < a >_{\bar{1}\bar{1}1}$). In this way, each of the gray lines represents a state that is defined by the average value of the spins on a tetrahedron $[< a >_{111}, < a >_{1\bar{1}\bar{1}}, < a >_{\bar{1}1\bar{1}}, < a >_{\bar{1}\bar{1}1}]$. The sign is defined positive for out spins as can be checked in the figure.

For example, $[1, -1, 1, -1]$ refers to an apical spin collinear with the external magnetic field (the first coordinate), and one out of three basal spins (the positive) pointing opposite to it[1]. In the case of the Kagome plateau, the gray line representing the state in this notation is: $[1, -1/3, -1/3, -1/3]$.

[1]Recall that the projection of the spin on the field has a different sign for the apical spin as compared to the basal spins with respect to the in-out convention (equation 2.4).

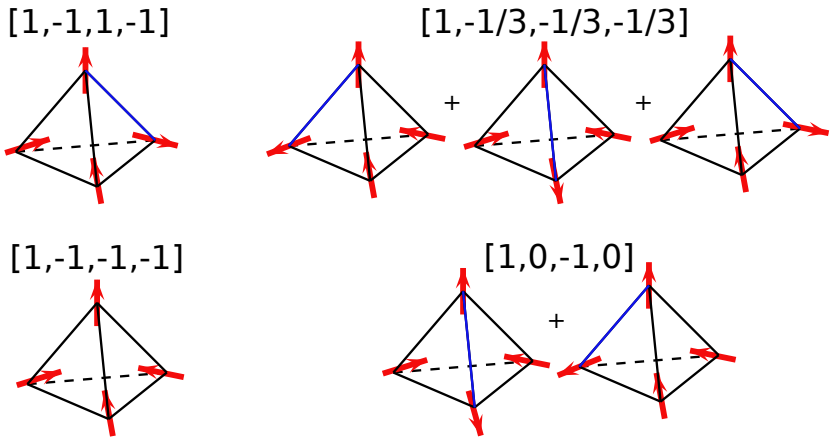

Figure 9.5: Notation for the gray lines plotted in figure 9.6. The four components represent the average value of the four spins on a tetrahedron $[< a >_{111}, < a >_{1\bar{1}\bar{1}}, < a >_{\bar{1}1\bar{1}}, < a >_{\bar{1}\bar{1}1}]$, with the subindex being the direction of each spin. The sign of each component is defined positive for the spins pointing out.

In this case the basal spins are equivalent and they point on average inwards a third of the time.

The configuration lines (gray) help us to understand the experiment, acting as guidelines for limiting behaviours. For instance, saturation, i.e., the $[1, -1, -1, -1]$ configuration is reached at high fields and matches the data in figure 9.6. The $[1, -1, 1, -1]$ configuration becomes increasingly populated as the field is increased for fields rotated towards the [112] direction. In turn, the Kagome state strictly lives at zero angle for the fields depicted. Finally, as the magnetic field is rotated from [110] towards [111], the curves for lower fields collapse into the $[1, 0, -1, 0]$ configuration which privileges the 'y' and 'z' configurations.

As we mentioned before, there is a departure from this limiting behaviour which eventually transforms into the mysterious second peak. This can be found for fields tilted from [111] in the direction [112] where, close to zero angle, the curves depart in the direction of the Kagome limiting curve. It is around these angles that the double peak feature is found.

Note that the tetrahedra configuration lines (gray) agree perfectly well with the nearest neighbour simulated data in the top panel of figure 9.6, and for the dipolar model, they slightly depart at small angles close to [111] in the direction [112] with the same trend as the experimental data (bottom panel).

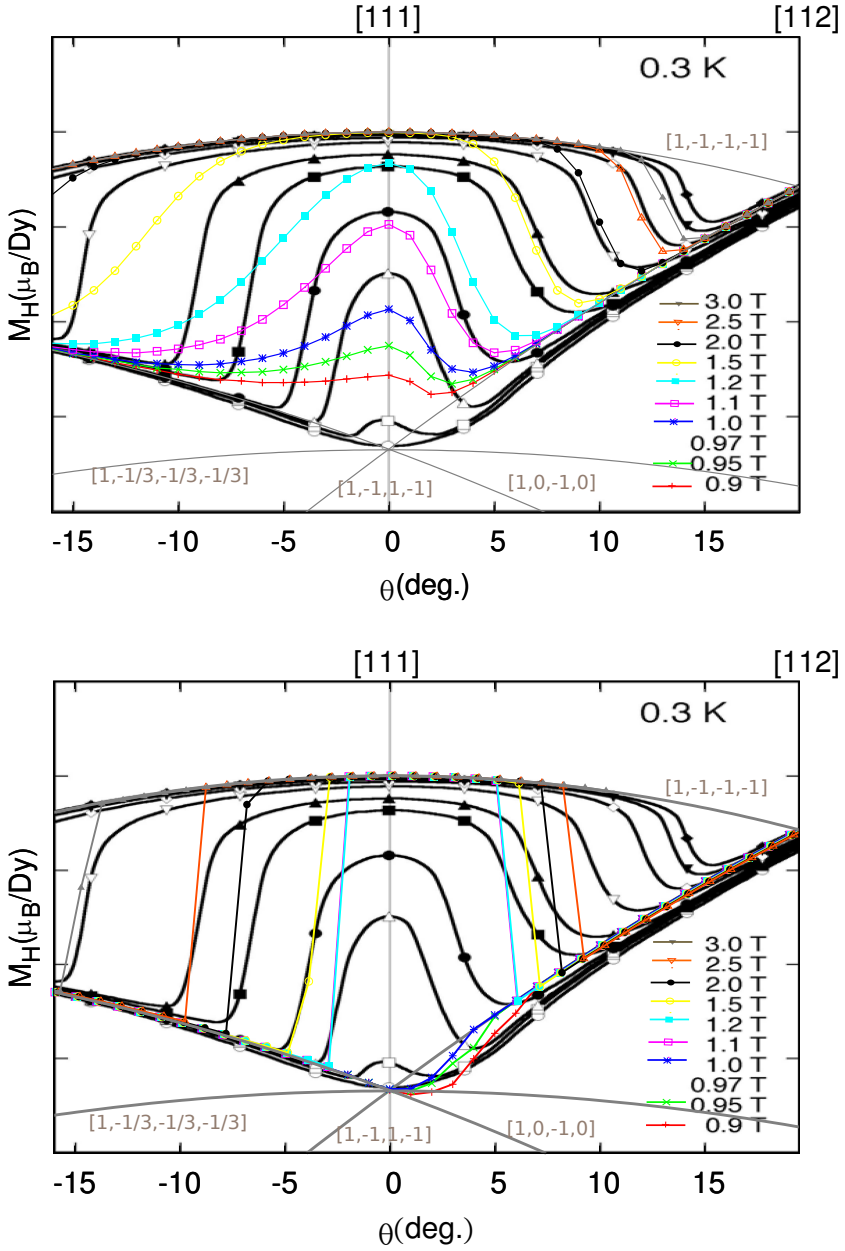

Figure 9.6: Magnetisation in the direction of the magnetic field as a function of angle for different magnetic field magnitudes. Superimposed to the experimental value of Sato *et al.* [39] in full black we have plotted: **Top**: nearest neighbour interaction model simulation for $L = 8$ (8192 spins), **Bottom**: dipolar model simulation with Ewald summation for an $L = 4$ (1024 spins). The dipolar model reproduces the first order transition but fails to reproduce the less abrupt decay towards the [112] side. This last is very well reproduced by the nearest neighbour model.

From the comparison of simulation with experiment we can see that the deviation of the data and the gray lines is small which implies a small deviation angle from the plane perpendicular to the $[\bar{1}10]$. Remember that the exact deviation angle within $\pm 3^\circ$ in this plane could not be controlled in the experiment. At intermediate angles and fields the experiment and simulation differ considerably. The simulated data for the nearest neighbour model in the top panel qualitatively agrees with the measured one for positive angles. In contrast, for negative angles the similarities are less clear with very sharp contours with plateaus for the experimental data, as opposed as smooth peaked curves for the nearest neighbour model. On the other hand, the dipolar model on the bottom panel gives very sharp transition peaks as a function of angle at the same positions as the experimental data. This reproduces reasonably well the behaviour for negative angles but the good agreement found for positive angles in the nearest neighbour model dissapears.

Unless a finite size effect were ascribable to the difference between Sato's experiment and Monte Carlo simulations, we believe that the dipolar model for spin ice is incomplete. Previous work by Yavors'kii *et al.* [22] tried to adjust second and third neighbour interactions in Monte Carlo simulations of the dipolar model, to fit the parameters of several experiments, moved by the need to improve the simulations from making qualitative to quantitative predictions. We performed the angle rotation simulations with the second and third neighbour interactions proposed by them, with various different combinations of parameters, without ever finding an acceptable match with experiment.

As a general conclusion we believe that in order to reproduce and fully understand the low temperature dynamics of $Dy_2Ti_2O_7$, we will have to go beyond the dipolar model adding new ingredients such as those required to account for the deflagration discussed in previous chapters.

The rotation experiment of Sato *et al.* is likely to provide a good numerical test of such models which, we hope, will evolve into a more quantitative tool to predict the behaviour of spin ice pyrochlores.

Chapter 10

Conclusion

Throughout this thesis we have investigated the magnetisation process in $Dy_2Ti_2O_7$ as a function of magnetic field and temperature, in single crystalline samples oriented in different directions with respect to the magnetic field.

In chapter 5 we expanded the experiments performed by Snyder *et al.* to single crystals of $Dy_2Ti_2O_7$, by measuring the temperature dependence of ZFC and FC curves for different fields applied to the [100] crystallographic axis. We found that, in agreement with previous experiments made on polycrystalline samples, there is a bifurcation between the ZFC and the FC curves as a function of temperature that indicates the onset of the system's departure from equilibrium. As in the case of the polycrystalline samples, we measured strange behaviour for the field dependence of the bifurcation point: the temperature at which the curves separated increased with increasing field, instead of decreasing which is the usual case for spin glasses.

Based on these results, we decided to prepare the samples before each experiment using a protocol by which we heated up the sample to above 700mK and then cooled it down to the desired temperature. In this way, we made sure to erase any memory from the history dependence of the magnetisation.

In the remaining chapters, we focused on the field dependence of the magnetisation for applied fields along different crystallographic directions.

In chapter 6 we studied the excitations from the spin ice ground state when a magnetic field was applied to the [100] direction of the crystal. By means of neutron scattering experiments, we were able to confirm the effective monopolar picture proposed for $Dy_2Ti_2O_7$, in which the ice rule-breaking excitations of three in (out), one out (in) corresponded to monopolar particles with + (-) charge. We measured the string of spins connecting two oppositely charged monopoles, similar to the Dirac strings in field theory,

by comparing the diffraction pattern of a very low density of strings with a simulation of random walks of strings on the pyrochlore. The agreement of the experiment with the model confirmed the string and monopolar scenarios. The existence of these strings agrees with the predictions of a 3D Kasteleyn transition, *i.e.*, an entropically driven topological transition separating a phase without strings from a phase with a proliferation of string defects. In the pure spin ice theory (nearest neighbour interactions) for temperatures much lower than the ice rule temperature J, the magnetisation was calculated using Monte Carlo simulations and fitted to scale as H/T, as in a cooperative paramagnet. We showed that for the real material $Dy_2Ti_2O_7$ at temperatures above the freezing temperature (bifurcation point), there is a visible effect of monopoles that translates into a rounding of the transition, but we were still able to measure the underlying convex curvature and partial H/T scaling characteristic for the Kasteleyn transition on spin ice. We could not, however, explain the hysteresis that shows very different magnetisation behaviour for up and down sweeps. Further experiments, both numerical and real, should be done to clarify this issue.

In chapter 7 we presented the first of a long set of experiments dedicated to studying the out-of-equilibrium dynamics of $Dy_2Ti_2O_7$ at temperatures below the freezing temperature. In equilibrium, the system behaves like a cooperative paramagnet, but as the temperature is decreased below the freezing temperature, out-of-equilibrium dynamics signals the departure from the cooperative paramagnetic behaviour. We found that the magnetisation as a function of field presents reproducible jumps for the lower temperatures as the magnetic field is swept through the temperature dependent threshold. By computing the demagnetisation factor, we were able to confirm that the jumps are out-of-equilibrium triggered events that, once ignited, do not stop even though the internal field becomes lower than the threshold. We further proved the existence of a dependence on the field sweep rate such that below a certain sweep rate (depending on the temperature) the magnetisation evolved without jumps.

By measuring the magnetisation as a function of magnetic field for spin systems prepared by cooling the sample at different fields, we showed that the triggering field depends on the magnetisation or/and the system configuration, and that is not represented by a unique fixed field. Furthermore, we realised that the fields where the magnetic jumps stop are similar to those of the 700mK curve. We suggested that the reason for this is that the temperature during these jumps increased to a value similar to 700mK, therefore annealing the sample (which we later corroborated).

We found also a field sweep rate dependence for the jumps. The jumps

can only be seen for the higher sweep rates. When the sweep rate is lowered the magnetisation starts with a slow increase, just as for the jumps, but then smoothly joins the Kagome plateau. The very flat start of the magnetisation at the lowest temperatures was ascribed to the possible existence of an energy gap given by the ice rule energy.

The out-of-equilibrium dynamics as a function of field for temperatures below the freezing temperature were shown to be very similar for magnetic fields applied along [111] and [100]. However we could discern two differences. The first is that the threshold field is much lower for the [100] case. The second is related to the evolution of the magnetisation after the jump. While in the [111] case there is a quasi-plateau after the jumps, in [100] there is a steady linear march to saturation. These differences stem from the differences between the strings formed as the magnetisation increases, which have very different geometrical constraints for the system oriented along [111] and [100] with respect to the applied field.

Up to chapter 7 all experiments were performed with the brass magnetometer described in section 3.2.1. From chapter 8 onwards, all experiments were performed with the specially designed plastic magnetometer described in section 3.2.2. This new design allowed us to obtain the temperature of the sample by the direct measurement of it with a thermometer very well coupled to the sample. The plastic magnetometer also improved our signal quality by an order of magnitude for a magnetic gradient one order of magnitude lower than in the original publication (a total improvement of a factor of 100 in sensitivity over that of the published design).

The use of the plastic magnetometer allowed us to improve our understanding of the magnetic jumps and to put forward the idea of magnetic deflagration in chapter 8. In this context, pairs of magnetic monopoles have to overcome a gap in order to separate, and when they achieve this they span the whole sample, flipping an $O(L)$ spins in their way. At low temperatures, we argued for the possibility of a phonon bottleneck, *i.e.* the spin system being badly coupled to the phonon system which makes thermalisation very difficult. In this case, monopoles travelling towards the sample surface flip spins, lowering their energy. Thus, the excess energy is dumped to the phonon system, heating up the local environment of the spin that is being flipped. We detected these temperature increments by means of our experimental set-up. We found that at the jumps, the sample temperature increases up to about the freezing temperature, *i.e.*, up to the point at which the system can reach equilibrium by thermalising. This fact correlated with the magnetisation jumping up to an equivalent equilibrium magnetisation at that temperature.

We were able to model the heat transfer in our experimental system which allowed us to demonstrate the relationship between the sample temperature increase and the power generated by the magnetisation processes. This model made use of the strong out-of-equilibrium behaviour and proves the energy conservation fits the data better than free energy conservation, *i.e.*, at low temperatures (below the freezing temperature) the entropic terms can be neglected.

In the last section of the chapter dedicated to deflagration, we investigated the dynamics of $Dy_2Ti_2O_7$ for low magnetic fields along [111]. We found that the limiting sweep rate dependence for jumps could change. By waiting at a fixed field and letting the system relax, we obtained jumps for even slower sweep rates than without waiting. This counter-intuitive phenomenon might be explained by the blocking of the apical spins preventing strings from continuing to advance locally. We have also measured the relaxation of the magnetisation during a fixed waiting time for different applied magnetic fields, and found that the results can be collapsed using a linear formula. This implies that the relaxation scales linearly with the field, a fact reminiscent of the linear dependence on field of the jump-free curve at slow sweep rate.

In the last chapter (9) we dealt with the transition from the Kagome state to saturation as the magnetic field is increased. We were able to reproduce the magnetisation characteristic observed in the experiment of Sakakibara *et al.* of a very steep jump in magnetisation followed by a rounded march to saturation. We also measured hysteresis below 400mK in accordance with their work, but found that the hysteresis is strongly dependent on the preparation of the system, an indication of out-of-equilibrium dynamics near the transition. We concluded that the freezing temperature at fields near the transition is $\sim$ 400mK, in contrast with the freezing temperature at the transition from zero field to the Kagome state, that was $\sim$ 700mK. This is an indication of the fact that the configuration of the system plays a fundamental role in the freezing temperature, given that at zero field the energy landscape is much more complex than in the Kagome state (where all apical spins are ordered).

As a consequence of the experimental results and the discussion, it is not clear whether the transition to saturation is of the first order type predicted by theory, or rather an out-of-equilibrium transition without thermodynamic meaning.

Finally, in section 9.3 we have discussed the field-angle rotation experiment by Sato *et al.*. We simulated this experiment by means of Monte Carlo simulations of both the nearest neighbour model and that with long range dipolar interactions. We found that even though the general trends of the experiment are followed by the simulations, they cannot satisfactorily ex-

plain the mysterious double peak feature appearing when the field is tilted less than 10° from the [111] direction to the [112] direction. We tried to alter the common model (equation 2.2) to include second and third neighbour interactions in many different forms, but none of our efforts accounted for the experimental signature. We therefore propose using this experiment in further investigations seeking the precise model describing the low temperature dynamics of $Dy_2Ti_2O_7$, by matching simulations of the proposed corrections to the model with the experimental data.

Future work

During this thesis we have investigated a set of problems concerning the experimental behaviour of $Dy_2Ti_2O_7$ at low temperatures. There remain several questions that we could not completely answer, for which further experimental and numerical data are highly desirable.

- In chapter 5 we showed that the bifurcation point for ZFC-FC curves obeys the same trend for a single crystal with applied field along the [100] and the one previously observed for polycrystals. Preliminary results on simulations of both the dipolar and the nearest neighbour model indicate that this behaviour is purely caused by the system with the magnetic field pointing along the [100] and is absent for systems with the magnetic field pointing along [111] and [110].

- In chapter 6 we discussed the Kasteleyn transition for strings, and found that it was compatible with a finite amount of monopolar excitations. Although convex characteristics of the magnetisation were clearly seen for up sweeps, they did not show up clearly in the down sweeps for temperatures near the freezing temperature. Further experimentation is needed to understand this behaviour.

- In chapter 8 magnetisation jumps were characterised. The deflagration in $Dy_2Ti_2O_7$ should be investigated further. To this end, we recommend following the path used in the study of molecular magnets, where the deflagration front was completely characterised using local probes for magnetisation such as Hall sensor arrays (see for instance [76]).

- In chapter 9 we showed that experimental data on the transition from the Kagome state to saturation at low temperature was compatible with freezing. This fact has to be made compatible with the prediction of a first order transition in the same region of parameter space. We have preliminary numerical data on the formation of a crystal of

monopoles for simulations that maintain a fixed number of monopoles. In the future this method should be applied to the region of parameters in which the Kagome to saturation transition occurs, to obtain further microscopic information on the behaviour of the system at the transition.

Appendix A

Paramagnetic and mean field susceptibilities: Curie-Weiss law

The statistical magnetic response of a set of N isolated Ising spins of magnetic moment μ without mutual interactions can be calculated exactly [86]. Before the description we outline the obvious results. If the magnetic field is strong enough to overcome thermal fluctuations, the spins align. Thermal fluctuations tend to randomise the direction of spins and then minimise the magnetisation in the direction of the field. For the intermediate regime, because of the absence of an energy scale associated with the interaction, the behaviour can only depend on a dimensionless combination of the parameters H and T. Furthermore, the only such adimensionless combination is formed by the variable $\mu H/k_B T$.

Paramagnet

For Ising spins, the energy of the system can be defined as $+\mu H$ for a spin opposing the magnetic field and $-\mu H$ for a spin aligned with the magnetic field. With this one can quickly obtain the partition of the system function in the canonical ensemble as

$$\mathcal{Z} = \left(e^{\beta\epsilon} + e^{-\beta\epsilon}\right)^N = \left(2\cosh\left(\beta\epsilon\right)\right)^N \tag{A.1}$$

with $\epsilon = \mu H$ and $\beta = 1/k_B T$. Accordingly, the Helmholtz free energy is given by

$$F = -N\beta \ln\left(2\cosh\left(\beta\epsilon\right)\right) \tag{A.2}$$

and the magnetisation by

$$M = -\left(\frac{\partial F}{\partial H}\right)_T = N\mu \tanh(\beta\epsilon) \tag{A.3}$$

Mean field ferromagnet and antiferromagnet

In the case of Ising spins an energy scale can be introduced by a nearest neighbor interaction $\pm J$ with the positive sign for an antiferromagnet and the negative for a ferromagnet.

The Hamiltonian reads

$$\mathcal{H} = \pm J \sum_{<i,j>} \mathbf{S_i} \cdot \mathbf{S_j} + \sum_i \mathbf{H} \cdot \mathbf{S_i} \tag{A.4}$$

where $< i, j >$ accounts for pairs of nearest neighbours. In mean field this Hamiltonian is expanded to first order in the fluctuations from the mean magnetisation [87] $\delta\mathbf{S_i} = \mathbf{S_i} - \mathbf{M}$, where the magnetisation $\mathbf{M}$ can be made appear using that $\mathbf{S_i} =(\mathbf{S_i} - \mathbf{M} + \mathbf{M})$, which replaced in equation A.4 changes the first term as follows,

$$\mathbf{S_i} \cdot \mathbf{S_j} = \mathbf{M^2} + \mathbf{M} \cdot (\mathbf{S_i} - \mathbf{M}) + \mathbf{M} \cdot (\mathbf{S_j} - \mathbf{M}) + O((\delta\mathbf{S_i})^2) \tag{A.5}$$

In this way the mean field Hamiltonian for N particles reads

$$\mathcal{H}_{mf} = -\frac{\pm 1}{2} JN\mathbf{M^2} + \sum_i (\mathbf{H} + \pm J\mathbf{M}) \cdot \mathbf{S_i} \tag{A.6}$$

where the interaction of the surrounding spins averages to a 'magnetic field'. In equation A.6 the interaction has been incorporated in the total magnetisation, and the spins can be considered as paramagnetic. In this way, the solution for a paramagnet can be recalled and used. The magnetisation along the magnetic field direction is then given by

$$M = N\mu \tanh(\beta(\epsilon \pm JM)) \tag{A.7}$$

which is a self-consistent equation for M.

We can summarise the results for the three cases, paramagnet ($J = 0$), ferromagnet ($J < 0$) and antiferromagnet ($J > 0$) for the important case of high temperature and low magnetic field. This is called Curie-Weiss law and states

$$\chi = \frac{dM}{dH} \sim \frac{1}{T - \Theta_{CW}} \tag{A.8}$$

with $\Theta_{CW} = J/k_B$ the characteristic energy (in units of temperature) called Curie-Weiss temperature.

Appendix B

Effect of platform twisting on the magnetometer signal

The measured capacitance at high capacitances has shown that the magnetometer is susceptible to bending due to torque on the sample. The simplest model for the effect on the measured capacitance is that of one plate tilted with respect to the other. This tilt can thought as occuring around the centre of the plate where it seems more likely to happen because of the two pairs of crossed wires constraining the movement.

We can see that for the case of a square plate we have to integrate the following formula between 0 and L, the length of plate:

$$dC = \frac{\epsilon_0 \bar{A}}{(x_0 - \frac{L}{2}\sin\theta) + y\tan\theta} dy \tag{B.1}$$

where $\bar{A}$ is the linear dimension in z. The result of the integration is

$$C = \frac{\epsilon_0 \bar{A}}{\tan\theta}[\ln|L\tan\theta + x_0 - \frac{L}{2}\sin\theta| - \ln|x_0 - \frac{L}{2}\sin\theta|] \tag{B.2}$$

The capacitance as a function of angle is plotted in the figure below for typical experimental values of $L = 13$mm, $x_0 = 0.1$mm

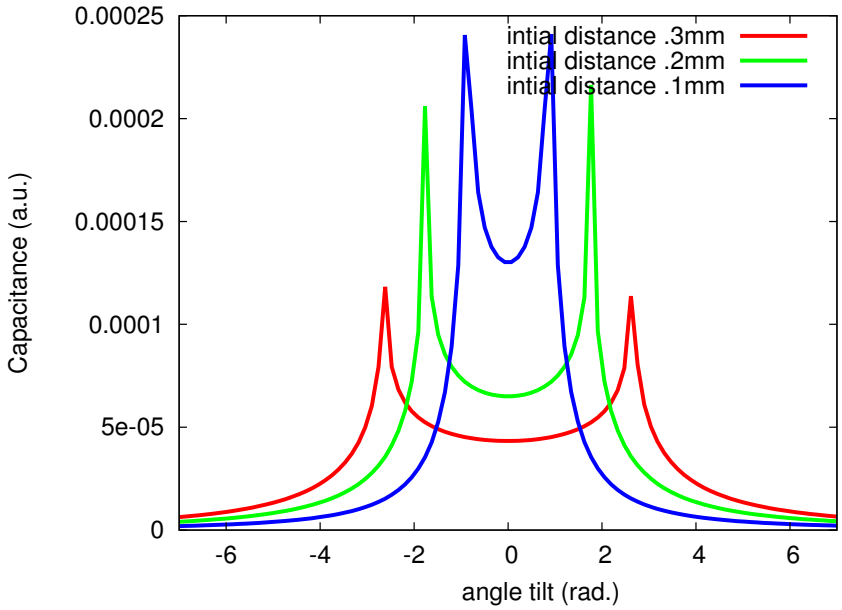
0.00025
0.0002
0.00015
0.0001
5e-05
0
Capacitance (a.u.)
-6
-4
-2
0
2
4
6
angle tilt (rad.)
intial distance .3mm
intial distance .2mm
intial distance .1mm

Bibliography

[1] A. P. Ramirez. Strongly geometrically frustrated magnets. *Annual Review of Materials Science*, **24**(1) 453 (1994).

[2] R. Moessner and J. T. Chalker. Low-temperature properties of classical geometrically frustrated antiferromagnets. *Physical Review B*, **58**(18) 12049 (1998).

[3] J. D. Bernal and R. H. Fowler. A theory of water and ionic solution, with particular reference to Hydrogen and Hydroxyl ions. *The Journal of Chemical Physics*, **8**(1) 515 (1933).

[4] R. Moessner. Relief and generation of frustration in pyrochlore magnets by single-ion anisotropy. *Physical Review B*, **57**(10) R5587 (1998).

[5] P. W. Anderson. Ordering and antiferromagnetism in ferrites. Phys. Rev., **102**(4) 1008 (1956).

[6] L. Pauling. The structure and entropy of ice and of other crystals with some randomness of atomic arrangement. *Journal of the American Chemical Society*, **57**(12) 2680 (1935).

[7] E.H. Lieb. Residual entropy of square ice. Phys. Rev., **162**(1) 162 (1967).

[8] W. F. Giauque and M. F. Ashley. Molecular rotation in ice at 10K. Free energy of formation and entropy of water. *Physical Reviews*, **43**(1) 81 (1933).

[9] A. P. Ramirez, A. Hayashi, R. J. Cava, R. Siddharthan and B. S. Shastry. Zero-point entropy in 'spin ice'. *Nature*, **399** (6734) 333 (1999).

[10] J. S. Gardner, M. J. P. Gingras and J. E. Greedan. Magnetic pyrochlore oxides. *Reviews of Modern Phyisics*, **82**(1) 53 (2010).

[11] R. G. Melko and M. J. P. Gingras. Monte Carlo studies of the dipolar spin ice model. *Journal of Physics: Condensed Matter*, **16**(43) R1277 (2004).

[12] H. W. J. Blöte, R. F. Wielinga and W. J. Huiskamp. Heat-capacity measurements on rare-earth double oxides $R_2M_2O_7$. *Physica*, **43**(4) 549 (1969).

[13] S. T. Bramwell, M. J. Harris, B. C. den Hertog, M. J. P. Gingras, J. S. Gardner, D. F. McMorrow, A. R. Wildes, A. L. Cornelius, J. D. M. Champion, R. G. Melko and T. Fennell. Spin correlations in $Ho_2Ti_2O_7$: a dipolar spin ice system. *Physical Review Letters*, **87**(4) 047205 (2001).

[14] T. Fennell, O.A. Petrenko, G. Balakrishnan, S.T. Bramwell, J.D.M. Champion, B. Fåk, M.J. Harris and D.McK. Paul. Field-induced partial order in the spin ice dysprosium titanate. *Applied Physics A: Materials Science & Processing*, **74** S889 (2002).

[15] T. Fennell, O. A. Petrenko, B. Fåk, S. T. Bramwell, M. Enjalran, T. Yavors'kii, M. J. P. Gingras, R. G. Melko and G. Balakrishnan. Neutron scattering investigation of the spin ice state in $Dy_2Ti_2O_7$. *Physical Review B*, **70**(13) 134408 (2004).

[16] D. J. P. Morris, D. A. Tennant, S. A. Grigera, B. Klemke, C. Castelnovo, R. Moessner, C. Czternasty, M. Meissner, K. C. Rule, J.-U. Hoffmann, K. Kiefer, S. Gerischer, D. Slobinsky and R. S. Perry. Dirac strings and magnetic monopoles in the spin ice $Dy_2Ti_2O_7$. *Science*, **326**(5951) 411 (2009).

[17] B. Klemke, M. Meissner, P. Strehlow, K. Kiefer, S. Grigera and D. Tennant. Thermal relaxation and heat transport in the spin ice material $Dy_2Ti_2O_7$. *Journal of Low Temperature Physics*, 1 (2011).

[18] S. T. Bramwell, M. N. Field, M. J. Harris and I. P. Parkin. Bulk magnetization of the heavy rare earth titanate pyrochlores - a series of model frustrated magnets. *Journal of Physics: Condensed Matter*, **12**(4) 483 (2000).

[19] K. Kitagawa, R. Higashinaka, K. Ishida, Y. Maeno and M. Takigawa. High-temperature spin relaxation process in $Dy_2Ti_2O_7$ probed by Ti^{47}-NQR. *Physical Review B*, **77**(21) 214403 (2008).

[20] R. Moessner and S. L. Sondhi. Theory of the [111] magnetization plateau in spin ice. *Physical Review B*, **68**(6) 064411 (2003).

[21] S. T. Bramwell and M. J. P. Gingras. Spin ice state in frustrated magnetic pyrochlore materials. *Science*, **294**(5546) 1495 (2001).

[22] T. Yavors'kii, T. Fennell, M. J. P. Gingras and S. T. Bramwell. Spin ice: a test case for emergent clusters in a frustrated magnet $Dy_2Ti_2O_7$. *Physical Review Letters*, **101**(3) 037204 (2008).

[23] R. G. Melko, B. C. den Hertog and M. J. P. Gingras. Long-range order at low temperatures in dipolar spin ice. *Physical Review Letters*, **87**(6) 067203 (2001).

[24] L. D. C. Jaubert, J. T. Chalker, P. C. W. Holdsworth and R. Moessner. Three-dimensional Kasteleyn transition: spin ice in a [100] field. *Physical Review Letters*, **100**(6) 067207 (2008).

[25] C. Castelnovo, R. Moessner and S. L. Sondhi. Thermal quenches in spin ice. *Physical Review Letters*, **104**(10) 107201 (2010).

[26] P. W. Kasteleyn. Dimer statistics and phase transitions. *Journal of Mathematical Physics*, **4**(2) 287 (1963).

[27] J. F. Nagle. Theory of biomembrane phase transitions. *The Journal of Chemical Physics*, **58**(1) 252 (1973).

[28] J. F. Nagle. Lipid bilayer phase transition: density measurements and theory. *Proceedings of the National Academy of Sciences of the United States of America*, **70**(12) 3443 (1973).

[29] T. Sakakibara, T. Tayama, Z. Hiroi, K. Matsuhira and S. Takagi. Observation of a liquid-gas-type transition in the pyrochlore spin ice compound $Dy_2Ti_2O_7$ in a magnetic field. *Physical Review Letters*, **90**(20) 207205 (2003).

[30] K. Matsuhira, Z. Hiroi, T. Tayama, S. Takagi and T. Sakakibara. A new macroscopically degenerate ground state in the spin ice compound $Dy_2Ti_2O_7$ under a magnetic field. *Journal of Physics: Condensed Matter*, **14**(29) L559 (2002).

[31] Z. Hiroi, K. Matsuhira, S. Takagi, T. Tayama and T. Sakakibara. Specific heat of Kagomé ice in the pyrochlore oxide $Dy_2Ti_2O_7$. *Journal of the Physical Society of Japan*, **72**(2) 411 (2003).

[32] M. Udagawa, M. Ogata and Z. Hiroi. Exact result of ground-state entropy for Ising pyrochlore magnets under a magnetic field along [111] axis. *Journal of the Physical Society of Japan*, **71**(10) 2365 (2002).

[33] Y. Tabata, H. Kadowaki, K. Matsuhira, Z. Hiroi, N. Aso, E. Ressouche and B. Fåk. Kagomé ice state in the dipolar spin ice $Dy_2Ti_2O_7$. *Physical Review Letters*, **97**(25) 257205 (2006).

[34] R. Moessner and S. L. Sondhi. Theory of the [111] magnetization plateau in spin ice. *Physical Review B*, **68**(6) 064411 (2003).

[35] C. Castelnovo, R. Moessner and S. L. Sondhi. Magnetic monopoles in spin ice. *Science*, **451**(7174) 42 (2008).

[36] S. V. Isakov, K. S. Raman, R. Moessner and S. L. Sondhi. Magnetization curve of spin ice in a [111] magnetic field. *Physical Review B*, **70**(10) 104418 (2004).

[37] T. Fennell, S. T. Bramwell, D. F. McMorrow, P. Manuel and A. R. Wildes. Pinch points and Kasteleyn transitions in Kagome ice., *Nature Physics*, **3**(8) 566 (2007).

[38] H. Aoki, T. Sakakibara, K. Matsuhira and Z. Hiroi. Magnetocaloric effect study on the pyrochlore spin ice compound $Dy_2Ti_2O_7$ in a [111] magnetic field. *Journal of the Physical Society of Japan*, **73**(10) 2851 (2004).

[39] H. Sato, K. Matsuhira, T. Sakakibara, T. Tayama, Z. Hiroi and S. Takagi. Field-angle dependence of the ice-rule breaking spin-flip transition in $Dy_2Ti_2O_7$. *Journal of Physics: Condensed Matter*, **19**(14) 145272 (2007).

[40] R. Higashinaka and Y. Maeno. Field-induced transition on a triangular plane in the spin-ice compound $Dy_2Ti_2O_7$. *Physical Review Letters*, **95**(23) 237208 (2005).

[41] R. Higashinaka, H. Fukazawa, K. Deguchi and Y. Maeno. Low temperature specific heat of $Dy_2Ti_2O_7$ in the Kagome ice state. *Journal of the Physical Society of Japan*, **73**(10) 2845 (2004).

[42] S. T. Bramwell, S. R. Giblin, S. Calder, R. Aldus, D. Prabhakaran and T. Fennell. Measurement of the charge and current of magnetic monopoles in spin ice. *Nature*, **461**(7266) 956 (2009).

[43] T. Fennell, P. P. Deen, A. R. Wildes, K. Schmalzl, D. Prabhakaran, A. T. Boothroyd, R. J. Aldus, D. F. McMorrow and S. T. Bramwell. Magnetic Coulomb phase in the spin ice $Ho_2Ti_2O_7$. *Science*, **326**(5951) 415 (2009).

[44] H. Kadowaki, N. Doi, Y. Aoki, Y. Tabata, T. J. Sato, J. W. Lynn, K. Matsuhira and Z. Hiroi. Observation of magnetic monopoles in spin ice. *Journal of the Physical Society of Japan*, **78**(10) 103706 (2009).

[45] J. Snyder, B. G. Ueland, J. S. Slusky, H. Karunadasa, R. J. Cava and P. Schiffer. Low-temperature spin freezing in the $Dy_2Ti_2O_7$ spin ice. *Physical Review B*, **69**(6) 064414 (2004).

[46] J. Snyder, B. G. Ueland, J. S. Slusky, H. Karunadasa, R. J. Cava, Ari Mizel and P. Schiffer. Quantum-classical reentrant relaxation crossover in $Dy_2Ti_2O_7$ spin ice. *Physical Review Letters*, **91**(10) 107201 (2003).

[47] J. Snyder, J. S. Slusky, R. J. Cava and P. Schiffer. How 'spin ice' freezes. *Nature*, **413**(6851) 48 (2001).

[48] K Matsuhira, Y Hinatsu and T Sakakibara. Novel dynamical magnetic properties in the spin ice compound $Dy_2Ti_2O_7$. *Journal of Physics: Condensed Matter*, **13**(31) L737 (2001).

[49] L. D. C. Jaubert and P. C. W. Holdsworth. Signature of magnetic monopole and Dirac string dynamics in spin ice *Nature Physics*, **5**(4) 258 (2009).

[50] L. D. C. Jaubert and P. C. W. Holdsworth. Magnetic monopole dynamics in spin ice. *Journal of Physics: Condensed Matter* **23**(16) 164222 (2011).

[51] G. Balakrishnan, O. A. Petrenko, M. R. Lees and D. McK Paul. Single crystal growth of rare earth titanate pyrochlores. *Journal of Physics: Condensed Matter*, **10**(44) L723 (1998).

[52] G.M. Kalvius and R.S. Tebble. Experimental magnetism. *J. Wiley*, Experimental Magnetism Series Vol. 1 (1979).

[53] A. Finkler, Y. Segev, Y. Myasoedov, M. L. Rappaport, L. Neâeman, D. Vasyukov, E. Zeldov, M. E. Huber, J. Martin and A. Yacoby. Self-aligned nanoscale SQUID on a tip. *Nano Letters*, **10**(3) 1046 (2010).

[54] S. Foner. versatile and sensitive vibrating-sample magnetometer. *Review of Scientific Instruments*, **30**(7) 548 (1959).

[55] S. Legl, C. Pfleiderer and K. Krämer. Vibrating coil magnetometer for milli-Kelvin temperatures. *Review of Scientific Instruments*, **81**(4) 043911 (2010).

[56] J. G. E. Harris, D. D. Awschalom, F. Matsukura, H. Ohno, K. D. Maranowski and A. C. Gossard. Integrated micromechanical cantilever magnetometry of $Ga_{1-x}Mn_xAs$. *Applied Physics Letters*, **75**(8) 1140 (1999).

[57] A. G. Swanson, Y. P. Ma, J. S. Brooks, R. M. Markiewicz and N. Miura. Diaphragm magnetometer for dc measurements in high magnetic fields. *Review of Scientific Instruments*, **61**(2) 848 (1990).

[58] T. Sakakibara, H. Mitamura, T. Tayama and H. Amitsuka. Faraday force magnetometer for high-sensitivity magnetization measurements at very low temperatures and high fields. *Japanese Journal of Applied Physics*, **33**(Part 1, No. 9A) 5067 (1994).

[59] T. Sakon and M. Motokawa. Electromechanical magnetization measurements at ultralow temperatures and high magnetic fields. *Review of Scientific Instruments*, **71**(9) 3474 (2000).

[60] J. S. Brooks, M. J. Naughton, Y. P. Ma, P. M. Chaikin and R. V. Chamberlin. Small sample magnetometers for simultaneous magnetic and resistive measurements at low temperatures and high magnetic fields. *Review of Scientific Instruments*, **58**(1) 117 (1987).

[61] F. Pobell. Matter and methods at low temperatures. *Springer*, second edition (2002).

[62] See for example L. D. Landau and E. M. Lifshitz. Theory of elasticity (course of theoretical physics). *Pergamon Press*, second edition (1981).

[63] E. Ohmichi, Y. Yoshida, S. I. Ikeda, N. V. Mushunikov, T. Goto and T. Osada. Double metamagnetic transition in the bilayer ruthenate $Sr_3Ru_2O_7$. *Physical Review B*, **67**(2) 024432 (2003).

[64] S. A. Grigera, R. A. Borzi, A. P. Mackenzie, S. R. Julian, R. S. Perry and Y. Maeno. Angular dependence of the magnetic susceptibility in the itinerant metamagnet $Sr_3Ru_2O_7$. *Physical Review B*, **67**(21) 214427 (2003).

[65] S. A. Grigera, P. Gegenwart, R. A. Borzi, F. Weickert, A. J. Schofield, R. S. Perry, T. Tayama, T. Sakakibara, Y. Maeno, A. G. Green and A. P. Mackenzie. Disorder-sensitive phase formation linked to metamagnetic quantum criticality. *Science*, **306**(5699) 1154 (2004).

[66] M. E. J. Newman and G. T. Barkema. Monte Carlo methods in statistical physics. *Oxford University Press*, reprinted (2001).

[67] D. P. Landau and K. Binder. A guide to Monte Carlo simulations in statistical physics. *Cambridge University Press*, second edition (2005).

[68] D. C. Rapaport. The art of molecular dynamics simulation. *Cambridge University Press*, second edition (2004).

[69] M. P. Allen and D. J. Tildesley. Computer simulation of liquids. *Oxford University Press*, (1987).

[70] S. V. Isakov, K. Gregor, R. Moessner and S. L. Sondhi. Dipolar spin correlations in classical pyrochlore magnets. *Physical Review Letters*, **93**(16) 167204 (2004).

[71] L. D. C. Jaubert. Topological constraints and defects in Spin Ice. PhD Thesis, ENS Lyon (2009).

[72] D. Slobinsky, C. Castelnovo, R. A. Borzi, A. S. Gibbs, A. P. Mackenzie, R. Moessner, S. A. Grigera. Unconventional magnetization processes and thermal runaway in spin-ice $Dy_2Ti_2O_7$. *Physical Review Letters*, **105**(26) 267205 (2010).

[73] R. Moessner. Magnets with strong geometric frustration. *Can. J. Phys.*, **79**(11-12) 1283 (2001).

[74] A. Aharoni. Demagnetizing factors for rectangular ferromagnetic prisms. *Journal of Applied Physics*, **83**(6) 3432 (1998).

[75] Y. Suzuki, M. P. Sarachik, N. Avraham, Y. Myasoedov, H. Shtrikman, E. Zeldov, E. M. Rumberger, D. N. Hendrickson and G. Christou. The occurrence of avalanches in a single crystal of Mn_12-acetate. *Journal of Applied Physics* **97**(10) 10M517 (2005).

[76] Y. Suzuki, M. P. Sarachik, E. M. Chudnovsky, S. McHugh, R. Gonzalez-Rubio, N. Avraham, Y. Myasoedov, E. Zeldov, H. Shtrikman, N. E. Chakov and G. Christou. Propagation of avalanches in Mn_12-acetate: Magnetic Deflagration. *Physical Review Letters*, **95**(14) 147201 (2005).

[77] A. Hernández-Mínguez, J. M. Hernandez, F. Macià, A. García-Santiago, J. Tejada and P. V. Santos. Quantum magnetic deflagration in Mn_12-acetate. *Physical Review Letters*, **95**(21) 217205 (2005).

[78] S. McHugh, R. Jaafar, M. P. Sarachik, Y. Myasoedov, A. Finkler, H. Shtrikman, E. Zeldov, R. Bagai and G. Christou. Effect of quantum tunneling on the ignition and propagation of magnetic avalanches in Mn_{12}-acetate. *Physical Review B*, **76**(17) 172410 (2007).

[79] S. McHugh, Bo Wen, Xiang Ma, M. P. Sarachik, Y. Myasoedov, E. Zeldov, R. Bagai and G. Christou. Tuning magnetic avalanches in the molecular magnet Mn_12-acetate. *Physical Review B*, **79**(17) 174413 (2009).

[80] D. A. Garanin and E. M. Chudnovsky. Theory of magnetic deflagration in crystals of molecular magnets. *Physical Review B*, **76**(5) 054410 (2007).

[81] T. Fennell, O. A. Petrenko, B. Fåk, J. S. Gardner, S. T. Bramwell and B. Ouladdiaf. Neutron scattering studies of the spin ices $Ho_2Ti_2O_7$ and $Dy_2Ti_2O_7$ in applied magnetic field. *Physical Review B*, **72**(22) 224411 (2005).

[82] J. H. Van Vleck. Paramagnetic relaxation and the equilibrium of lattice oscillators. it Phys. Rev, **59**(9) 724 (1941).

[83] S. R. Giblin, S. T. Bramwell, P. C. W. Holdsworth, D. Prabhakaran and I. Terry. Creation and measurement of long-lived magnetic monopole currents in spin ice *Nature Physics*, **7** (3) 252 (2011).

[84] L. Onsager. Deviations from Ohm's law in weak electrolytes. *J. Chem. Phys.* **2** 599 (1934).

[85] Ryuji Higashinaka. Field orientation control of geometrical frustration in the spin ice $Dy_2Ti_2O_7$. PhD Thesis, Kyoto University (2005).

[86] R. K. Pathria. Statistical mechanics. *Butterworth Heinemann*, second edition (1996).

[87] J. Cardy. Scaling and renormalization in statistical physics. *Cambridge University Press* (1996).